



UNIVERSITÀ DEGLI STUDI DI NAPOLI FEDERICO II
DIPARTIMENTO DI SCIENZE FISICHE

TESI DI DOTTORATO IN FISICA FONDAMENTALE ED APPLICATA

**Thin solid film and interfaces analysis
with Optical Second Harmonic Generation:
application to nanotribology and to
the study of the $\text{LaAlO}_3/\text{SrTiO}_3$ interface**

ANNUNZIATA SAVOIA

Tutor:
Prof. L. Marrucci

Coordinatore:
Prof. L. Marrucci

XXI CICLO 2005-2008

Contents

Introduction	ii
1 Second Harmonic Generation	1
1.1 Local second harmonic generation	2
1.1.1 Nonlinear Surface polarization	4
1.1.2 Second Harmonic Radiation generated from a polarized sheet	11
1.1.3 Second harmonic signal generated from a non-chiral and isotropic interface	22
1.1.4 Homodyne SHG measurements	27
1.2 Nonlocal Second Harmonic Generation	31
1.2.1 Polarization in a nonlinear optical medium	31
1.2.2 Nonlocal Second Harmonic Radiation generated from centrosymmetric material	39
I Application to nanotribology	49
2 Our project and Friction Apparatus	50
2.1 The project: simultaneous measurements of second harmonic radiation and friction force	52
2.2 Design of Friction Apparatus	53
2.3 Electronic setup of the FA	56
2.3.1 Stepper motor and motion control system	57
2.3.2 Strain gauge and signal conditioning	58
3 Mica	66
3.1 General properties of muscovite mica	66
3.2 Optical properties of muscovite mica	68
3.3 Nonlocal Second Harmonic Radiation generated from muscovite mica	70
4 Experimental setup and SHG results for muscovite mica	74
4.1 Second Harmonic Experimental setup	75

4.1.1	Results and discussion	76
II	Application to the study of the $\text{LaAlO}_3/\text{SrTiO}_3$ interface	88
5	$\text{LaAlO}_3/\text{SrTiO}_3$ interface	89
5.1	Properties of the $\text{LaAlO}_3/\text{SrTiO}_3$ interface	90
5.2	State of the art	92
6	Experimental setup and SHG results for $\text{LaAlO}_3/\text{SrTiO}_3$ interface	96
6.1	Samples	98
6.2	Preliminary results	99
6.3	SHG intensity results	102
6.4	Homodyne SHG measurements: results and discussion	105
6.5	Homodyne SHG measurements and electric-field-effect	115
6.6	Homodyne SHG measurements and orientational order	120
	Conclusions	123

Contents

Introduction

This thesis is divided in two Parts, which reflect two distinct applications of Optical Second Harmonic Generation (SHG). In this Introduction a brief overview is given for both of them. SHG is a nonlinear optical process that consists in the generation of a radiation with double frequency with respect to the frequency of an incident electromagnetic field. Schematically, we can say that the incident optical beam induces a polarization \vec{P} in a medium with a component, quadratic in the electric field, described by a third order tensor $\chi^{(2)}$ called nonlinear second order susceptibility. By measuring the intensity, the polarization and the phase of the second harmonic radiation, one can determine the elements of the tensor $\chi^{(2)}$ and then obtain information about the medium. The attractive feature of this process is that, in the electric dipole approximation, it is forbidden in the bulk of a centrosymmetric medium, but allowed at the surface of the medium or at the interface between two different centrosymmetric media, where the inversion symmetry is necessarily broken. For this reason, SHG is a technique used

for studying surfaces and, most importantly, interfaces between centrosymmetric materials, the so-called “buried interfaces” [3]. Besides, with respect to the surface sensitive particle scattering techniques, which require an ultra high vacuum environment to operate and usually have a penetration depth of only a few atomic layers, SHG technique can be used in every kind of environment, provided it is optically transparent.

Let us now introduce the first application of the SHG technique performed in my thesis work, discussed in Part 1 of this dissertation. The old empirical laws of the friction do not always hold true at molecular level. In fact, theoretical and experimental works belonging to the so-called field of nanotribology have not just extended, but in some cases fundamentally altered, the picture that was developed from macroscale studies [5]. For example, it was found that the coefficient of friction varies considerably as function of the normal load, temperature and sliding speed, so no single value can adequately describe the material. In particular, the static friction coefficient of a large number of metals increases at low loads [1] does not verifying the proportionality between the friction force and the normal applied load. Moreover, when thin liquid film of lubricant are interposed between sliding surfaces, it was found the friction force depends critically on the

number of layers of lubricant and could not be accounted in terms of a continuum model where the liquid film is assumed to have newtonian viscosity [4]. The nature of the interactions between two surfaces brought close together, have been experimentally studied with the Surface Force Apparatus (SFA). It consists of a pair of mica surfaces, which are mounted in a crossed cylinder geometry. Mica is a centrosymmetric material that is most often used as a crystalline substrate for nanotribological studies because it can be easily cleaved to obtain an atomically smooth surface. The mica surfaces are treated to adsorb molecules of lubricant. A shortcoming of SFA experiments is that the molecular organization have to be inferred from measurements of the tribological properties that they influence. To this purpose, since the SHG technique can be readily adopted to provide molecular orientation of thin films deposited between two surfaces, our starting idea is to apply the SHG for nanotribological investigations in the controlled frame of the SFA. Our project and its state of the art is the subject of the first part of this thesis work. The idea consists in to perform simultaneous measurements of second harmonic radiation and friction forces in a SFA setup. In this way, by observing with the SHG the behavior of a molecular film of lubricant during the shear, we want try to correlate the molecular variations detected by SHG with

the tribological phenomena. At the present, this project is still underway and we have not reached yet the stage of performing SHG measurements on lubricant films under shear, but some important intermediate steps have been completed and will be reported here. In particular, a first step has been the mounting and interfacing of the Friction Apparatus, a modified version of the SFA, and a second one has been the measurement of the second harmonic signal generated from the mica, which represents the background signal for our planned measurements of friction. Our SHG measurements showed that second harmonic signal generated from a mica substrate is unexpected intense and generated from the bulk. Since the mica is centrosymmetric, this means that its nonlinear response is nonlocal (i.e., corresponding to the higher-order multipole contributions). In the literature there are only few and not very recent works [2] on the second harmonic radiation generated from mica, that do not consider the case of nonlocal response. Therefore, we decided to develop a theoretical model in order to calculate the second harmonic radiation including the nonlocal contribution to the nonlinear response. This model and its use for interpreting the SHG data will be presented in the Part 1 of this thesis.

The second part of the thesis work consisted into the study of a particular oxide

interface, the $\text{LaAlO}_3/\text{SrTiO}_3$ interface. Oxides interfaces attract a large of interest for basic research as well for technological applications. The interest on these materials has rapidly grown recently, since the observation of the high electrical conductivity and mobility in the heterointerfaces formed between a thin LaAlO_3 (LAO) film deposited on a TiO_2 terminated SrTiO_3 (STO) substrate [23]. Despite the growing body of evidence [25, 26, 33, 30, 31, 28, 37, 32, 36, 35], the physics underlying the observed interfacial conduction phenomena is still hotly debated. A leading interpretation is based on the so-called “polar catastrophe” idea [25]: the charged character of the LAO atomic layers grown with a well defined order would give rise to an ever increasing electrostatic energy for increasing thickness. As this energy increase cannot be sustained, an interfacial reconstruction must necessarily occur for a large enough thickness of the LAO film. This reconstruction could be partly ionic, involving lattice distortions and/or some degree of cationic mixing [25, 29, 34, 36, 35], but it has been proposed that a purely *electronic reconstruction* may instead be the dominating effect, involving a transfer of electrons from LAO to STO. To clarify these issues, it would be desirable to use a direct experimental probe of the electronic polar rearrangements taking place at the interface. We retain that such probe is the Second Harmonic Generation

technique. In fact, because SHG is usually generated efficiently at interfaces [17], it allow us to study the electronic properties of $\text{LaAlO}_3/\text{SrTiO}_3$ interface. To this purpose, we used SHG in a homodyne phase-sensitive configuration. In this case, in fact, it is possible to measure the phase and the amplitude of the generated second harmonic radiation by means of an interferometric measurement. The technique consists in analyzing the interference between the second harmonic radiation from the sample under investigation and that from a piece of quartz (reference) in a collinear geometry. A phase delay is introduced by varying the distance between the reference and the sample. This leads to a characteristic sinusoidal behavior of the SHG signal as a function of the distance, that can be fitted in order to measure the phase and the amplitude of the nonlinear second order susceptibility.

The thesis work is organized as follows. In the Chapter 1, preliminar to both Parts of the thesis, we will describe the basic theory of SHG, in the case of local and nonlocal response from a material. Next, in the first Part, we will expose our project for nanotribological investigations. In particular, in the Chapter 2, we will show the principle of working and the interfacing of the FA and, in the Chapter 3, we will introduce the main properties of the muscovite mica and, here,

we will calculate also the second harmonic radiation generated from it. Finally, in the Chapter 4, we will show and discuss our SHG measurements from muscovite mica.

The second Part of the thesis, as said above, is dedicated to the analysis of the $\text{LaAlO}_3/\text{SrTiO}_3$ interface as detected by means of SHG. In particular, in the Chapter 5, we will introduce the properties of the interface and the state of the art on this topic. In Chapter 6, we will show our SHG measurements and discuss the results obtained.

Chapter 1

Second Harmonic Generation

This chapter contains a description of the main features of the Second Harmonic Generation (SHG) phenomenon. In the first part, we present the theory of the SHG in the case of a local nonlinear response of a medium. In this part we will calculate the reflected second harmonic field generated by a single plane wave expressing it in terms of the input beam. After that, property symmetries will be considered to obtain the second harmonic signal in the case of an isotropic and non chiral interface. The theory relative to the case where also a nonlocal nonlinear response is considered will be given in the second part of the chapter. In particular, we will show in detail the derivation of the second order polarization for a weak nonlocal response. Finally, we will calculate the non local second harmonic radiation generated from a centrosymmetric material.

1.1 Local second harmonic generation

Under excitation by a strong optical electric field, the polarization of a medium displays deviations from a linear response. These deviations are the basis of nonlinear optics. Strong electric fields give rise to nonlinear source terms in the Maxwell's equations. These sources can be described by a generalized polarization:

$$P_i(\vec{r}, t) = \int \epsilon_0 \chi_{ij}^{(1)}(\vec{r} - \vec{r}', t - t') E_j(\vec{r}', t') d^3 r' dt' + \int \chi_{ijh}^{(2)}(\vec{r} - \vec{r}', \vec{r} - \vec{r}'', t - t', t - t'') E_j(\vec{r}', t') E_h(\vec{r}'', t'') d^3 r' d^3 r'' dt' dt'' \quad (1.1)$$

where the summation over repeated indices is implied.

We stopped the expansion (1.1) to the second order because we are interested to the SHG phenomenon which emerges from the latter. The first term of the (1.1) is the linear polarization and the second one is the second order nonlinear polarization. The tensors $\chi_{ij}^{(1)}(\vec{r} - \vec{r}', t - t')$ and $\chi_{ijh}^{(2)}(\vec{r} - \vec{r}', \vec{r} - \vec{r}'', t - t', t - t'')$ are called *first order electric susceptibility* and *second order electric susceptibility*, respectively. They characterize the optical properties of the medium. Physically $\chi^{(1)}$ and $\chi^{(2)}$ are related to the microscopic structure of the medium and can be properly evaluated only with a quantum-mechanical calculation.

Often, the polarization $\vec{P}(\vec{r}, t)$ is determined by the electric field $\vec{E}(\vec{r}, t')$ at the same point in the space \vec{r} . In this case, the nonlinear response of the material is said local and the polarization becomes:

$$P_i(t) = \int \epsilon_0 \chi_{ij}^{(1)}(t-t') E_j(t') dt' + \int \epsilon_0 \chi_{ijh}^{(2)}(t-t', t-t'') E_j(t') E_h(t'') dt' dt'' \quad (1.2)$$

Expressing the fields and the polarization in the Fourier transform, the (1.2) takes the form:

$$P_i(\omega) = P_i^{(1)}(\omega) + P_i^{(2)}(\omega) \quad (1.3)$$

where

$$P_i^{(1)}(\omega) = \epsilon_0 \chi_{ij}^{(1)}(\omega) E_j(\omega) \quad (1.4)$$

and

$$P_i^{(2)}(\omega) = \epsilon_0 \chi_{ijh}^{(2)}(\omega = \omega_1 + \omega_2) E_j(\omega_1) E_h(\omega_2). \quad (1.5)$$

We defined the Fourier transform of the first and second order susceptibilities as follows:

$$\chi_{ij}^{(1)}(\omega) = \int d\tau \chi_{ij}^{(1)}(\tau) e^{i\omega\tau} \quad (1.6)$$

and

$$\chi_{ijh}^{(2)}(\omega = \omega_1 + \omega_2) = \int d\tau d\tau' \chi_{ijh}^{(2)}(\tau, \tau') e^{i\omega_1\tau + i\omega_2\tau'}. \quad (1.7)$$

Now we consider only the local second order polarization for the case $\omega_1 = \omega_2$:

$$P_i(2\omega) = \epsilon_0 \chi_{ijh}^{(2)} E_j(\omega) E_h(\omega), \quad (1.8)$$

where $\chi_{ijh}^{(2)}$ is the local second order susceptibility.

From the (1.8) one can see that the indexes j and h are dummy, so we can define

$\chi_{ijh}^{(2)}$ in such way to fulfill the following permutation symmetry:

$$\chi_{ijh}^{(2)} = \chi_{ihj}^{(2)} \quad \textit{intrinsic permutation symmetry}. \quad (1.9)$$

The local second order susceptibility is exactly zero for systems that are centrosymmetric. Nevertheless, at interface between two centrosymmetric media, the inversion symmetry is necessarily broken and, then, a second harmonic radiation can be generated. The consequence of this property is that the SHG is highly sensitive to the properties of an interface between two centrosymmetric media.

1.1.1 Nonlinear Surface polarization

To describe the SHG at the interface between two centrosymmetric media, it is useful to divide the system in three regions: an interfacial zone and two bulk media which are semi-infinite (see Fig.1.1). One suitable definition of the interface is the zone where either the material properties, such as the electronic structure

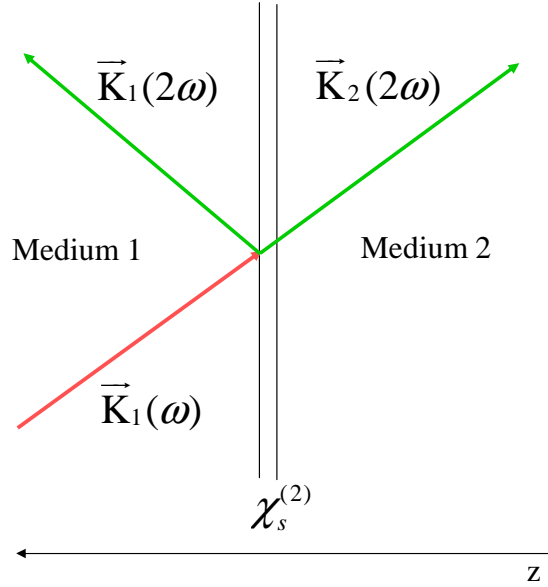


Figure 1.1: Schematic representation of the phenomenological model for the second harmonic generation at the interface between two centrosymmetric media. The pump wave at frequency ω comes from the medium 1, the radiated second harmonic radiation is emitted in both the media 1 and 2. The figure shows the xz plane, the equation $z = 0$ defines the interface.

and the molecular orientation, or the electromagnetic fields differ appreciably from those found in the bulk media. For most systems, this transitional behavior will occur within a distance of few Ångstroms. Thus, we can attribute the nonlinearity of the interface to a sheet, thick few Ångstroms, where a nonlinear polarization is located. We call this polarization as surface nonlinear polarization \vec{P}_{s1} .

¹We omit the index 2 in order to simplify the notation.

Our purpose, in this section, is to determine the expression of \vec{P}^s to calculate the discontinuity relations across the interface, schematically represented in Fig.1.1. In order to do it, let us introduce a coordinate system x, y, z (*laboratory frame*) where the x and y axes are in the plane of the interface. To model the electromagnetic properties of the interface, we express the polarization emphasizing the surface part:

$$\vec{P}(\vec{r}, 2\omega) = \vec{P}^s(x, y, 2\omega)\delta(z), \quad (1.10)$$

where $\vec{P}^s(x, y)$ is the induced electrical dipole momentum for surface unit and is given by the following relation:

$$P_i^s(x, y, 2\omega) = \varepsilon_0 \chi_{ijh}^s(2\omega) E_j(\vec{r}, \omega) E_h(\vec{r}, \omega). \quad (1.11)$$

The (1.11) defines intrinsically a surface second order susceptibility χ_{ijh}^s , which is connected to the second order (bulk) susceptibility from the following relation:

$$\chi^b(\vec{r}, 2\omega) = \chi^s(x, y, 2\omega)\delta(z). \quad (1.12)$$

The optical field that appears in the (1.11) is the field that will be in $z = 0$ if the surface layer is the vacuum². With this choice, χ^s contains information about the microscopic properties associated to the second order nonlinear response of the

²We have chose the vacuum because the refraction index of a few atomic thick layer is undefined.

medium.

If the field at the interface is a monochromatic wave:

$$\vec{E}_0 = \vec{E}_a e^{i(\vec{k}_0(\omega) \cdot \vec{r} - \omega t)} + c.c. \quad (1.13)$$

with $\vec{k}_0 = (k_{0x}, 0, k_{0z})$, the surface polarization becomes:

$$\begin{aligned} P_i^s(x, y, 2\omega) &= \varepsilon_0 \chi_{ijh}^s E_{0j}(x, y, z=0; \omega) E_{0h}(x, y, z=0; \omega) = \\ &= \varepsilon_0 \chi_{ijh}^s E_{aj} E_{ah} e^{i(k_{0x}x - \omega t)} e^{i(k_{0x}x - \omega t)} = \\ &= \varepsilon_0 \chi_{ijh}^s E_{aj} E_{ah} e^{i(2k_{0x}x - 2\omega t)} = \\ &= P_{0i}^s e^{i(k_x x - 2\omega t)} \end{aligned} \quad (1.14)$$

where we put $k_x = 2k_{0x}$, and $P_{0i}^s = \varepsilon_0 \chi_{ijh}^{(2)} E_{aj} E_{ah}$.

Therefore, the second order nonlinear polarization can be written as:

$$\vec{P}(\vec{r}, 2\omega) = \vec{P}_0^s e^{i(k_x x - 2\omega t)} \delta(z). \quad (1.15)$$

The (1.15) is the source of the second harmonic radiation. Such radiation is determined by solving Maxwell's equations, that, in the case of absence of external

charge and current, are:

$$\vec{\nabla} \cdot \vec{D} = 0 \quad (1.16)$$

$$\vec{\nabla} \cdot \vec{B} = 0 \quad (1.17)$$

$$\vec{\nabla} \times \vec{E} = -\frac{\partial \vec{B}}{\partial t} \quad (1.18)$$

$$\vec{\nabla} \times \vec{H} = \frac{\partial \vec{D}}{\partial t}. \quad (1.19)$$

They consist of 8 scalar equations that relate a total of 12 variables, 3 for each of the 4 vectors, \vec{E} , \vec{D} , \vec{H} and \vec{B} . They cannot be solved uniquely unless the relationship between \vec{B} and \vec{H} and that between \vec{E} and \vec{D} are known. These relationships are given by:

$$\vec{D} = \epsilon_0 \vec{E} + \vec{P} \quad (1.20)$$

$$\vec{B} = \mu_0 (\vec{H} + \vec{M}),$$

where \vec{P} and \vec{M} are the polarization and the magnetization of the material, respectively. It is almost always possible to neglect the magnetization. In fact, the force, due to the electromagnetic field, acting on the electron in its motion around the nucleus is:

$$\vec{F} = q(\vec{E} + \vec{v}_e \times \vec{B})$$

where \vec{v}_e is the electron speed. Since $|\vec{B}| = |\vec{E}|/c$, the magnitude absolute of the force is given by:

$$|\vec{F}| = q|\vec{E}|\sqrt{\left(1 + \frac{|\vec{v}_e|^2}{c^2}\right)}.$$

Because the ratio between the electron speed and the light velocity is of order of 10^{-5} , it is possible to neglect this ratio with respect to 1. For this reason, the total force is given only by the electric contribution $q\vec{E}$. Then, the approximation $\vec{B} = \mu_0\vec{H}$ almost always holds true.

Assuming that the generated fields have the same dependence from the x and y spatial variables and from t temporal variable as the polarization that generates them, the Maxwell's equations become:

$$\begin{aligned} \partial_z D_z &= -ik_x D_x \\ \partial_z B_z &= -ik_x B_x \\ -\partial_z E_y &= i\Omega B_x \\ \partial_z E_x &= i\Omega B_y + ik_x E_z \\ -\partial_z B_y &= -i\Omega\mu_0 D_x \\ \partial_z B_x &= -i\Omega\mu_0 D_y + ik_x B_z. \end{aligned} \tag{1.21}$$

The others components of the fields are obtained by means of the (1.20):

$$E_z = \frac{D_z - P_z}{\varepsilon_0}$$

$$D_x = \varepsilon_0 E_x + P_x \quad (1.22)$$

$$D_y = \varepsilon_0 E_y + P_y.$$

The (1.22) are singular in the plane $z = 0$ because the components x , y and z of the surface polarization are there singular.

With the aid of the equations (1.21) and (1.22), we can derive the matching conditions of the fields across the polarized sheet. To this purpose, we introduce the notation:

$$E_{i1} \equiv E_i(z) \quad \text{per} \quad z = 0^+$$

$$E_{i2} \equiv E_i(z) \quad \text{per} \quad z = 0^-$$

to indicate the components of the electric field³ in the upper and lower half-space with respect to $z = 0$ for values of z which go to zero. Then, integrating with respect to z parameter the (1.21) in the range $(-d, d)$ and calculating the integral in the limit $d \rightarrow 0$, we obtain the relations of discontinuity for the electric and

³Obviously we use the same notation also for D_x and D_y .

magnetic fields across the interface:

$$E_{x1} = E_{x2} - \frac{ik_x}{\varepsilon_0} P_z^s$$

$$E_{y2} = E_{y2} \tag{1.23}$$

$$n_1^2 E_{z2} = n_2^2 E_{z2} - \frac{ik_x}{\varepsilon_0} P_x^s$$

$$H_{x1} = H_{x2} - i\Omega P_y^s$$

$$H_{y1} = H_{y2} + i\Omega P_x^s \tag{1.24}$$

$$H_{z1} = H_{z2}.$$

1.1.2 Second Harmonic Radiation generated from a polarized sheet

Thanks to the discontinuity relations, obtained in the previous section, we calculate the second harmonic radiation, generated by the interface, propagating in the medium 1. To do it, we consider a configuration in which a laser beam at frequency ω is incident at an angle $\beta_1(\omega)$ on a sample from the medium 1 (see Fig.1.1). We assume that the symmetry is broken in the z direction and that the optical response of the medium 1 is linear. In this configuration the second harmonic radiation can be traced in both the transmitted and the reflected beams emerging from the interface. The choice of which component to measure is mainly

a question of experimental convenience. In our case, we are forced to measure the SHG in reflection geometry because the lower surface of the medium 2 is not transparent. With reference to the Fig.1.1, we call n_1 the refraction index of the first medium and n_2 the refraction index of the second medium. Besides, we assume that in both of them the dispersion and losses are negligible. Let us label with 0 the interfacial layer, that, as we said previously, has $n_0 = 1$ as refraction index. In the interfacial layer the polarization defined in the (1.14) is located. Then, we can calculate the SH radiation propagating in the medium 1.

In the following, we will consider the case where the fields have one of this two linear polarizations: electric field oscillating in the incidence plane, indicated with unit vector p ; and electric field oscillating perpendicularly to the incidence plane, indicated with s . The geometry is shown in Fig.1.2. Then, first of all, let us to find the geometric relations between the fields components in the two coordinates systems, the laboratory frame and the (s,p) reference frame.

Let us label with $E_{s1}(2\omega)$, $E_{p1}(2\omega)$, $E_{s2}(2\omega)$ and with $E_{p2}(2\omega)$ the components s and p of the beam at frequency 2ω in the media 1 and 2, respectively.

Let us start from the case in which the SH radiation has polarization in the direction p . In this case, the components of the electric field in the two media

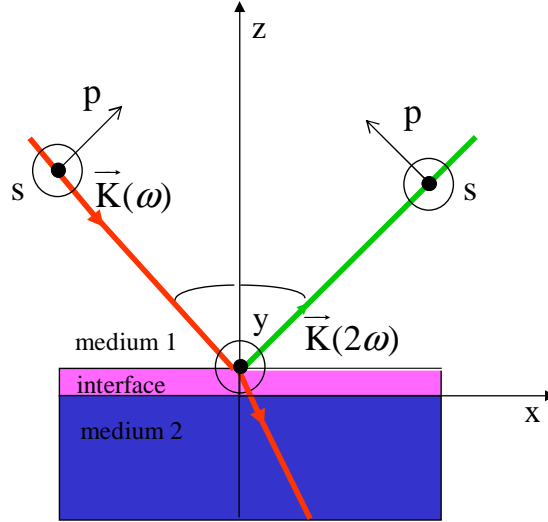


Figure 1.2: The coordinate system used to describe to solutions of the Maxwell equations. We have illustrate the reference frame (s, p) and the laboratory frame (x, y, z) .

are:

$$E_{x1}(2\omega) = -E_{p1}(2\omega) \cos \beta_1(2\omega)$$

$$E_{y1}(2\omega) = 0$$

$$E_{z1}(2\omega) = E_{p1}(2\omega) \sin \beta_1(2\omega) \tag{1.25}$$

$$E_{x2}(2\omega) = E_{p2}(2\omega) \cos \beta_2(2\omega)$$

$$E_{y2}(2\omega) = 0$$

$$E_{z2}(2\omega) = E_{p2}(2\omega) \sin \beta_2(2\omega).$$

By means of the relation $|E| = \frac{c}{n}|B| = \frac{c}{n}\mu_0|H|$, we obtain the components of the magnetic field:

$$\begin{aligned}
 H_{x1}(2\omega) &= 0 \\
 H_{y1}(2\omega) &= -\frac{n_1 E_{p1}(2\omega)}{c\mu_0} \\
 H_{z1}(2\omega) &= 0 \\
 H_{x2}(2\omega) &= 0 \\
 H_{y2}(2\omega) &= -\frac{n_2 E_{p2}(2\omega)}{c\mu_0} \\
 H_{z2}(2\omega) &= 0.
 \end{aligned} \tag{1.26}$$

Replacing E_{x1} and E_{x2} in the first equation of (1.23) and H_{y1} and H_{y2} in the second equation of (1.24), we get the p polarized field at frequency 2ω in the plane $z = 0$:

$$\begin{aligned}
 E_{p1}(z = 0, 2\omega) &= \frac{1}{n_2 \cos \beta_1(2\omega) + n_1 \cos \beta_2(2\omega)} \frac{i2\omega}{\varepsilon_0 c} \left[n_1 n_2 \sin \beta_1(2\omega) P_{0z}^s + \right. \\
 &\quad \left. - \cos \beta_2(2\omega) P_{0x}^s \right] e^{i(k_x x - 2\omega t)}.
 \end{aligned} \tag{1.27}$$

When the second harmonic radiation is s polarized, the components of the electric field in the media 1 and 2 are:

$$\begin{aligned}
 E_{x1}(2\omega) &= 0 \\
 E_{y1}(2\omega) &= E_{s1} \\
 E_{z1}(2\omega) &= 0 \\
 E_{x2}(2\omega) &= 0 \\
 E_{y2}(2\omega) &= E_{s2} \\
 E_{z2}(2\omega) &= 0,
 \end{aligned} \tag{1.28}$$

while, the components of the magnetic field are:

$$\begin{aligned}
 H_{x1}(2\omega) &= -\frac{n_1 E_{s1}}{c\mu_0} \cos \beta_1(2\omega) \\
 H_{y1}(2\omega) &= 0 \\
 H_{z1}(2\omega) &= \frac{n_1 E_{s1}}{c\mu_0} \sin \beta_1(2\omega) \\
 H_{x2}(2\omega) &= \frac{n_2 E_{s2}}{c\mu_0} \cos \beta_2(2\omega) \\
 H_{y2}(2\omega) &= 0 \\
 H_{z2}(2\omega) &= \frac{n_2 E_{s2}}{c\mu_0} \sin \beta_2(2\omega).
 \end{aligned} \tag{1.29}$$

Substituting the first and the fourth of the (1.29) in the first of (1.24), and remembering that $E_{s1}(2\omega) = E_{s2}(2\omega)$, we obtain the s polarized second harmonic

radiation at the interface:

$$E_{s1}(z = 0, 2\omega) = \frac{1}{n_1 \cos \beta_1(2\omega) + n_2 \cos \beta_2(2\omega)} \frac{i2\omega}{\varepsilon_0 c} P_{0y}^s e^{i(k_x x - 2\omega t)}. \quad (1.30)$$

In order to express the second harmonic field in a more compact notation, we calculate the field $E_0(\omega)$ in terms of the input field $E_1(\omega)$. To this purpose, we start from the relations which connect the fields in the media 1 and 2 in the (s, p) reference frame:

$$E_{p2}(\omega) = t_p E_{p1}(\omega) \quad (1.31)$$

$$E_{s2}(\omega) = t_s E_{s1}(\omega),$$

where t_p and t_s are the Fresnel coefficients for the transmission of the fundamental beam from the medium 1 to the medium 2, for the p and s components, respectively. Then, the components of the field in the medium 2 in terms of $E_1(\omega)$, in

the laboratory frame, are given by:

$$\begin{aligned}
 E_{x2}(\omega) &= E_{p2}(\omega) \cos \beta_2(\omega) = t_p E_{p1}(\omega) \cos \beta_2(\omega) = \\
 &= t_p \frac{\cos \beta_2(\omega)}{\cos \beta_1(\omega)} E_{x1}(\omega) \\
 E_{y2}(\omega) &= E_{s2}(\omega) = t_s E_{s1}(\omega) = t_s E_{y1}(\omega)
 \end{aligned} \tag{1.32}$$

$$\begin{aligned}
 E_{z2}(\omega) &= E_{p2}(\omega) \sin \beta_2(\omega) = t_p E_{p1}(\omega) \sin \beta_2(\omega) = \\
 &= t_p \frac{\sin \beta_2(\omega)}{\sin \beta_1(\omega)} E_{z1}(\omega) = t_p \frac{n_1}{n_2} E_{z1}(\omega),
 \end{aligned}$$

where, in the last of the (1.32), we used the *Snell's law*:

$$n_1 \sin \beta_1(\omega) = n_2 \sin \beta_2(\omega).$$

Because the discontinuity relations for the fields $E_x(\omega)$, $E_y(\omega)$ and $D_z(\omega)$ across

the interface are:

$$\begin{aligned}
 E_{x0}(\omega) &= E_{x2}(\omega) \\
 E_{y0}(\omega) &= E_{y2}(\omega) \\
 D_{z0}(\omega) &= D_{z2}(\omega),
 \end{aligned} \tag{1.33}$$

we obtain, after straightforward calculations, the field $E_0(\omega)$ as function of the incident beam:

$$\begin{aligned} E_{x0}(\omega) &= t_p \frac{\cos \beta_2(\omega)}{\cos \beta_1(\omega)} E_{x1}(\omega) \\ E_{y0}(\omega) &= t_s E_{y1}(\omega) \\ E_{z0}(\omega) &= t_p n_1 n_2 E_{z1}(\omega). \end{aligned} \tag{1.34}$$

Since t_s and t_p are given by:

$$\begin{aligned} t_s &= \frac{2n_1 \cos \beta_1(\omega)}{n_1 \cos \beta_1(\omega) + n_2 \cos \beta_2(\omega)} \\ t_p &= \frac{2n_1 \cos \beta_1(\omega)}{n_2 \cos \beta_1(\omega) + n_1 \cos \beta_2(\omega)}, \end{aligned} \tag{1.35}$$

the (1.34) can be written as:

$$\begin{aligned} E_{x0}(\omega) &= L_{xx}(\omega) E_{x1}(\omega) \\ E_{y0}(\omega) &= L_{yy}(\omega) E_{y1}(\omega) \\ E_{z0}(\omega) &= L_{zz}(\omega) E_{z1}(\omega), \end{aligned} \tag{1.36}$$

where we put:

$$\begin{aligned} L_{xx}(\omega) &= \frac{2n_1 \cos \beta_2(\omega)}{n_2 \cos \beta_1(\omega) + n_1 \cos \beta_2(\omega)} \\ L_{yy}(\omega) &= \frac{2n_1 \cos \beta_1(\omega)}{n_1 \cos \beta_1(\omega) + n_2 \cos \beta_2(\omega)} \\ L_{zz}(\omega) &= \frac{2n_1^2 n_2 \cos \beta_1(\omega)}{n_2 \cos \beta_1(\omega) + n_1 \cos \beta_2(\omega)}. \end{aligned} \tag{1.37}$$

By means of the (1.37), we can express the (1.36) as:

$$E_{i0}(\omega) = L_{ii}(\omega)E_{i1}(\omega). \quad (1.38)$$

Physically, $\vec{L} = (L_{xx}, L_{yy}, L_{zz})$ can be considered as a macroscopic local field correction factor on the radiation from the polarization sheet due to the presence of the boundary surfaces. In fact, in absence of the surfaces all $L_{ii}(\omega)$ become unity and the (1.38) reduces to $E_{i0} = E_{i1}$.

In analogy with the (1.37) we define the Fresnel factors for the field at frequency 2ω :

$$\begin{aligned} L_{xx}(2\omega) &= \frac{2n_1 \cos \beta_2(2\omega)}{n_2 \cos \beta_1(2\omega) + n_1 \cos \beta_2(2\omega)} \\ L_{yy}(2\omega) &= \frac{2n_1 \cos \beta_1(2\omega)}{n_1 \cos \beta_1(2\omega) + n_2 \cos \beta_2(2\omega)} \\ L_{zz}(2\omega) &= \frac{2n_1^2 n_2 \cos \beta_1(2\omega)}{n_2 \cos \beta_1(2\omega) + n_1 \cos \beta_2(2\omega)}. \end{aligned} \quad (1.39)$$

Inserting $L_{xx}(2\omega)$ and $L_{zz}(2\omega)$ into the (1.27), we obtain the following expression for the component of the second harmonic field parallel to the incidence plane:

$$\begin{aligned} E_{p1}(z = 0, 2\omega) &= \frac{i2\omega}{2\varepsilon_0 c n_1 \cos \beta_1(2\omega)} \left[\sin \beta_1(2\omega) L_{zz}(2\omega) P_{0z}^s + \right. \\ &\quad \left. + \cos \beta_1(2\omega) L_{xx}(2\omega) P_{0x}^s \right] e^{i(k_x x - 2\omega t)}. \end{aligned} \quad (1.40)$$

Inserting $L_{yy}(2\omega)$ in the (1.30), we obtain the second harmonic field perpendicular to the incidence plane:

$$E_{s1}(z = 0, 2\omega) = \frac{i2\omega}{2\varepsilon_0cn_1 \cos \beta_1(2\omega)} L_{yy}(2\omega) P_{0y}^s e^{i(k_x x - 2\omega t)}. \quad (1.41)$$

The (1.40) and (1.41) can be written by using a more general notation:

$$E_{1\alpha}(z = 0, 2\omega) = \frac{2i\omega}{2\varepsilon_0cn_1 \cos \beta_1(2\omega)} \widehat{e}_\alpha(2\omega)_i L_{ii}(2\omega) P_{0i}^s e^{i(k_x x - 2\omega t)}, \quad (1.42)$$

where we labeled with α s or p and with $\widehat{e}_\alpha(2\omega)$ the unit polarization vector for the wave at frequency 2ω , that is:

$$\widehat{e}_s(2\omega) = (0, 1, 0) \quad (1.43)$$

and

$$\widehat{e}_p(2\omega) = (-\cos \beta_1(2\omega), 0, \sin \beta_1(2\omega)). \quad (1.44)$$

The (1.42) is the field radiated from the polarization sheet \vec{P}^s . All the geometric factors resulting from the reflection and refraction are contained in the coefficients $L_{ii}(2\omega)$.

The wave at frequency 2ω propagating in the medium 1 and satisfying in $z = 0$ the boundary condition (1.42) has then the following form:

$$E_{1\alpha}(z, 2\omega) = E_{1\alpha}(z = 0, 2\omega) e^{ik_z z}, \quad (1.45)$$

with $k_z = \sqrt{\frac{4\omega^2}{c^2} - k_x^2} = \frac{2\omega}{c} \cos \beta_1(2\omega)$.

Let us express the SH radiation in terms of the intensity of the laser beam. The average intensity of a laser pulse with width T and area of spot A is given by:

$$I = \frac{U}{AT} \quad (1.46)$$

The intensity of an electromagnetic wave is connected to the module of the electric field by the following relation:

$$I(\omega) = 2\varepsilon_0 n c |\vec{E}(\omega)|^2. \quad (1.47)$$

Then, replacing the (1.42) in the (1.47) and using the (1.38), we can express the intensity of the second harmonic radiation as function of the laser beam intensity:

$$I_\alpha(2\omega) = \frac{\omega^2}{2n_1 c^3 \varepsilon_0 \cos^2 \beta_1(2\omega)} \left| \widehat{e}_{\alpha i}(2\omega) L_{ii}(2\omega) \chi_{ijh}^{(2)} L_{jj}(\omega) L_{hh}(\omega) I_{\alpha'}(\omega) \widehat{e}_{\alpha' j}(\omega) \widehat{e}_{\alpha' h}(\omega) \right|^2, \quad (1.48)$$

where $\widehat{e}_{\alpha j}(\omega)$ and $\widehat{e}_{\alpha' h}(\omega)$ are the unit polarization vector for the input field. Let us define a local effective surface second order susceptibility as follows:

$$\chi_{\alpha'\alpha}^{\text{eff}} = \widehat{e}_{\alpha i}(2\omega) L_{ii}(2\omega) \chi_{ijh}^{(2)} L_{jj}(\omega) L_{hh}(\omega) \widehat{e}_{\alpha' j}(\omega) \widehat{e}_{\alpha' h}(\omega), \quad (1.49)$$

that is a linear combination of the $\chi^{(2)}$ elements.

By using the (1.49), the (1.48) becomes:

$$I_\alpha(2\omega) = \frac{\omega^2}{2n_1 c^3 \varepsilon_0 \cos^2 \beta_1(2\omega)} |\chi_{\alpha'\alpha}^{\text{eff}}|^2 I_{\alpha'}^2(\omega). \quad (1.50)$$

Since the intensity of the second harmonic radiation is weak, it is useful to express the SH signal as photon number. The photon number N contained in a pulse with energy U and frequency ω is:

$$N(\omega) = \frac{U}{\hbar\omega}. \quad (1.51)$$

By using the (1.46), the photon number can be written as:

$$N(\omega) = \frac{I(\omega)}{\hbar\omega AT}. \quad (1.52)$$

Thus, from the (1.50) we get:

$$N_\alpha(2\omega) = \frac{\omega}{4\hbar n_1 c^3 \varepsilon_0 \cos^2 \beta_1(2\omega)} |\chi_{\alpha'\alpha}^{\text{eff}}|^2 I_{\alpha'}^2(\omega). \quad (1.53)$$

Therefore, with different combinations of input and output beam polarizations, the elements of $\chi_{\alpha'\alpha}^{\text{eff}}$ can be deduced from SHG measurements.

1.1.3 Second harmonic signal generated from a non-chiral and isotropic interface

The local second order susceptibility has 27 independent elements. As optical properties of a medium, it should have certain forms of symmetry that reflect the structural symmetry of the medium. Accordingly, some tensor elements are zero and others are related to each other, greatly reducing the total number of independent elements. In the following we will examine the case of a non-chiral

and isotropic interface. For a non-chiral interface, in the laboratory frame, the tensor χ_{ijh} ⁴ remains unchanged under reflection with respect to the planes xz and yz . Then, for the element χ_{xxy} , we obtain that:

$$\chi_{xxy} = \chi_{xx(-y)} = -\chi_{xxy}, \quad (1.54)$$

which implies that the elements with an odd number of y are zero. In the same way we can demonstrate that are vanish the elements whit an odd number of indexes x . Then, the non-vanishing components of the local second order susceptibility are:

$$\chi_{xxz}, \chi_{xzx}, \chi_{zxx}, \chi_{yyz}, \chi_{yzy}, \chi_{zyy}, \chi_{zzz}.$$

Besides, thanks to the isotropy property, the tensor χ_{ijh} remains unchanged under rotation around the axis z . For example, if we consider a rotation of 90° around the axis z , the non-vanishing elements of χ_{ijh} satisfy the following relations:

$$\begin{aligned} \chi_{xxz} &= \chi_{yyz} \\ \chi_{xzx} &= \chi_{yzy} \\ \chi_{zxx} &= \chi_{zyy}. \end{aligned} \quad (1.55)$$

⁴In the following section, in order to simplify the notation, we will neglect the apex (2).

Then, the independent elements of χ_{ijh} are four:

$$\chi_{xxz}, \quad \chi_{xzx}, \quad \chi_{zxx}, \quad \chi_{zzz}.$$

Considering the permutation intrinsic symmetry (see eq.(1.9)), we have additional relations:

$$\chi_{xxz} = \chi_{xzx} \tag{1.56}$$

$$\chi_{yyz} = \chi_{yzy}.$$

Finally, the independent non-vanishing components of the local second order susceptibility for a non-chiral and isotropic interface are two:

$$\chi_{xxz} = \chi_{xzx} = \chi_{zxx} = \chi_{yyz} = \chi_{yzy} = \chi_{zyy}$$

and

$$\chi_{zzz}.$$

Since we measure the second harmonic signal by varying the polarization direction of the incident and generated beams, we will address the determination of the elements of the effective susceptibility for different input output polarization combinations. When the laser beam is p polarized, we can measure the second harmonic radiation p or s polarized, obtaining two combinations, pp and sp ⁵. For

⁵The first index refers to the input beam and the second to the wave at frequency 2ω .

the combination pp , the unit polarization vectors are given by ⁶:

$$\widehat{e}_p(\omega) = (\cos \beta_1, 0, \sin \beta_1)$$

and

$$\widehat{e}_p(2\omega) = (-\cos \beta_1, 0, \sin \beta_1),$$

Therefore the effective susceptibility is:

$$\begin{aligned} \chi_{pp}^{\text{eff}} = & -L_{xx}(2\omega)\chi_{xxx}L_{xx}^2 \cos^3 \beta_1 - 2L_{xx}(2\omega) \cos^2 \beta_1 \sin \beta_1 \chi_{xxz}L_{xx}(\omega)L_{zz}(\omega) \\ & - L_{xx}(2\omega)\chi_{xzz}L_{zz}\omega^2 \sin^2 \beta_1 \cos \beta_1 + L_{zz}(2\omega) \sin \beta_1 \chi_{zxx} \cos^2 \beta_1 L_{xx}^2(\omega) + \\ & + 2L_{zz}(2\omega)\chi_{zzx}L_{zz}(\omega)L_{xx}(\omega) \sin^2 \beta_1 \cos \beta_1 + L_{zz}(2\omega) \sin^2 \beta_1 \chi_{zzz}L_{zz}^2(\omega). \end{aligned} \quad (1.57)$$

In the case of the ps polarization combination, the unit polarization vectors are given by:

$$\widehat{e}_p(\omega) = (\cos \beta_1, 0, \sin \beta_1)$$

and

$$\widehat{e}_s(2\omega) = (0, 1, 0).$$

Therefore, the effective susceptibility is:

$$\begin{aligned} \chi_{ps}^{\text{eff}} = & L_{yy}(2\omega)\chi_{yxx} \cos^2 \beta_1 L_{xx}(\omega) + L_{yy}(2\omega)\chi_{yzz} \sin^2 \beta_1 L_{zz}(\omega) + \\ & + 2L_{yy}(2\omega)\chi_{yxz} \cos \beta_1 \sin \beta_1 L_{xz}(\omega)L_{zx}(\omega). \end{aligned} \quad (1.58)$$

⁶In the following we will consider $\beta_1(\omega) = \beta_1(2\omega) = \beta_1$, because we neglected the dispersion of the medium 1.

When the input beam is s polarized, the effective susceptibility tensor for the polarization combinations ss and sp are given by:

$$\chi_{ss}^{\text{eff}} = L_{yy}(2\omega)\chi_{yyy}L_{yy}(\omega)L_{yy}(\omega), \quad (1.59)$$

and

$$\chi_{sp}^{\text{eff}} = L_{zz}(2\omega)\chi_{zyy}L_{yy}^2(\omega)\sin\beta_1 - L_{xx}(2\omega)\chi_{xyy}L_{yy}^2(\omega)\cos\beta_1 \quad (1.60)$$

Now we specify the (1.57)-(1.60) in the case of a non-chiral and isotropic interface. Substituting the symmetry relations obtained above, the components of the effective susceptibility become:

$$\begin{aligned} \chi_{pp}^{\text{eff}} &= -2L_{xx}(2\omega)\chi_{xxz}L_{xx}(\omega)L_{zz}(\omega)\cos^2\beta_1\sin\beta_1 \\ &+ L_{zz}(2\omega)\chi_{zxx}L_{xx}^2(\omega)\sin\beta_1\cos^2\beta_1 + L_{zz}(2\omega)\chi_{zzz}L_{zz}^2(\omega)\sin^3\beta_1 \\ \chi_{ps}^{\text{eff}} &= 0 \\ \chi_{ss}^{\text{eff}} &= 0 \end{aligned} \quad (1.61)$$

$$\chi_{sp}^{\text{eff}} = L_{zz}(2\omega)\chi_{zyy}L_{yy}^2(\omega)\sin\beta_1.$$

Thus, independently by the polarization of the incident beam (p or s), the second harmonic radiation generated by an isotropic non-chiral surface has no components in the direction s .

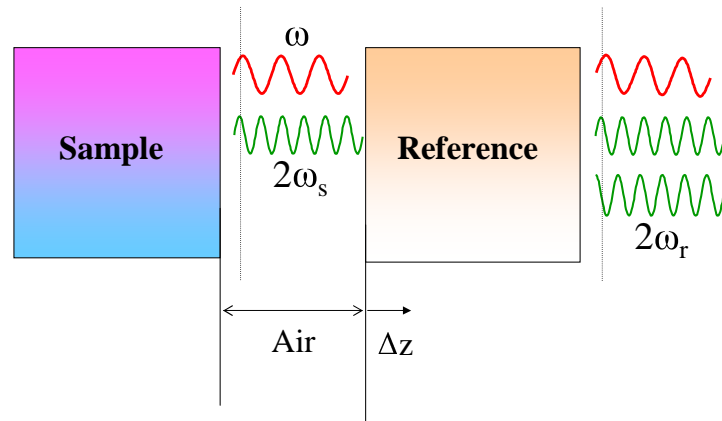


Figure 1.3: General principle for the appearance of phase between two SHG media separated by air.

1.1.4 Homodyne SHG measurements

The second order susceptibility is a complex quantity. Thus, it is characterized by an amplitude and a phase. Determining the phase of the second harmonic susceptibility is important for analyzing the orientation of dipoles present at the interface. The homodyne SHG (HSHG) measurements involve the insertion of a second source of SH radiation, usually a piece of quartz ⁷, into the beam reflected from the sample surface (see Fig.1.3). The reflected fundamental beam

⁷In the following we will call it reference.

will generate SH radiation in the quartz that is shifted in phase with respect to the SH radiation generated from the sample. In fact, because of the dispersion of the light in air the second harmonic radiation generated from the sample undergoes a phase shift with respect the incident field traveling collinearly with it. Therefore, when the second harmonic field is generated from the reference, it has a phase shift that differs from the first SH field:

$$\Delta k = 2\pi \frac{n(2\omega) - n(\omega)}{\lambda} z. \quad (1.62)$$

This phase shift causes the two SH field to interfere with one another. This interference can be made visible by translating the reference with respect to the sample. In order to calculate the interference pattern, we consider the following experimental configuration: the second harmonic beams are gaussian, the sample is placed after the waist of the input beam and the reference is translated in the region after the sample, where the gaussian beam expands.

The incident gaussian beam is given by:

$$E(z, r, \omega) = \frac{A}{q(z)} e^{ikz + i\frac{kr^2}{2q(z)}}, \quad (1.63)$$

where A is the complex amplitude of the field and $q(z)$ is given by:

$$\frac{1}{q(z)} = \frac{1}{R(z)} - i\frac{\lambda}{\pi w^2(z)}.$$

The behavior of q with z is the following:

$$q(z) = z - iz_0, \quad (1.64)$$

where z_0 is the Rayleigh length of the beam. For the beams at frequency 2ω , the

(1.63) becomes:

$$E_2(z, r, 2\omega) = \frac{A_2}{q_2(z)} e^{ik_2 z + i \frac{k_2 r^2}{2q_2(z)}}. \quad (1.65)$$

By imposing that the field at frequency ω generates E_2 by means of a thin piece of quartz, placed in \bar{z} , we have:

$$E_2(\bar{z}, r, \omega) = K\chi[E_1(\bar{z}, r, \omega)]^2 \quad \forall r. \quad (1.66)$$

The (1.66) implies that:

$$q_2(\bar{z}) = \frac{k_2}{2k_1} q_1(\bar{z}) \simeq q_1(\bar{z}), \quad (1.67)$$

where we assumed $k_2 \simeq 2k_1$ ⁸. Then, the two beams have the same focal parameters. Within this approximation, the amplitude of the second harmonic field is given by:

$$A_2 = K\chi A_1^2 \frac{1}{q(z)} e^{-i\Delta k z}, \quad (1.68)$$

⁸This assumption is valid in air with good approximation.

where Δk is given by the (1.62). Using the (1.68), we calculate the second harmonic fields generated from the sample and the reference:

$$E_2(z_s, r, 2\omega) = K \chi_s \frac{A_1^2}{q_1^2(z_s)} e^{(i\Delta k z_s + k_2 z_s + k_2 r / 2q_1(z_s))} \quad (1.69)$$

and

$$E_2(z_r, r, 2\omega) = K \chi_r \frac{A_1^2}{q_1^2(z_r)} e^{(i\Delta k z_r + k_2 z_r + k_2 r / 2q_1(z_r))}. \quad (1.70)$$

where χ_s and χ_r are the effective susceptibility of the sample and reference, z_s and z_r are the position of the sample and the reference, respectively. Because the total field is the sum of $E_2(z_s, r, 2\omega)$ and $E_2(z_r, r, 2\omega)$, the total intensity is given by:

$$I(2\omega) = |E_1(2\omega) + E_2(2\omega)|^2. \quad (1.71)$$

After straightforward calculation, we obtain:

$$I(2\omega) = K \frac{|\chi_s|^2}{1 + z_s^2/z_0^2} + K \frac{|\chi_r|^2}{1 + z_r^2/z_0^2} + 2K \frac{|\chi_s||\chi_r|}{\sqrt{(1 + z_s^2/z_0^2)(1 + z_r^2/z_0^2)}} \times \quad (1.72)$$

$$\times \cos(\Delta k(z_r - z_s) + \arctan(z_r/z_0) - \arctan(z_s/z_0) + \varphi_s - \varphi_r),$$

where K is a constant which includes the incident intensity and the revelation efficiency. Measuring the intensity of the total SH beam we can obtain, by a fitting procedure, $|\chi_s|$ and $|\chi_r|$ and the phase difference $\varphi_s - \varphi_r$.

1.2 Nonlocal Second Harmonic Generation

This section is devoted to a discussion of coupled electromagnetic waves in a nonlinear medium, which generates second harmonic radiation, for the case where the nonlocal response cannot be neglected. In particular, we will see how an incident optical radiation with a fixed frequency generates in a nonlinear medium the polarization \vec{P} . After that, by using the polarization as a source term in the Maxwell's equations, we will solve them, under certain approximations, to calculate the nonlocal second harmonic field generated from the medium.

1.2.1 Polarization in a nonlinear optical medium

For convenience, we rewrite in this section the Maxwell's equations in the case of absence of external charges and current:

$$\vec{\nabla} \times \vec{E} = -\frac{\partial \vec{B}}{\partial t} \quad (1.73)$$

$$\vec{\nabla} \cdot \vec{D} = 0 \quad (1.74)$$

$$\vec{\nabla} \times \vec{H} = \frac{\partial \vec{D}}{\partial t} \quad (1.75)$$

$$\vec{\nabla} \cdot \vec{B} = 0. \quad (1.76)$$

By taking the curl of the equation (1.73), by using the (1.75) and substituting the (1.20), we obtain a coupled nonlinear system of differential equations:

$$-\nabla^2 \vec{E} + \vec{\nabla}(\vec{\nabla} \cdot \vec{E}) + \epsilon_0 \mu_0 \frac{\partial^2 \vec{E}}{\partial t^2} = -\mu_0 \frac{\partial^2 \vec{P}}{\partial t^2}, \quad (1.77)$$

where the polarization is a source term. When the nonlocal response of the material cannot be neglected the polarization is given by:

$$\begin{aligned} P_i(\vec{r}, t) = & \int \epsilon_0 \chi_{ij}^{(1)}(\vec{r} - \vec{r}', t - t') E_j(\vec{r}', t') d^3 r' dt' + \\ & + \int \chi_{ijh}^{(2)}(\vec{r} - \vec{r}', \vec{r} - \vec{r}'', t - t', t - t'') E_j(\vec{r}', t') E_h(\vec{r}'', t'') d^3 r' d^3 r'' dt' dt''. \end{aligned} \quad (1.78)$$

The general solution of the (1.77) with the (1.78) is extremely complicated. Then, in the following we will make some simplifying approximations: the pump non depletion approximation and the slowly varying amplitude approximation.

Let us start expressing the fields in the Fourier transform. From the definition given in the (1.78), the polarization takes the form:

$$\begin{aligned} \tilde{P}_i(\vec{k}, \omega) = & \epsilon_0 \tilde{\chi}_{ij}^{(1)}(\vec{k}, \omega) E_j(\vec{k}, \omega) + \\ & + \int \tilde{\chi}_{ijh}^{(2)}(\vec{k}, \vec{k}', \vec{k}'', \omega, \omega', \omega'') E_j(\vec{k}', \omega') E_h(\vec{k}'', \omega'') \times \\ & \times \delta(\omega - \omega' - \omega'') \delta(\vec{k} - \vec{k}' - \vec{k}'') d^3 k' d^3 k'' d\omega' d\omega'', \end{aligned} \quad (1.79)$$

where δ functions imply that $\tilde{\chi}_{ijh}^{(2)}$ is a function of only two frequencies and two wave vectors⁹.

Since the $P_i(\vec{r}, t)$ is a physically measurable quantity, it must be real and hence the Fourier transform $\tilde{P}_i(\vec{k}, \omega)$ satisfies the following relation:

$$\tilde{P}_i(\vec{k}, \omega) = \tilde{P}_i^*(-\vec{k}, -\omega).$$

Obviously, also the electric field must be real. Hence the Fourier transform $\tilde{E}_j(\vec{k}', \omega')$ must obey an analogous condition:

$$\tilde{E}_j(\vec{k}', \omega') = \tilde{E}_j^*(-\vec{k}', -\omega').$$

Since the fields and the polarization are related to each other through the susceptibilities¹⁰, they have to satisfy the following relations:

$$\left. \begin{aligned} \tilde{\chi}_{ij}^{(1)}(\vec{k}, \omega) &= \tilde{\chi}_{ij}^{*(1)}(-\vec{k}, -\omega) \\ \tilde{\chi}_{ijh}^{(2)}(\vec{k}', \vec{k}'', \omega', \omega'') &= \tilde{\chi}_{ijh}^{*(2)}(-\vec{k}', -\vec{k}'', -\omega', -\omega''). \end{aligned} \right\} \text{reality conditions}$$

According to the intrinsic permutation symmetry (see eq. (1.9)), we can interchange the indexes j and h obtaining:

$$\tilde{\chi}_{ijh}^{(2)}(\vec{k}', \vec{k}'', \omega', \omega'') = \tilde{\chi}_{ihj}^{(2)}(\vec{k}'', \vec{k}', \omega'', \omega'), \quad \text{intrinsic symmetry condition.}$$

⁹For this reason in the following we will indicate $\tilde{\chi}_{ijh}^{(2)}$ only as a function of two frequencies and two wave vectors.

¹⁰Really $\tilde{\chi}_{ij}^{(1)}(\vec{k}, \omega)$ and $\tilde{\chi}_{ijh}^{(2)}(\vec{k}', \vec{k}'', \omega', \omega'')$ are the Fourier transform of the susceptibilities $\tilde{\chi}_{ij}^{(1)}(\vec{r} - \vec{r}', t - t')$ and $\tilde{\chi}_{ijh}^{(2)}(\vec{r} - \vec{r}', \vec{r} - \vec{r}'', t - t', t - t'')$, but in order to simplify the notation we call them susceptibility of the first and second order, respectively.

In most materials, the nonlocal dependence is small. So, the tensors $\tilde{\chi}_{ij}^{(1)}(\vec{k}, \omega)$ and $\tilde{\chi}_{ijh}^{(2)}(\vec{k}', \vec{k}'', \omega', \omega'')$ can be expanded into a power series of \vec{k} and the expansion can be truncated to the first order:

$$\tilde{\chi}_{ij}^{(1)}(\vec{k}, \omega) = \tilde{\chi}_{ij}^{(1)}(0, \omega) + \left(\frac{\partial \tilde{\chi}_{ij}^{(1)}(\vec{k}, \omega)}{\partial k_h} \right)_{\vec{k}=0} k_h$$

and

$$\begin{aligned} \tilde{\chi}_{ijh}^{(2)}(\vec{k}', \vec{k}'', \omega', \omega'') &= \tilde{\chi}_{ijh}^{(2)}(0, \omega', \omega'') + \left(\frac{\partial \tilde{\chi}_{ijh}^{(2)}(\vec{k}', \vec{k}'', \omega', \omega'')}{\partial k'_l} \right)_{\vec{k}'=0, \vec{k}''=0} k'_l + \\ &+ \left(\frac{\partial \tilde{\chi}_{ijh}^{(2)}(\vec{k}', \vec{k}'', \omega', \omega'')}{\partial k''_l} \right)_{\vec{k}'=0, \vec{k}''=0} k''_l. \end{aligned}$$

By putting:

$$\begin{aligned} \gamma_{ijh}(0, \omega) &= \left(\frac{\partial \tilde{\chi}_{ij}^{(1)}(\vec{k}, \omega)}{\partial k_h} \right)_{\vec{k}=0} \\ \gamma_{ijhl}(\omega', \omega'') &= \left(\frac{\partial \tilde{\chi}_{ijh}^{(2)}(\vec{k}', \vec{k}'', \omega', \omega'')}{\partial k'_h} \right)_{\vec{k}'=0, \vec{k}''=0} \\ \bar{\gamma}_{ijhl}(\omega', \omega'') &= \left(\frac{\partial \tilde{\chi}_{ijh}^{(2)}(\vec{k}', \vec{k}'', \omega', \omega'')}{\partial k''_h} \right)_{\vec{k}'=0, \vec{k}''=0}, \end{aligned}$$

the susceptibilities take the form:

$$\tilde{\chi}_{ij}^{(1)}(\vec{k}, \omega) = \tilde{\chi}_{ij}^{(1)}(0, \omega) + \gamma_{ijh}(0, \omega) k_h \quad (1.80)$$

$$\tilde{\chi}_{ijh}^{(2)}(\vec{k}', \vec{k}'', \omega', \omega'') = \tilde{\chi}_{ijh}^{(2)}(0, \omega', \omega'') + \gamma_{ijhl}(\omega', \omega'') k'_l + \bar{\gamma}_{ijhl}(\omega', \omega'') k''_l, \quad (1.81)$$

where $\gamma_{ijh}(0, \omega)$ and $\bar{\gamma}_{ijhl}(\omega', \omega'')$ are tensors of the third and fourth order, respectively, depending on the frequency.

By using the reality and intrinsic symmetry conditions, the (1.80) and (1.81) have

to satisfy the following relations:

$$\left. \begin{aligned} \tilde{\chi}_{ij}^{(1)}(0, \omega) &= \tilde{\chi}_{ij}^{*(1)}(0, -\omega) \\ \gamma_{ijh}(0, \omega) &= -\gamma_{ijh}^*(0, -\omega) \\ \tilde{\chi}_{ijh}^{(2)}(0, \omega', \omega'') &= \tilde{\chi}_{ijh}^{*(2)}(0, -\omega', -\omega'') \\ \gamma_{ijhl}(\omega', \omega'') &= -\gamma_{ijhl}^*(-\omega', -\omega'') \\ \bar{\gamma}_{ijhl}(\omega', \omega'') &= -\bar{\gamma}_{ijhl}^*(-\omega', -\omega'') \end{aligned} \right\} \text{reality conditions}$$

and

$$\left. \begin{aligned} \tilde{\chi}_{ijh}^{(2)}(0, \omega', \omega'') &= \tilde{\chi}_{ihj}^{(2)}(0, \omega'', \omega') \\ \gamma_{ijhl}(\omega', \omega'') &= \bar{\gamma}_{ihjl}(\omega'', \omega') \\ \bar{\gamma}_{ijhl}(\omega', \omega'') &= \gamma_{ihjl}(\omega'', \omega'). \end{aligned} \right\} \text{intrinsic symmetry conditions}$$

Substituting the (1.80) and (1.81), the polarization $\tilde{P}_i(\vec{k}, \omega)$ can be written as:

$$\begin{aligned} \tilde{P}_i(\vec{k}, \omega) &= \epsilon_0 [\tilde{\chi}_{ij}^{(1)}(0, \omega) + \gamma_{ijh}(0, \omega)k_h] E_j(\vec{k}, \omega) + \\ &+ \int [\tilde{\chi}_{ijh}^{(2)}(0, \omega', \omega'') + \gamma_{ijhl}(\omega', \omega'')k'_l + \bar{\gamma}_{ijhl}(\omega', \omega'')k''_l] E_j(\vec{k}', \omega') E_h(\vec{k}'', \omega'') \times \\ &\times \delta(\omega - \omega' - \omega'') \delta(\vec{k} - \vec{k}' - \vec{k}'') d^3k' d^3k'' d\omega' d\omega''. \end{aligned} \quad (1.82)$$

By calculating Fourier antitransform of $\tilde{P}_i(\vec{k}, \omega)$ respect to \vec{k} , we obtain:

$$\begin{aligned}
P_i(\vec{r}, \omega) = & \epsilon_0 \tilde{\chi}_{ij}^{(1)}(0, \omega) E_j(\vec{r}, \omega) - i \epsilon_0 \gamma_{ijh}(0, \omega) \frac{\partial}{\partial x_h} E_j(\vec{r}, \omega) + \\
& + \int d\omega' d\omega'' \tilde{\chi}_{ijh}^{(2)}(0, \omega', \omega'') E_j(\vec{r}, \omega') E_h(\vec{r}, \omega'') \delta(\omega - \omega' - \omega'') + \\
& - i \int d\omega' d\omega'' \gamma_{ijhl}(\omega', \omega'') \frac{\partial}{\partial x_l} E_j(\vec{r}, \omega') E_h(\vec{r}, \omega'') \delta(\omega - \omega' - \omega'') + \\
& - i \int d\omega' d\omega'' \bar{\gamma}_{ijhl}(\omega', \omega'') E_j(\vec{r}, \omega') \frac{\partial}{\partial x_l} E_h(\vec{r}, \omega'') \delta(\omega - \omega' - \omega''). \quad (1.83)
\end{aligned}$$

We consider now a monochromatic wave at frequency $\bar{\omega}$ that impinges onto the material. In order to take into account the coupling between the first and the second harmonic field, we substitute the expression:

$$E_j(\vec{r}, \omega) = E_{j, \bar{\omega}}(\vec{r}) \delta(\omega - \bar{\omega}) + E_{j, 2\bar{\omega}}(\vec{r}) \delta(\omega - 2\bar{\omega}) + c.c.,$$

into the (1.83). In this way we get:

$$P_i(\vec{r}, \omega) = P_{i, \bar{\omega}}(\vec{r}) \delta(\omega - \bar{\omega}) + P_{i, 2\bar{\omega}}(\vec{r}) \delta(\omega - 2\bar{\omega}) + c.c., \quad (1.84)$$

where the first order polarization $P_{i,\bar{\omega}}(\vec{r})$ is given by:

$$\begin{aligned}
P_{i,\bar{\omega}}(\vec{r}) = & \epsilon_0 \tilde{\chi}_{ij}^{(1)}(0, \bar{\omega}) E_{j,\bar{\omega}}(\vec{r}) - i\epsilon_0 \gamma_{ijh}(\bar{\omega}) \frac{\partial}{\partial x_h} E_{j,\bar{\omega}}(\vec{r}) + \\
& + \tilde{\chi}_{ijh}^{(2)}(0, 0, -\bar{\omega}, 2\bar{\omega}) E_{j,\bar{\omega}}^*(\vec{r}) E_{h,2\bar{\omega}}(\vec{r}) + \tilde{\chi}_{ijh}^{(2)}(0, 0, 2\bar{\omega}, -\bar{\omega}) E_{j,2\bar{\omega}}(\vec{r}) E_{h,\bar{\omega}}^*(\vec{r}) + \\
& - i\gamma_{ijhl}(-\bar{\omega}, 2\bar{\omega}) \frac{\partial}{\partial x_l} E_{j,\bar{\omega}}^*(\vec{r}) E_{h,2\bar{\omega}}(\vec{r}) - i\gamma_{ijhl}(2\bar{\omega}, -\bar{\omega}) \frac{\partial}{\partial x_l} E_{j,2\bar{\omega}}(\vec{r}) E_{h,\bar{\omega}}^*(\vec{r}) + \\
& - i\bar{\gamma}_{ijhl}(-\bar{\omega}, 2\bar{\omega}) E_{j,\bar{\omega}}^*(\vec{r}) \frac{\partial}{\partial x_l} E_{h,2\bar{\omega}}(\vec{r}) - i\bar{\gamma}_{ijhl}(2\bar{\omega}, -\bar{\omega}) E_{j,2\bar{\omega}}(\vec{r}) \frac{\partial}{\partial x_l} E_{h,\bar{\omega}}^*(\vec{r}), \quad (1.85)
\end{aligned}$$

and the second order polarization $P_{i,2\bar{\omega}}(\vec{r})$ is given by:

$$\begin{aligned}
P_{i,2\bar{\omega}}(\vec{r}) = & \epsilon_0 \tilde{\chi}_{ij}^{(1)}(0, 2\bar{\omega}) E_{j,2\bar{\omega}}(\vec{r}) - i\epsilon_0 \gamma_{ijh}(2\bar{\omega}) \frac{\partial}{\partial x_h} E_{j,2\bar{\omega}}(\vec{r}) + \quad (1.86) \\
& + \tilde{\chi}_{ijh}^{(2)}(0, 0, \bar{\omega}, \bar{\omega}) E_{j,\bar{\omega}}(\vec{r}) E_{h,\bar{\omega}}(\vec{r}) - i\gamma_{ijhl}(\bar{\omega}, \bar{\omega}) \frac{\partial}{\partial x_l} E_{j,\bar{\omega}}(\vec{r}) E_{h,\bar{\omega}}(\vec{r}) + \\
& - i\bar{\gamma}_{ijhl}(\bar{\omega}, \bar{\omega}) E_{j,\bar{\omega}}(\vec{r}) \frac{\partial}{\partial x_l} E_{h,\bar{\omega}}(\vec{r}).
\end{aligned}$$

In order to obtain last relations we used the pump non depletion approximation, that is we neglected the terms $E_{i,\bar{\omega}} E_{j,2\bar{\omega}}$ which describe the energy transfer between the pump and the field at frequency $2\bar{\omega}$. As consequence of this approximation, we neglected also the terms $E_{i,2\bar{\omega}} E_{j,2\bar{\omega}}$. We note that the weak nonlocal response of the material lead to the appearance, in the second order polarization, of terms proportional to the product between the electric field and the gradient of the electric field. These terms are responsible of the second harmonic generation in a centrosymmetric material, as we will show at the end of this section.

The susceptibilities tensors should have certain forms of symmetry that reflect the structural symmetry of the medium. We are interested to centrosymmetric material¹¹. For it, the electric field and the polarization have to satisfy the following relations:

$$E'_i(\vec{r}', \omega) = -E_i(-\vec{r}, \omega)$$

$$P'_i(\vec{r}', \omega) = -P_i(-\vec{r}, \omega)$$

where $\vec{r}' = -\vec{r}$ (inversion operation).

By calculating $P'_i(\vec{r}', \omega)$ and $-P_i(-\vec{r}, \omega)$, we have that:

$$\left. \begin{array}{l} \tilde{\gamma}_{ijh}(0, \omega) = 0 \\ \tilde{\chi}_{ijh}^{(2)}(0, \bar{\omega}, \bar{\omega}) = 0 \end{array} \right\} \text{centrosymmetry conditions}$$

Therefore, in the bulk of materials possessing a center of symmetry only nonlocal second harmonic radiation can be generated because only the components of the nonlocal susceptibilities $\tilde{\chi}_{ij}$, γ_{ijhl} and $\bar{\gamma}_{ijhl}$ are different to zero. Such SH radiation

¹¹The material we use in our experiment, muscovite mica, is centrosymmetric.

is due to the following polarization:

$$\begin{aligned}
P_i(\vec{r}, \omega) = & \epsilon_0 \tilde{\chi}_{ij}^{(1)}(0, \bar{\omega}) E_{j, \bar{\omega}}(\vec{r}) \delta(\omega - \bar{\omega}) + \\
& + [\epsilon_0 \tilde{\chi}_{ij}^{(1)}(0, 2\bar{\omega}) E_{j, 2\bar{\omega}}(\vec{r}) + \\
& - i\gamma_{ijhl}(\bar{\omega}, \bar{\omega}) \frac{\partial}{\partial x_l} E_{j, \bar{\omega}}(\vec{r}) E_{h, \bar{\omega}}(\vec{r}) + \\
& - i\bar{\gamma}_{ijhl}(\bar{\omega}, \bar{\omega}) E_{j, \bar{\omega}}(\vec{r}) \frac{\partial}{\partial x_l} E_{h, \bar{\omega}}(\vec{r})] \delta(\omega - 2\bar{\omega}). \quad (1.87)
\end{aligned}$$

Finally, taking into account the intrinsic symmetry conditions and by defining:

$$\Gamma_{ijhl}(\omega, \omega) = -2i\bar{\gamma}_{ijhl}(\omega, \omega),$$

we have:

$$\begin{aligned}
P_i(\vec{r}, \omega) = & \epsilon_0 \tilde{\chi}_{ij}^{(1)}(0, \bar{\omega}) E_{j, \bar{\omega}}(\vec{r}) \delta(\omega - \bar{\omega}) + \\
& + [\epsilon_0 \tilde{\chi}_{ij}^{(1)}(0, 2\bar{\omega}) E_{j, 2\bar{\omega}}(\vec{r}) + \Gamma_{ijhl}(\bar{\omega}, \bar{\omega}) E_{j, \bar{\omega}}(\vec{r}) \frac{\partial}{\partial x_l} E_{h, \bar{\omega}}(\vec{r})] \delta(\omega - 2\bar{\omega}). \quad (1.88)
\end{aligned}$$

This relation constitutes the main result of this section. We will apply it in the following sections to calculate the nonlocal second harmonic radiation generated from a centrosymmetric medium.

1.2.2 Nonlocal Second Harmonic Radiation generated from centrosymmetric material

As said above, a centrosymmetric material generates only nonlocal second harmonic radiation. In this section, we will calculate it. Let us consider a reference

frame (*laboratory frame*), where the centrosymmetric medium is in the plane xy .

In particular, it occupies the region of $0 < z < d$. To obtain the nonlocal second harmonic radiation generated by it, we have to solve the equation:

$$-\nabla^2 \vec{E}(\vec{r}, \omega) + \vec{\nabla}(\vec{\nabla} \cdot \vec{E}(\vec{r}, \omega)) - \epsilon_0 \mu_0 \omega^2 \vec{E}(\vec{r}, \omega) = \mu_0 \omega^2 \vec{P}(\vec{r}, \omega), \quad (1.89)$$

where the polarization is given by (1.88). We suppose that in the regions with $z < 0$ and $z > d$ there is the vacuum. Thus, we have to solve also the equation:

$$\nabla^2 \vec{E}(\vec{r}, \omega) + \frac{\omega^2}{c^2} \vec{E}(\vec{r}, \omega) = 0 \quad \text{for } z < 0 \quad \text{and} \quad z > d. \quad (1.90)$$

By adding to (1.89) and (1.90) the condition of continuity, in $z = 0$ and in $z = d$, for E_x , E_y and D_z we can solve them. To this purpose, we suppose that the input field is a monochromatic wave, at frequency $\bar{\omega}$, which impinges on the material surface at $z = 0$:

$$E_i(z, \omega) = \mathcal{E}_{i, \bar{\omega}} e^{i\xi z} \delta(\omega - \bar{\omega}) + \mathcal{E}_{i, \bar{\omega}}^* e^{-i\xi z} \delta(\omega + \bar{\omega}), \quad i = x, y,$$

$$E_z(z, \omega) = 0 \quad z < 0.$$

This field is a solution of the equation (1.90) with the condition that $\xi^2 = \frac{\bar{\omega}^2}{c^2}$.

Inserting the polarization into (1.89), we obtain:

$$\nabla^2 E_{i, \bar{\omega}}(\vec{r}) + \frac{\bar{\omega}^2}{c^2} E_{i, \bar{\omega}}(\vec{r}) - \frac{\partial}{\partial x_i} (\vec{\nabla} \cdot \vec{E}_{\bar{\omega}}(\vec{r})) = -\frac{\bar{\omega}^2}{c^2} \tilde{\chi}_{ij}^{(1)}(0, \bar{\omega}) E_{j, \bar{\omega}}(\vec{r}), \quad (1.91)$$

and

$$\begin{aligned} \nabla^2 E_{i,2\bar{\omega}}(\vec{r}) + \frac{4\bar{\omega}^2}{c^2} E_{i,2\bar{\omega}}(\vec{r}) - \frac{\partial}{\partial x_i} (\vec{\nabla} \cdot \vec{E}_{2\bar{\omega}}(\vec{r})) = \\ - \frac{4\bar{\omega}^2}{c^2} \tilde{\chi}_{ij}^{(1)}(0, 2\bar{\omega}) E_{j,2\bar{\omega}}(\vec{r}) - 4\mu_0 \bar{\omega}^2 \Gamma_{ijkl}(\bar{\omega}, \bar{\omega}) E_{j,\bar{\omega}}(\vec{r}) \frac{\partial}{\partial x_l} E_{h,\bar{\omega}}(\vec{r}). \end{aligned} \quad (1.92)$$

We note the the pump non depletion approximation, made in previous section, led to an equation for the pump, the (1.91), in which there is no coupling between the pump and the wave at frequency $2\bar{\omega}$. Let us solve it. It is possible to show that the tensor $\tilde{\chi}_{ij}^{(1)}(0, \bar{\omega})$ is symmetric. Then, there is a reference frame where it is diagonal. The axes $\hat{a}, \hat{b}, \hat{c}$ of this reference frame are called *principal dielectric axes*. They are connected to the axes $\hat{i}, \hat{j}, \hat{k}$ of the laboratory frame by the following rotation matrix \mathbf{R} :

$$\begin{pmatrix} \hat{a} \\ \hat{b} \\ \hat{c} \end{pmatrix} = \mathbf{R} \begin{pmatrix} \hat{i} \\ \hat{j} \\ \hat{k} \end{pmatrix} = \begin{pmatrix} \cos \vartheta & \sin \vartheta & 0 \\ -\sin \vartheta & \cos \vartheta & 0 \\ 0 & 0 & 1 \end{pmatrix} \begin{pmatrix} \hat{i} \\ \hat{j} \\ \hat{k} \end{pmatrix}, \quad (1.93)$$

where we assumed that the axis \hat{c} coincides with the axis \hat{k} of the laboratory frame¹². Indicating with E_α ($\alpha = a, b, c$) the components of the electric field along the principal dielectric axes, we have that:

$$E_{i,\bar{\omega}} = R_{i\alpha}^{-1} E_{\alpha,\bar{\omega}}, \quad E_{i,2\bar{\omega}} = R_{i\alpha}^{-1} E_{\alpha,2\bar{\omega}}, \quad (1.94)$$

¹²We made this choice because the mica has the axis \hat{c} parallel to the axis \hat{k} of the laboratory frame.

After straightforward calculations, we obtain the (1.91) in the reference frame

$\hat{a}, \hat{b}, \hat{c}$:

$$\frac{d^2}{dz^2} E_{\gamma, \bar{\omega}}(z) + \frac{\bar{\omega}^2}{c^2} (1 + \tilde{\chi}_{\gamma\gamma}^{(1)}(0, \bar{\omega})) E_{\gamma, \bar{\omega}}(z) - \delta_{\gamma c} \frac{d^2}{dz^2} E_{c, \bar{\omega}}(z) = 0, \quad (1.95)$$

where we assumed that the field depends only on z . The solution of (1.95) is

given by:

$$E_{\gamma, \bar{\omega}}(z) = \mathcal{E}_{\gamma, \bar{\omega}} e^{i\eta_\gamma z}, \quad \text{with} \quad \eta_\gamma^2 = \frac{\bar{\omega}^2}{c^2} (1 + \tilde{\chi}_{\gamma\gamma}^{(1)}(0, \bar{\omega})) \quad \text{and} \quad \gamma = a, b,$$

$$E_{c, \bar{\omega}}(\vec{r}) = 0. \quad (1.96)$$

Now, we move on find the solution of equation (1.92). In order to do it, we

calculate the components of the tensor $\Gamma_{\gamma\alpha\beta z}$ along the dielectric axes by using

the matrix \mathbf{R} :

$$\Gamma_{\gamma\alpha\beta z}(\bar{\omega}, \bar{\omega}) = R_{\gamma i} \Gamma_{ijhz}(\bar{\omega}, \bar{\omega}) R_{j\alpha}^{-1} R_{h\beta}^{-1}.$$

Inserting last relation in the (1.92) we get the equation for the wave at frequency

$2\bar{\omega}$ in the reference frame $\hat{a}, \hat{b}, \hat{c}$:

$$\begin{aligned} \frac{d^2}{dz^2} E_{\gamma, 2\bar{\omega}}(z) + \frac{4\bar{\omega}^2}{c^2} (1 + \tilde{\chi}_{\gamma\gamma}^{(1)}(0, 2\bar{\omega})) E_{\gamma, 2\bar{\omega}}(z) - \delta_{\gamma c} \frac{d^2}{dz^2} E_{c, 2\bar{\omega}}(z) = \\ = -4\mu_0 \bar{\omega}^2 [A_\gamma e^{i2\eta_a z} + B_\gamma e^{i(\eta_a z + \eta_b)z} + C_\gamma e^{i2\eta_b z}], \end{aligned} \quad (1.97)$$

where we put:

$$A_\gamma = i\eta_a \Gamma_{\gamma aaz}(\bar{\omega}, \bar{\omega}) \mathcal{E}_{a,\bar{\omega}}^2, \quad (1.98)$$

$$B_\gamma = i [\eta_b \Gamma_{\gamma abz}(\bar{\omega}, \bar{\omega}) + \eta_a \Gamma_{\gamma baz}(\bar{\omega}, \bar{\omega})] \mathcal{E}_{a,\bar{\omega}} \mathcal{E}_{b,\bar{\omega}}, \quad (1.99)$$

$$C_\gamma = i\eta_b \Gamma_{\gamma bbz}(\bar{\omega}, \bar{\omega}), \mathcal{E}_{b,\bar{\omega}}^2, \quad (1.100)$$

and we assumed that also the $\tilde{\chi}_{ij}^{(1)}(0, 2\bar{\omega})$ tensor is diagonal in the principal dielectric axes reference frame. We note that the c component (*longitudinal wave*) of the field can be neglected because in $z > d$ there is the vacuum and the Maxwell's equations have no solution for a longitudinal wave.

We assume that the components a, b of the second harmonic field are given by:

$$E_{\gamma, 2\bar{\omega}}(z) = \mathcal{E}_{\gamma, 2\bar{\omega}}(z) e^{ik_\gamma z}, \quad \gamma = a, b, \quad (1.101)$$

with $k_\gamma^2 = \frac{4\bar{\omega}^2}{c^2} \left(1 + \tilde{\chi}_{\gamma\gamma}^{(1)}(0, 2\bar{\omega})\right)$. By calculating the second derivative of the field,

we have:

$$\frac{d^2}{dz^2} E_{\gamma, 2\bar{\omega}}(z) = \frac{d^2 \mathcal{E}_{\gamma, 2\bar{\omega}}(z)}{dz^2} e^{ik_\gamma z} + 2ik_\gamma \frac{d\mathcal{E}_{\gamma, 2\bar{\omega}}(z)}{dz} e^{ik_\gamma z} - k_\gamma^2 \mathcal{E}_{\gamma, 2\bar{\omega}}(z) e^{ik_\gamma z}. \quad (1.102)$$

We assume that the variation of the amplitude $\mathcal{E}_{\gamma, 2\bar{\omega}}(z)$ with z is small enough (slowly varying approximation) then that:

$$\frac{d^2 \mathcal{E}_{\gamma, 2\bar{\omega}}(z)}{dz^2} \ll \frac{d\mathcal{E}_{\gamma, 2\bar{\omega}}(z)}{dz} k_\gamma.$$

Thus, from the (1.102) we get:

$$\frac{d^2}{dz^2} E_{\gamma, 2\bar{\omega}}(z) \simeq 2ik_\gamma \frac{d\mathcal{E}_{\gamma, 2\bar{\omega}}(z)}{dz} e^{ik_\gamma z} - k_\gamma^2 \mathcal{E}_{\gamma, 2\bar{\omega}}(z) e^{ik_\gamma z}. \quad (1.103)$$

Through the use of the last equation, the (1.97) reduces to a first order differential equation:

$$\frac{d}{dz} \mathcal{E}_{\gamma, 2\bar{\omega}}(z) = \frac{2i\mu_0\bar{\omega}^2}{k_\gamma} [A_\gamma e^{i(2\eta_a - k_\gamma)z} + B_\gamma e^{i(\eta_a + \eta_b - k_\gamma)z} + C_\gamma e^{i(2\eta_b - k_\gamma)z}], \quad (1.104)$$

where we multiplied both of the members for $\frac{-ie^{-ik_\gamma z}}{2k_\gamma}$.

Finally, the amplitude of the field at frequency $2\bar{\omega}$ in $z = d$ is given integrating the second member of the (1.104):

$$\begin{aligned} \mathcal{E}_{\gamma, 2\bar{\omega}}(d) = id \frac{2\mu_0\bar{\omega}^2}{k_\gamma} & \left[A_\gamma e^{\frac{i(2\eta_a - k_\gamma)d}{2}} \text{sync} \left(\frac{(2\eta_a - k_\gamma)d}{2} \right) + \right. \\ & \left. + B_\gamma e^{\frac{i(\eta_a + \eta_b - k_\gamma)d}{2}} \text{sync} \left(\frac{(\eta_a + \eta_b - k_\gamma)d}{2} \right) + C_\gamma e^{\frac{i(2\eta_b - k_\gamma)d}{2}} \text{sync} \left(\frac{(2\eta_b - k_\gamma)d}{2} \right) \right], \end{aligned} \quad (1.105)$$

where we put $\mathcal{E}_{\gamma, 2\bar{\omega}}(0) = 0$.

We consider only the case where the beams are linearly polarized along the directions x and y . When the incident field is polarized along the axis x (*vertical polarization*), we have that $\mathcal{E}_{y, \bar{\omega}} = 0$. Then, the coefficients defined in the (1.98),

(1.99) and (1.100) become:

$$\begin{aligned}
A_a^v &= i\eta_a \Gamma_{aaaz}(\omega, \omega) \mathcal{E}_{x,\bar{\omega}}^2 \cos^2 \vartheta, \\
B_a^v &= i[\eta_b \Gamma_{abz}(\omega, \omega) + \eta_a \Gamma_{abaz}(\omega, \omega)] \mathcal{E}_{x,\bar{\omega}}^2 \sin \vartheta \cos \vartheta, \\
C_a^v &= i\eta_b \Gamma_{abbz}(\omega, \omega) \mathcal{E}_{x,\bar{\omega}}^2 \sin^2 \vartheta, \\
A_b^v &= i\eta_a \Gamma_{baaz}(\omega, \omega) \mathcal{E}_{x,\bar{\omega}}^2 \cos^2 \vartheta, \\
B_b^v &= i[\eta_b \Gamma_{babz}(\omega, \omega) + \eta_a \Gamma_{bbaz}(\omega, \omega)] \mathcal{E}_{x,\bar{\omega}}^2 \sin \vartheta \cos \vartheta, \\
C_b^v &= i\eta_b \Gamma_{bbbz}(\omega, \omega) \mathcal{E}_{x,\bar{\omega}}^2 \sin^2 \vartheta.
\end{aligned} \tag{1.106}$$

When the incident field is polarized along y (*horizontal polarization*), we have that $\mathcal{E}_{x,\bar{\omega}} = 0$. So, the (1.98), (1.99) and (1.100) take the form:

$$\begin{aligned}
A_a^h &= i\eta_a \Gamma_{aaaz}(\omega, \omega) \mathcal{E}_{y,\bar{\omega}}^2 \sin^2 \vartheta, \\
B_a^h &= -i[\eta_b \Gamma_{abz}(\omega, \omega) + \eta_a \Gamma_{abaz}(\omega, \omega)] \mathcal{E}_{y,\bar{\omega}}^2 \sin \vartheta \cos \vartheta, \\
C_a^h &= i\eta_b \Gamma_{abbz}(\omega, \omega) \mathcal{E}_{y,\bar{\omega}}^2 \cos^2 \vartheta, \\
A_b^h &= i\eta_a \Gamma_{baaz}(\omega, \omega) \mathcal{E}_{y,\bar{\omega}}^2 \sin^2 \vartheta, \\
B_b^h &= -i[\eta_b \Gamma_{babz}(\omega, \omega) + \eta_a \Gamma_{bbaz}(\omega, \omega)] \mathcal{E}_{y,\bar{\omega}}^2 \sin \vartheta \cos \vartheta, \\
C_b^h &= i\eta_b \Gamma_{bbbz}(\omega, \omega) \mathcal{E}_{y,\bar{\omega}}^2 \cos^2 \vartheta.
\end{aligned} \tag{1.107}$$

The components of the second harmonic field in the laboratory frame are connected to those along dielectric principal axes of the material by the following

relations:

$$\begin{aligned}
 E_{x,2\bar{\omega}}(d) &= E_{a,2\bar{\omega}}(d) \cos \vartheta + E_{b,2\bar{\omega}}(d) \sin \vartheta = \\
 &= \mathcal{E}_{a,2\bar{\omega}}(d) e^{ik_a d} \cos \vartheta + \mathcal{E}_{b,2\bar{\omega}}(d) e^{ik_b d} \sin \vartheta, \quad (1.108)
 \end{aligned}$$

$$\begin{aligned}
 E_{y,2\bar{\omega}}(d) &= E_{b,2\bar{\omega}}(d) \cos \vartheta - E_{a,2\bar{\omega}}(d) \sin \vartheta = \\
 &= \mathcal{E}_{b,2\bar{\omega}}(d) e^{ik_b d} \cos \vartheta - \mathcal{E}_{a,2\bar{\omega}}(d) e^{ik_a d} \sin \vartheta. \quad (1.109)
 \end{aligned}$$

The second harmonic signal vertically polarized is proportional to $|E_{x,2\bar{\omega}}(d)|^2$, whereas the second harmonic signal horizontally polarized is proportional to $|E_{y,2\bar{\omega}}(d)|^2$. The coefficients are the ones indicated in the (1.106), when the input field is vertically polarized, and the ones in the (1.107), when the input field is horizontally polarized. Then, after straightforward calculations, we obtain the second harmonic signals for four different input-output polarization combinations

in the laboratory frame:

$$\begin{aligned}
S_{vv} \propto & \left| \mathcal{E}_{x,\bar{\omega}}^2 \right|^2 \left| \frac{\eta_a}{k_a} \Gamma_{aaaz} e^{\frac{i(2\eta_a+k_a)d}{2}} \text{sync} \left(\frac{(2\eta_a - k_a)d}{2} \right) \cos^3 \vartheta + \right. \\
& + \left[\frac{\eta_b \Gamma_{aabz} + \eta_a \Gamma_{abaz}}{k_a} e^{\frac{i(\eta_a+\eta_b+k_a)d}{2}} \text{sync} \left(\frac{(\eta_a + \eta_b - k_a)d}{2} \right) + \right. \\
& + \left. \frac{\eta_a}{k_b} \Gamma_{baaz} e^{\frac{i(2\eta_a+k_b)d}{2}} \text{sync} \left(\frac{(2\eta_a - k_b)d}{2} \right) \right] \sin \vartheta \cos^2 \vartheta + \\
& + \left[\frac{\eta_b \Gamma_{babz} + \eta_a \Gamma_{bbaz}}{k_b} e^{\frac{i(\eta_a+\eta_b+k_b)d}{2}} \text{sync} \left(\frac{(\eta_a + \eta_b - k_b)d}{2} \right) + \right. \\
& + \left. \frac{\eta_b}{k_a} \Gamma_{abbz} e^{\frac{i(2\eta_b+k_a)d}{2}} \text{sync} \left(\frac{(2\eta_b - k_a)d}{2} \right) \right] \sin^2 \vartheta \cos \vartheta + \\
& \left. + \frac{\eta_b}{k_b} \Gamma_{bbbz} e^{\frac{i(2\eta_b+k_b)d}{2}} \text{sync} \left(\frac{(2\eta_b - k_b)d}{2} \right) \sin^3 \vartheta \right|^2, \tag{1.110}
\end{aligned}$$

$$\begin{aligned}
S_{hv} \propto & \left| \mathcal{E}_{y,\bar{\omega}}^2 \right|^2 \left| \frac{\eta_b}{k_a} \Gamma_{abbz} \cos^3 \vartheta e^{\frac{i(2\eta_b+k_a)d}{2}} \text{sync} \left(\frac{(2\eta_b - k_a)d}{2} \right) + \right. \\
& + \left[- \frac{\eta_b \Gamma_{aabz} + \eta_a \Gamma_{abaz}}{k_a} e^{\frac{i(\eta_a+\eta_b+k_a)d}{2}} \text{sync} \left(\frac{(\eta_a + \eta_b - k_a)d}{2} \right) \right. \\
& + \left. \frac{\eta_b}{k_b} \Gamma_{bbbz} e^{\frac{i(2\eta_b+k_b)d}{2}} \text{sync} \left(\frac{(2\eta_b - k_b)d}{2} \right) \right] \sin \vartheta \cos^2 \vartheta + \\
& + \left[- \frac{\eta_b \Gamma_{babz} + \eta_a \Gamma_{bbaz}}{k_b} e^{\frac{i(\eta_a+\eta_b+k_b)d}{2}} \text{sync} \left(\frac{(\eta_a + \eta_b - k_b)d}{2} \right) + \right. \\
& + \left. \frac{\eta_a}{k_a} \Gamma_{aaaz} e^{\frac{i(2\eta_a+k_a)d}{2}} \text{sync} \left(\frac{(2\eta_a - k_a)d}{2} \right) \right] \sin^2 \vartheta \cos \vartheta + \\
& \left. + \frac{\eta_a}{k_b} \Gamma_{baaz} \sin^3 \vartheta e^{\frac{i(2\eta_a+k_b)d}{2}} \text{sync} \left(\frac{(2\eta_a - k_b)d}{2} \right) \right|^2, \tag{1.111}
\end{aligned}$$

$$\begin{aligned}
S_{hh} \propto & \left| \mathcal{E}_{y,\bar{w}}^2 \right|^2 \left| \frac{\eta_b}{k_b} \Gamma_{bbbz} e^{\frac{i(2\eta_b+k_b)d}{2}} \text{sync} \left(\frac{(2\eta_b - k_b)d}{2} \right) \cos^3 \vartheta + \right. \\
& + \left[- \frac{\eta_b \Gamma_{babz} + \eta_a \Gamma_{bbaz}}{k_b} e^{\frac{i(\eta_a+\eta_b+k_b)d}{2}} \text{sync} \left(\frac{(\eta_a + \eta_b - k_b)d}{2} \right) + \right. \\
& \left. \left. - \frac{\eta_b}{k_a} \Gamma_{abbz} e^{\frac{i(2\eta_b+k_a)d}{2}} \text{sync} \left(\frac{(2\eta_b - k_a)d}{2} \right) \right] \sin \vartheta \cos^2 \vartheta + \right. \\
& + \left[\frac{\eta_b \Gamma_{aabz} + \eta_a \Gamma_{abaz}}{k_a} e^{\frac{i(\eta_a+\eta_b+k_a)d}{2}} \text{sync} \left(\frac{(\eta_a + \eta_b - k_a)d}{2} \right) + \right. \\
& \left. \left. + \frac{\eta_a}{k_b} \Gamma_{baaz} e^{\frac{i(2\eta_a+k_b)d}{2}} \text{sync} \left(\frac{(2\eta_a - k_b)d}{2} \right) \right] \sin^2 \vartheta \cos \vartheta + \right. \\
& \left. - \frac{\eta_a}{k_a} \Gamma_{aaaz} e^{\frac{i(2\eta_a+k_a)d}{2}} \text{sync} \left(\frac{(2\eta_a - k_a)d}{2} \right) \sin^3 \vartheta + \right|^2, \tag{1.112}
\end{aligned}$$

$$\begin{aligned}
S_{vh} \propto & \left| \mathcal{E}_{x,\bar{w}}^2 \right|^2 \left| \frac{\eta_a}{k_b} \Gamma_{baaz} e^{\frac{i(2\eta_a+k_b)d}{2}} \text{sync} \left(\frac{(2\eta_a - k_b)d}{2} \right) \cos^3 \vartheta + \right. \\
& + \left[\frac{\eta_b \Gamma_{babz} + \eta_a \Gamma_{bbaz}}{k_b} e^{\frac{i(\eta_a+\eta_b+k_b)d}{2}} \text{sync} \left(\frac{(\eta_a + \eta_b - k_b)d}{2} \right) + \right. \\
& \left. \left. - \frac{\eta_a}{k_a} \Gamma_{aaaz} e^{\frac{i(2\eta_a+k_a)d}{2}} \text{sync} \left(\frac{(2\eta_a - k_a)d}{2} \right) \right] \sin \vartheta \cos^2 \vartheta + \right. \\
& + \left[- \frac{\eta_b \Gamma_{aabz} + \eta_a \Gamma_{abaz}}{k_a} e^{\frac{i(\eta_a+\eta_b+k_a)d}{2}} \text{sync} \left(\frac{(\eta_a + \eta_b - k_a)d}{2} \right) + \right. \\
& \left. \left. + \frac{\eta_b}{k_b} \Gamma_{bbbz} e^{\frac{i(2\eta_b+k_b)d}{2}} \text{sync} \left(\frac{(2\eta_b - k_b)d}{2} \right) \right] \sin^2 \vartheta \cos \vartheta + \right. \\
& \left. - \frac{\eta_b}{k_a} \Gamma_{abbz} e^{\frac{i(2\eta_b+k_a)d}{2}} \text{sync} \left(\frac{(2\eta_b - k_a)d}{2} \right) \sin^3 \vartheta \right|^2. \tag{1.113}
\end{aligned}$$

Part I

Application to nanotribology

Chapter 2

Our project and Friction Apparatus

Understanding the atomic processes at the interface between two materials when they are brought together, separated or moved with respect to one another is central to nanotribology. The growing diffusion of apparatus, such as the AFM and the SFA, has allowed systematic investigations of interfacial problems with high spatial resolution and good control of the systems [11] [12].

The SFA was developed in 1960s and is employed to study both static and dynamic properties of molecular films sandwiched between two mica surfaces, facing each other in a crossed cylinder geometry. The mica is a silicate that can be cleaved to form step-free atomically-flat surfaces extending over several squared centimeters. The crossed cylinder geometry, combined with the molecular smoothness of the mica, ensures a single contact “point”, when the surfaces

are approached towards each other, with an actual contact area of macroscopic extension.

Recently, the influence of thin liquid films on friction between solid surfaces has been extensively studied with the Surface Force Apparatus including in particular the important “boundary lubricant limit”, where a single molecular monolayer adsorbed at the surface determines the lubricant properties [13]. However, the friction force measurements give no direct information regarding the molecular orientation, alignment, or conformation of the film interposed between the mica surfaces. To do it, additional experimental techniques have to be used to complete the information gained from the SFA. Experimentally, the study of the interfaces is often difficult because of a lack of techniques that have sufficient sensitivity and access to films buried between two different media. For example, the surface sensitive particle scattering techniques, that require an ultra high vacuum environment to operate, usually have a penetration depth of only a few layers, whereas linear spectroscopic techniques are often dominated by bulk contributions and lack the sufficient interface sensitivity. Instead the SHG, being a nonlinear optical process of the second order, has both the required interface sensitivity and the penetration depth. In this context, our idea is to apply the

SHG to nanotribological investigations in the controlled frame of the SFA. The details of the project will be presented in the next section.

2.1 The project: simultaneous measurements of second harmonic radiation and friction force

Our plan is to place the SFA in the path of a laser beam and perform simultaneous measurements of second harmonic radiation and friction force. Such combination enables us to probe the orientation and alignment of lubricant molecules, that are subjected to normal and lateral forces, and study the influence that these properties have on tribological phenomena. For example, measuring the SH signal at fixed polarization as a function of the input polarization, we may obtain information on the in-plane orientation (with respect to the underlying surface) and the tilt angle of the molecules of lubricant and how these change during the sliding. The final goal is to link the structure of the confined molecules with the shear tribological properties of the corresponding films.

At the present, the project is still underway and we have not reached the stage of performing SHG measurements on lubricant films under shear, but some important intermediate steps have been completed. These steps are the subject of the first part of this thesis work and will be presented in the following. In particular,

the first step has been the mounting and interfacing of the FA, and the second one the measurement of the harmonic signal generated from the mica, which represents the background signal for our planned measurements of friction. In the remaining of this chapter, we will present the first step. In chapter 3 and 4 we will show the second harmonic experimental setup and the results of our SHG measurements on mica substrate.

2.2 Design of Friction Apparatus

During the last decade the Surface Force Apparatus has been modified to study the dynamic properties of thin films of lubricant. Retaining its capability to measure static forces, the SFA was upgraded with a lateral sliding mechanism which allowed the two surface to be sheared past each other. Successive improvements permitted sensitive measurements of the shear forces as one surface is moved laterally with respect the other. In particular, we use the Surface Force Apparatus modified for friction measurements, called Friction Apparatus (FA). It was purchased from The Australian National University, in a customized design, developed according to our specifications. In this section, we describe the principles of operation of the FA and the procedure we followed to interface it with the computer. Our Friction Apparatus is capable of measuring friction forces up to

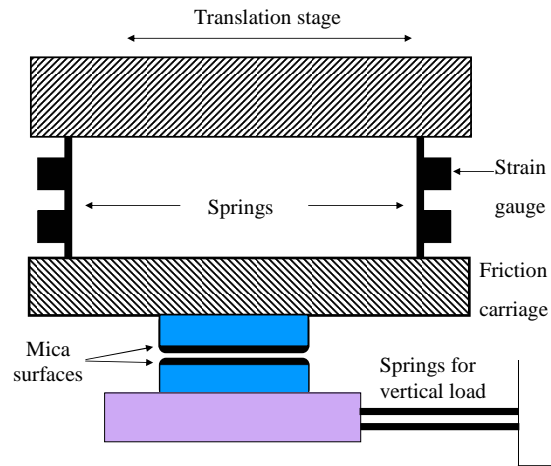


Figure 2.2: Schematic diagram of working principle of the FA.

after they come in contact. The upper surface is attached to the friction carriage. When the two surfaces are in contact, any shear force that results from friction between them gives rise to a bending of the double cantilever springs which connect the translation stage to the friction carriage. Four strain gauges are glued to the springs and connected in the configuration of a Wheatstone bridge. When the friction springs are bent, they give rise to an out of balance electrical signal from the bridge which is proportional to the friction force and which is measured. The horizontal motion of the translation stage is limited to a maximum of around 3 mm by two limits switches, a safety devices used to interrupt the translation of the stage to prevent it from driving the micrometer beyond its limits and thus

damaging the FA. The horizontal position of the translation stage as it moves across the lower surface is obtained from an electrical transducer in the form of a 10 turn potentiometer giving a $\pm 10V$ output powered by a $\pm 15V$ D.C. power supply. The voltage from the slider of the potentiometer is directly proportional to the horizontal displacement of the translation stage. The data are recorded as frictional force versus position of the translation stage.

2.3 Electronic setup of the FA

To operate the Friction Apparatus, we need to move the upper surface at precisely speed and measure the output voltage from the Wheatstone's bridge. The movement of the upper surface was achieved by a means of a precise stepper motor. Regarding the measure of the friction force, we need a device for amplifying and measuring the very low signal generated from the Wheatstone's bridge, that is a suitable signal conditioning. In the next sections, we will explain the features and the working principle of the stepper motor and of the signal conditioning employed in the FA.

2.3.1 Stepper motor and motion control system

In the present section we describe the procedure followed to control the motion of the upper mica surface. To this purpose, we used a stepper motor. Stepper motor incorporates a permanent magnet rotor, coil windings and magnetically conductive stators. An important characteristic of this motor is that it can maintain the holding torque indefinitely when the rotor is stopped. When no power is applied to the windings, a small magnetic force is developed between the permanent magnet and the stator. This magnetic force is called residual torque. The residual torque can be noticed by turning a stepper motor by hand and it is generally about one-tenth of the holding torque.

The stepper motor we use is Radiospares, model 440-262. It is a unipolar stepper motor. It consists of two windings on a pole connected in such a way that when one winding is energized the magnetic north pole is created, while when the other winding is energized the south pole is created. By pulsing the stator coils in a desired sequence, we control the speed and the direction of the motor. The speed of the motor is reduced by a mechanical gearbox (Radiospares model 336-416) and a flexible belt drive. In order to control the stepper motor, we use a driver and a controller (stepper motor motion control system). The Fig. 2.3 shows the

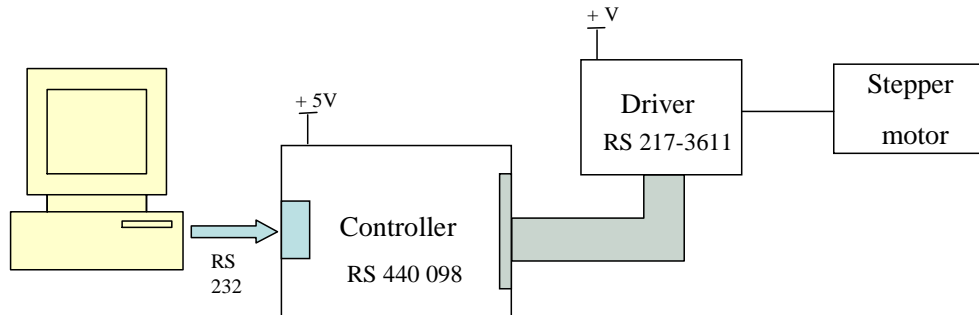


Figure 2.3: Schematic representation of the stepper motor motion control system.

different components of our motion control system. The controller (Radiospares 440-098) acts as the brain of the motion control system and calculates trajectories for each commanded move. We programmed the Radiospares 440-098 controller via an RS-232 serial link to a personal computer. The driver (Radiospares 217-3611) is the part of the system that receives commands from the controller in form of analog voltage signals with low current and converts them into signals with high current to drive the motor. The Radiospares 217-3611 driver uses bifilar windings and four Darlington transistors to control the direction of the rotation and the stepping rate of the motor.

2.3.2 Strain gauge and signal conditioning

In the present section we describe the procedure followed to measure the friction force. First, however, we recall briefly the definition of strain and the working

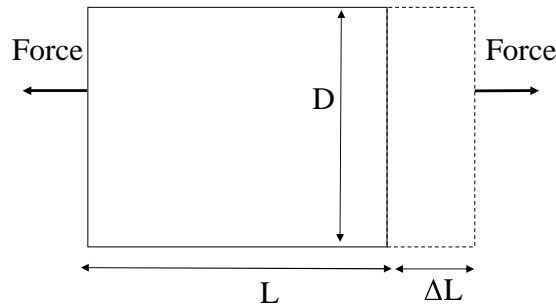


Figure 2.4: Schematic representation of the strain.

principle of the strain gauge.

The strain is the amount of deformation of a body due to an applied force. More specifically, the strain ε is defined as the fractional change in length (see Fig. 2.4):

$$\varepsilon = \frac{\Delta L}{L}. \quad (2.1)$$

The most common way of measuring the strain is by a strain gauge. The strain gauge is a device whose electrical resistance varies in proportion to the amount of strain in the device. Usually, the strain gauge consists of a very fine wire or, more commonly, metallic foil arranged in a grid pattern. We have a strain gauge with the grid bonded to a thin backing, which is attached directly to the double cantilever springs (see Fig. 2.2). Therefore, the strain experienced by the cantilever is transferred directly to the strain gauge, which responds with a

linear change in the electrical resistance. A fundamental parameter of the strain gauge is the sensitivity to the strain, expressed quantitatively as the gauge factor GF. The gauge factor is defined as the ratio of a fractional change in electrical resistance to the a fractional change in length (strain):

$$GF = \frac{\Delta R/R}{\Delta L/L} = \frac{\Delta R/R}{\varepsilon} \quad (2.2)$$

The gauge factor for metallic strain gauges is typically around 2.

To measure the strain, an accurate measurement of very small changes in resistance is required. In order to do it, strain gauges are almost always used in a Wheatstone's bridge configuration. The Wheatstone's bridge, illustrated in Fig. 2.5, consists of four resistive arms with an excitation voltage, V_{ex} . The output voltage of the bridge, V_{out} , is equal to:

$$V_{out} = V_{ex} \left(\frac{R_3}{R_3 + R_4} - \frac{R_2}{R_1 + R_2} \right). \quad (2.3)$$

From this equation, it is evident that when $R_1/R_2 = R_4/R_3$ the voltage output V_{out} is zero. Any change in resistance in any arm of the bridge will result in a nonzero output voltage. Therefore, if we replace R_4 with an active strain gauge (quarter-bridge configuration), any change in the strain gauge resistance will unbalance the bridge and produce a nonzero output voltage. By indicating

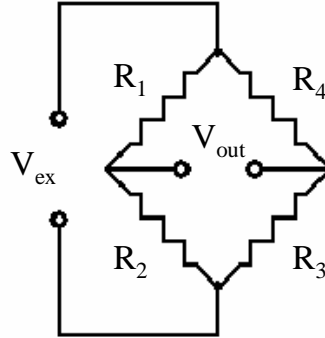


Figure 2.5: Wheatstone bridge.

with R_G the nominal resistance of the strain gauge, the strain-induced change in resistance, ΔR , can be expressed as $\Delta R = R_G GF \varepsilon$. Assuming $R_1 = R_2$ and $R_3 = R_G$, the equation (2.5) can be rewritten expressing V_{out}/V_{ex} as a function of the strain:

$$\frac{V_{out}}{V_{ex}} = -\frac{GF\varepsilon}{4} \left(\frac{1}{1 + GF\varepsilon/2} \right). \quad (2.4)$$

Note that the presence of the term $1/(1 + GF\varepsilon/2)$ indicates the nonlinearity of the bridge output respect to the strain.

Ideally, the resistance of the strain gauge should change only in response to the applied strain. However, strain gauge material responds to changes in temperature. To minimize the temperature effect, the number of strain gauges inside the bridge has to be increased. In fact, any change in temperature will affect the gauges in the same way. Then, the ratio of their resistance does not change

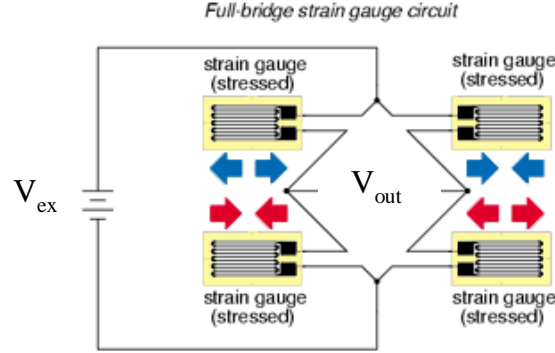


Figure 2.6: Full bridge configuration.

and the effects of the temperature change are minimized. We used a circuit with the four arms of the bridge active strain gauges in a so called full-bridge configuration. The full-bridge circuit is shown in Fig. 2.6. The output voltage in this configuration is given by:

$$\frac{V_{out}}{V_{ex}} = -GF\varepsilon. \quad (2.5)$$

In the (2.5), we assumed an initially balanced bridge that generates zero output when no strain is applied. The full-bridge configuration is the most convenient to use. This is true not only because it minimizes the temperature effects, but also because the output voltage is directly proportional to the strain, with no nonlinearity introduced by the electric circuit.

The output of the strain gauge we use is less than 10mV/V (10 mV of output per volt of excitation). Therefore, we need to amplify it. Moreover, the strain

gauge is located in electrically noisy environments, so we may have a non zero output signal even if no friction force is present between the two mica surfaces. To amplify the low signal and reduce the noise effects we use a signal conditioning device, NI SCC-SG Series, purchased from National Instruments. It consists of a shielded chassis that houses a combination of signal conditioning input and output modules. Each module has two strain gauge input channels, offset nulling circuit for each channel, and a 2.5 V excitation circuit. In particular, we chose the SCC-SG04 model as it is specifically designed to work with the the full-bridge configuration. The main features of our signal conditioning are: excitation, amplification, filtering offset and shunt calibration. In the following we will briefly describe them:

- **Excitation:** the strain gauge signal conditioning provides a constant voltage source to power the bridge. Although there is no standard voltage level, excitation voltage levels of around 3 and 10 V are common. In fact, a higher excitation voltage generates a proportionately higher output voltage, but the higher voltage can also cause larger errors because of self-heating. So, we use an intermediate value to power the bridge, that is 5V.
- **Amplification:** as we said, the output of a strain gauge and also of the bridge

is relatively small. In practice, in our case, it was less than 10 mV/V (10 mV of output per volt of excitation voltage). With 5 V excitation, the output signal is 50 mV. The NI SCC-SG system includes amplifiers to increase the signal level and improve the signal-to-noise ratio.

- Filtering: the strain gauges are located in electrically noisy environments. The NI SCC-SG system has lowpass filters to remove high-frequency noise.
- Offset nulling: due to non-idealities, the bridge does not have an output of exactly zero volts when no strain is applied. Slight variations in resistance among the bridge arms and lead resistance generated some nonzero initial offset voltage. The offset nulling is used to compensate this effect. We performed this operation with software compensation, that is we made an initial measurement before a strain input is applied, then we subtracted this offset to compensate subsequent measurements. Such method is simple, fast, and requires no manual adjustments.
- Shunt calibration: to calibrate the bridge we use the shunt calibration method. We simulate the strain by changing the resistance of an arm in the bridge by some known amount. This is accomplished by connecting

a large resistor of known value across one arm of the bridge, creating a known ΔR . The output of the bridge can then be measured and compared to the expected voltage value. We use the results to correct the next voltage measurement. For the shunt calibration, we used the SCC-SG11 module.

To acquire the analog signal that comes out from the Wheatstone bridge, we use an analog-digital converter, namely a PCI (model 6281) High-Accuracy M Series Multifunction DAQ of the National Instruments.

Chapter 3

Mica

Mica has generated much interest as a crystalline substrate for nanotribological studies because it is chemically stable and can be easily cleaved to expose an atomically smooth surface. In this chapter we are going to introduce the type of mica used in our experiment, the muscovite mica. After that, we will calculate the second harmonic signal generated from it by using the model presented in the section 1.2.2.

3.1 General properties of muscovite mica

Micas are one of the most common mineral types on the Earth's surface, being approximately 4.5% of the crust by volume. They are known for cleavage. The cleavage is the tendency of a crystalline material to split along definite planes creating smooth surfaces. In the mica there are a strong intraplanar bonding and a much weaker interplanar forces. The effect of this structure is the easy

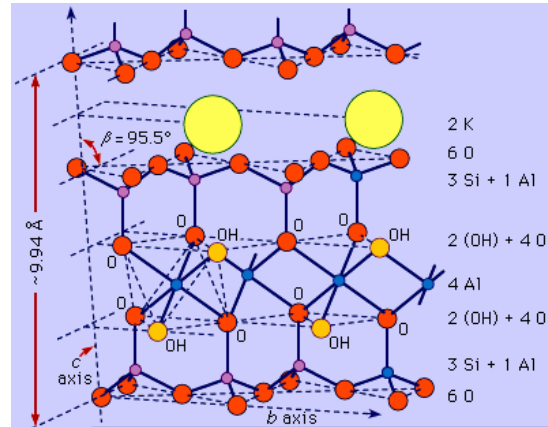


Figure 3.1: Schematic representation of the structure of the muscovite mica.

cleavage parallel to a basal plane¹. The usual mica is the muscovite variety $\text{KA}_3\text{Si}_3\text{O}_{10}(\text{OH})_2$, named not for a location where it was collected, but for its common use in windows in medieval Moscow, instead of glass. It is clear and transparent, unlike most other micas. The muscovite structure consists of two layers of mainly silicon oxide tetrahedra and an octahedral layer between them. Potassium cations reside between the layers and bind them together (see Fig.3.1). Successive layers are shifted laterally in alternating directions separated by 120° , leading to a monoclinic structure with two layers per unit cell.

¹The basal plane is the plane perpendicular to the long, or \hat{c} , axis in all crystals except those of the isometric system.

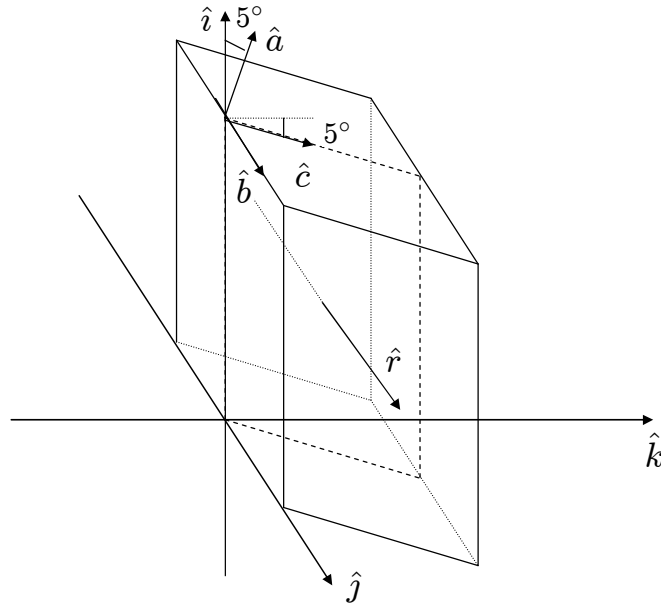


Figure 3.2: Orientation of the principal dielectric axes with respect to the primitive cell of muscovite. The dashed figure is the intersection between the glide plane and the cell itself whereas the \hat{r} -axis is the 2-fold axis. The cleavage plane is parallel to the plane $z = 0$.

3.2 Optical properties of muscovite mica

Since the muscovite mica crystallizes in the monoclinic system, it is optically biaxial. We chose the 2-fold axis of mica as the axis \hat{j} of the laboratory frame (see Fig.3.2). Muscovite mica has a symmetry plane which is perpendicular to the 2-fold axis. This plane is called *glide plane*. In crystallography, the glide plane is symmetry operation describing how a reflection respect to a plane followed by a translation leave the crystal unchanged. In our case, because the tensors characterizing the optical response are not dependent on translations much shorter than

a wavelength, we can consider the glide plane as symmetry plane. The intersection point of the glide plane with the 2-fold axis is the symmetry center of the mica. The two principal axes of the muscovite mica \hat{a} and \hat{b} are almost parallel to cleavage planes [14]. In fact, the principal axis dielectric \hat{c} makes an angle of $\simeq 5^\circ$ with the axis \hat{k} . However, we can neglect this angle and assume that the axes \hat{a} and \hat{b} are in the cleavage plane [15].

The symmetry properties of the mica imply relationships between the elements of the first and second order susceptibilities. The existence of the symmetry plane means that the $\tilde{\chi}_{ij}^{(1)}$ remains the same under reflection with respect to the plane xz :

$$\tilde{\chi}_{xy}^{(1)} = \tilde{\chi}_{x(-y)}^{(1)} = -\tilde{\chi}_{xy}^{(1)}. \quad (3.1)$$

So, we can say that the elements of $\tilde{\chi}_{ij}^{(1)}$ with an odd number of indexes y are vanish:

$$\tilde{\chi}_{xy}^{(1)}(0, \bar{\omega}) = \tilde{\chi}_{yx}^{(1)}(0, \bar{\omega}) = \quad (3.2)$$

$$\tilde{\chi}_{yz}^{(1)}(0, \bar{\omega}) = \tilde{\chi}_{zy}^{(1)}(0, \bar{\omega}) = 0.$$

Obviously we have the same relations for the first order susceptibility calculated at frequency $2\bar{\omega}$. For the second order susceptibility, the existence of the plane

symmetry implies that all the elements of $\Gamma_{\gamma\alpha\beta z}$ containing an odd number of b vanish.

3.3 Nonlocal Second Harmonic Radiation generated from muscovite mica

Let us assume that in the region $0 < z < d$ of the laboratory there is the muscovite mica. We put the mica in our experimental setup with the cleavage plane coincident with the plane $z = 0$ plane. Since the axis \hat{c} of the mica is perpendicular to cleavage plane, it coincides with the axis \hat{k} of the laboratory frame. In this configuration we can use the (1.110)-(1.113). To this purpose, we define the refraction indices at frequency ω and $2\bar{\omega}$ along the direction γ as follows:

$$\begin{aligned}
 n_{\gamma, \bar{\omega}} &= \sqrt{1 + \tilde{\chi}_{\gamma\gamma}^{(1)}(0, \bar{\omega})}, \\
 n_{\gamma, 2\bar{\omega}} &= \sqrt{1 + \tilde{\chi}_{\gamma\gamma}^{(1)}(0, 2\bar{\omega})},
 \end{aligned}
 \tag{3.3}$$

with $\gamma = a, b$. Beside, we define the the dispersion with respect to the axis a , and the birefringence at frequency $\beta_{2\bar{\omega}}$ and $\beta_{\bar{\omega}}$ as follows:

$$\delta_a = n_{a,2\bar{\omega}} - n_{a,\bar{\omega}}$$

$$\beta_{2\bar{\omega}} = n_{b,2\bar{\omega}} - n_{a,2\bar{\omega}}$$

$$\beta_{\bar{\omega}} = n_{b,\bar{\omega}} - n_{a,\bar{\omega}}.$$

From the literature, we known that the birefringence of muscovite mica at frequency $\bar{\omega}$ is $5 \cdot 10^{-3}$ [8] and the dispersion is $2 \cdot 10^{-2}$ [9]. We assume that the birefringence at frequency $2\bar{\omega}$ is of the same order of magnitude of that at frequency $\bar{\omega}$. Then, by using these value, we obtain an estimate of the ratio between the wave vectors corresponding to the axes \hat{a} and \hat{b} of the muscovite mica:

$$\frac{\eta_a}{k_b} = \frac{1}{2} \frac{n_{a,\bar{\omega}}}{n_{b,2\bar{\omega}}} \simeq \frac{1}{2}. \tag{3.4}$$

Inserting the (3.4) in the equations (1.110)-(1.113), we obtain the second harmonic signals, for the four different input-output polarization combinations, gen-

erated from the muscovite mica:

$$\begin{aligned}
 S_{vv} \propto & \left| \mathcal{E}_{x,\bar{\omega}}^2 \right|^2 \left[\Gamma_{aaa} e^{\frac{i\bar{\omega}d}{c}\delta_a} \text{sync} \left((-\delta_a) \frac{\bar{\omega}d}{c} \right) \cos^3 \vartheta + \right. \\
 & + \Gamma_{bbb} e^{\frac{i2\pi d}{\lambda}(\delta_a + \beta_{\bar{\omega}} + \beta_{2\bar{\omega}})} \text{sync} \left((-\delta_a + \beta_{\bar{\omega}} - \beta_{2\bar{\omega}}) \frac{\bar{\omega}d}{c} \right) \sin^3 \vartheta + \\
 & + \left[(\Gamma_{bbaz} + \Gamma_{bab}) e^{\frac{i2\pi d}{\lambda}(\delta_a + \frac{1}{2}\beta_{\bar{\omega}} + \beta_{2\bar{\omega}})} \text{sync} \left((-\delta_a + \frac{1}{2}\beta_{\bar{\omega}} - \beta_{2\bar{\omega}}) \frac{\bar{\omega}d}{c} \right) + \right. \\
 & + \left. \Gamma_{abbz} e^{\frac{i2\pi d}{\lambda}(\delta_a + \beta_{\bar{\omega}})} \text{sync} \left((-\delta_a + \beta_{\bar{\omega}}) \frac{\bar{\omega}d}{c} \right) \right] \sin^2 \vartheta \cos \vartheta + \\
 & + \left[(\Gamma_{abaz} + \Gamma_{aabz}) e^{\frac{i\bar{\omega}d}{c}(\delta_a + \frac{1}{2}\beta_{\bar{\omega}})} \text{sync} \left((-\delta_a + \frac{1}{2}\beta_{\bar{\omega}}) \frac{\bar{\omega}d}{c} \right) + \right. \\
 & + \left. \Gamma_{baaz} e^{\frac{i\bar{\omega}d}{c}(\delta_a + \beta_{2\bar{\omega}})} \text{sync} \left((-\delta_a - \beta_{\bar{\omega}}) \frac{\bar{\omega}d}{c} \right) \right] \sin \vartheta \cos^2 \vartheta \Big|^2, \quad (3.5)
 \end{aligned}$$

$$\begin{aligned}
 S_{hv} \propto & \left| \mathcal{E}_{y,\bar{\omega}}^2 \right|^2 \left[\Gamma_{abbz} e^{\frac{i\bar{\omega}d}{c}(\beta_{\bar{\omega}} + \delta_a)} \text{sync} \left((-\delta_a + \beta_{\bar{\omega}}) \frac{\bar{\omega}d}{c} \right) \cos^3 \vartheta + \right. \\
 & + \Gamma_{baaz} e^{\frac{i\bar{\omega}d}{c}(\delta_a + \beta_{\bar{\omega}})} \text{sync} \left((-\delta_a - \beta_{\bar{\omega}}) \frac{\bar{\omega}d}{c} \right) \sin^3 \vartheta + \\
 & + \left[-(\Gamma_{bbaz} + \Gamma_{bab}) e^{\frac{i\bar{\omega}d}{c}(\delta_a + \frac{1}{2}\beta_{\bar{\omega}} + \beta_{2\bar{\omega}})} \text{sync} \left((-\delta_a + \frac{1}{2}\beta_{\bar{\omega}} - \beta_{2\bar{\omega}}) \frac{\bar{\omega}d}{c} \right) + \right. \\
 & + \left. \Gamma_{aaa} e^{\frac{i\bar{\omega}d}{c}\delta_a} \text{sync} \left((-\delta_a) \frac{\bar{\omega}d}{c} \right) \right] \sin^2 \vartheta \cos \vartheta + \\
 & + \left[-(\Gamma_{abaz} + \Gamma_{aabz}) e^{\frac{i\bar{\omega}d}{c}(\delta_a + \frac{1}{2}\beta_{\bar{\omega}})} \text{sync} \left((-\delta_a + \frac{1}{2}\beta_{\bar{\omega}}) \frac{\bar{\omega}d}{c} \right) + \right. \\
 & + \left. \Gamma_{bbbz} e^{\frac{i\bar{\omega}d}{c}(-\delta_a - \beta_{2\bar{\omega}} + \beta_{\bar{\omega}})} \text{sync} \left((-\delta_a - \beta_{2\bar{\omega}} + \beta_{\bar{\omega}}) \frac{\bar{\omega}d}{c} \right) \right] \sin \vartheta \cos^2 \vartheta \Big|^2, \quad (3.6)
 \end{aligned}$$

$$\begin{aligned}
 S_{hh} \propto & \left| \mathcal{E}_{y,\bar{w}}^2 \right|^2 \left[\Gamma_{bbbz} e^{\frac{i\bar{w}d}{c}(\beta_{\bar{w}}+\beta_{2\bar{w}}+\delta_a)} \text{sync} \left((-\delta_a + \beta_{\bar{w}} - \beta_{2\bar{w}}) \frac{\bar{w}d}{c} \right) \cos^3 \vartheta + \right. \\
 & - \Gamma_{aaaaz} e^{\frac{i\bar{w}d}{c}\delta_a} \text{sync} \left((-\delta_a) \frac{\bar{w}d}{c} \right) \sin^3 \vartheta + \\
 & + \left[\Gamma_{baaz} e^{\frac{i\bar{w}d}{c}(\delta_a+\beta_{2\bar{w}})} \text{sync} \left((-\delta_a - \beta_{2\bar{w}}) \frac{\bar{w}d}{c} \right) - \right. \\
 & + \left. (\Gamma_{abaz} + \Gamma_{aabz}) e^{\frac{i\bar{w}d}{c}(\delta_a+\frac{1}{2}\beta_{\bar{w}})} \text{sync} \left((-\delta_a + \frac{1}{2}\beta_{\bar{w}}) \frac{\bar{w}d}{c} \right) \right] \sin^2 \vartheta \cos \vartheta + \\
 & + \left[- (\Gamma_{bbaz} + \Gamma_{babz}) e^{\frac{i\bar{w}d}{c}(\delta_a+\frac{1}{2}\beta_{\bar{w}}+\beta_{\bar{w}})} \text{sync} \left((-\delta_a + \frac{1}{2}\beta_{\bar{w}} - \beta_{2\bar{w}}) \frac{\bar{w}d}{c} \right) + \right. \\
 & \left. \left. - \Gamma_{abbz} e^{\frac{i\bar{w}d}{c}(-\delta_a+\beta_{\bar{w}})} \text{sync} \left((-\delta_a + \beta_{\bar{w}}) \frac{\bar{w}d}{c} \right) \right] \sin \vartheta \cos^2 \vartheta \right|^2, \tag{3.7}
 \end{aligned}$$

$$\begin{aligned}
 S_{vh} \propto & \left| \mathcal{E}_{x,\bar{w}}^2 \right|^2 \left[\Gamma_{baaz} e^{\frac{i\bar{w}d}{c}(\beta_{2\bar{w}}+\delta_a)} \text{sync} \left((-\delta_a - \beta_{2\bar{w}}) \frac{\bar{w}d}{c} \right) \cos^3 \vartheta + \right. \\
 & - \Gamma_{abbz} e^{\frac{i\bar{w}d}{c}(\delta_a+\beta_{\bar{w}})} \text{sync} \left((-\delta_a + \beta_{\bar{w}}) \frac{\bar{w}d}{c} \right) \sin^3 \vartheta + \\
 & + \left[\Gamma_{bbbz} e^{\frac{i\bar{w}d}{c}(\delta_a+\beta_{2\bar{w}}+\beta_{\bar{w}})} \text{sync} \left((-\delta_a + \beta_{\bar{w}} - \beta_{2\bar{w}}) \frac{\bar{w}d}{c} \right) - \right. \\
 & + \left. (\Gamma_{abaz} + \Gamma_{aabz}) e^{\frac{i\bar{w}d}{c}(\delta_a+\frac{1}{2}\beta_{\bar{w}})} \text{sync} \left((-\delta_a + \frac{1}{2}\beta_{\bar{w}}) \frac{\bar{w}d}{c} \right) \right] \sin^2 \vartheta \cos \vartheta + \\
 & + \left[(\Gamma_{bbaz} + \Gamma_{babz}) e^{\frac{i\bar{w}d}{c}(\delta_a+\frac{1}{2}\beta_{\bar{w}}+\beta_{2\bar{w}})} \text{sync} \left((-\delta_a + \frac{1}{2}\beta_{\bar{w}} - \beta_{2\bar{w}}) \frac{\bar{w}d}{c} \right) + \right. \\
 & \left. \left. - \Gamma_{aaaaz} e^{\frac{i\bar{w}d}{c}(-\delta_a)} \text{sync} \left((-\delta_a) \frac{\bar{w}d}{c} \right) \right] \sin \vartheta \cos^2 \vartheta \right|^2. \tag{3.8}
 \end{aligned}$$

Chapter 4

Experimental setup and SHG results for muscovite mica

The SHG measurements from the muscovite mica constituted the second step of our project. Being mica a centrosymmetric material, we expected that it generates only second harmonic radiation at the surface, where the inversion symmetry is broken. However, our SHG measurements showed an intense second harmonic radiation. We attributed this signal to the nonlocal response of the mica and then explained the results by using the theoretical model developed in the section 3.3. In the first section of this chapter we describe the experimental setup used for Second Harmonic measurements and in the second section, we discuss the results obtained.

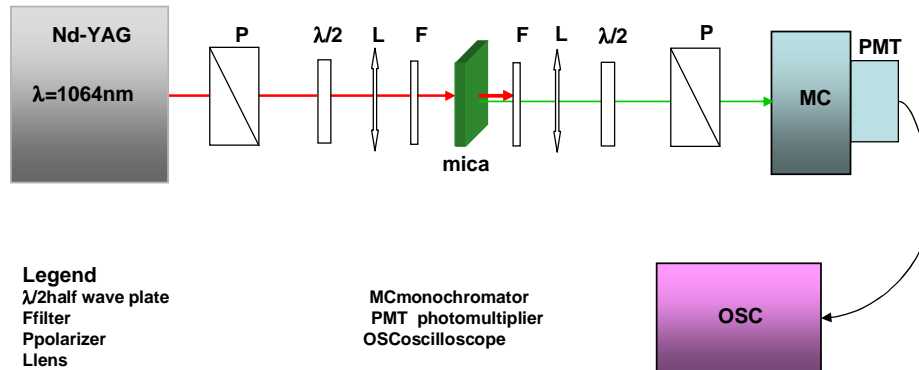


Figure 4.1: Experimental setup for the generation and measurement of the second harmonic signal generated from the mica in the transmission geometry.

4.1 Second Harmonic Experimental setup

The experimental setup for Second Harmonic Generation measurements is shown in Fig. 4.1. A mode-locked Nd-YAG laser (mod. PL2143B Ekspla Ltd) provides pulses at 1064 nm with repetition rate of 10 Hz. During the experiment, the laser polarization was controlled using a cube polarizer and a half-wave plate. The laser beam was focused onto the mica sample by a lens. A long-pass filter, placed before the sample, eliminates any possible second harmonic radiation generated by the previous optical components. The sample is mounted on a rotation stage. The transmitted IR light is blocked by a short-pass filter. We introduced another half-wave plate and cube polarizer to select also the polarization direction of the second harmonic radiation. With a monochromator we have selected accurately

the second harmonic radiation against possible two-photon fluorescence or other background light. A Hamamatsu R928's photomultiplier has been used as a detector. The electrical signal coming from the photomultiplier is displayed and measured from a digital oscilloscope, model TDS3032 of the Tektronix.

4.1.1 Results and discussion

In this section we show the measurements of the second harmonic radiation intensity generated by 5 mica discs of the highest quality grade V-1, purchased from SPI Supplies. The transmitted second harmonic signal was measured as a function of the mica rotation about its surface normal for four different input-output polarization combinations: vv , vh , hh and hv (v here means vertical polarization direction and h horizontal polarization direction). We used samples of different thickness and named them I , II , III , IV and V . The first two are obtained from a mica disc by cleaving with the help of bidistilled water and a needle. The others are three mica discs used as received from the supplier with a nominal thickness ranging from $275 \mu\text{m}$ to $325 \mu\text{m}$. All data have been taken at the same energy of the laser (about 2.5 mJ per pulse) at room temperature.

The experimental data are shown in Figs. (4.2)-(4.6). Since the mica is centrosymmetric, it can generate SH radiation from the bulk only including the

nonlocal contribution to the nonlinear response. Usually, the nonlocal contribution to the second order nonlinear polarization is negligible, but in the case where a phase matching condition is satisfied, it can become higher than the interfacial local contributions. From our experimental data, it appears that the muscovite mica in our experimental geometry at normal incidence angle is close enough to satisfy this condition. Therefore, to explain our experimental data we use the equations derived in section 3.3 for the nonlocal SHG in a centrosymmetric material:

$$\begin{aligned}
S_{vv} \propto & \left| \mathcal{E}_{x,\bar{\omega}}^2 \right|^2 \left[\Gamma_{aaaz} e^{\frac{i\bar{\omega}d}{c}\delta_a} \text{sync} \left(\left(-\delta_a \right) \frac{\bar{\omega}d}{c} \right) \cos^3 \vartheta + \right. \\
& + \Gamma_{bbbz} e^{\frac{i2\pi d}{\lambda}(\delta_a + \beta_{\bar{\omega}} + \beta_{2\bar{\omega}})} \text{sync} \left(\left(-\delta_a + \beta_{\bar{\omega}} - \beta_{2\bar{\omega}} \right) \frac{\bar{\omega}d}{c} \right) \sin^3 \vartheta + \\
& + \left[(\Gamma_{bbaz} + \Gamma_{bab}) e^{\frac{i2\pi d}{\lambda}(\delta_a + \frac{1}{2}\beta_{\bar{\omega}} + \beta_{2\bar{\omega}})} \text{sync} \left(\left(-\delta_a + \frac{1}{2}\beta_{\bar{\omega}} - \beta_{2\bar{\omega}} \right) \frac{\bar{\omega}d}{c} \right) + \right. \\
& + \Gamma_{abbz} e^{\frac{i2\pi d}{\lambda}(\delta_a + \beta_{\bar{\omega}})} \text{sync} \left(\left(-\delta_a + \beta_{\bar{\omega}} \right) \frac{\bar{\omega}d}{c} \right) \left. \right] \sin^2 \vartheta \cos \vartheta + \\
& + \left[(\Gamma_{abaz} + \Gamma_{aabz}) e^{\frac{i\bar{\omega}d}{c}(\delta_a + \frac{1}{2}\beta_{\bar{\omega}})} \text{sync} \left(\left(-\delta_a + \frac{1}{2}\beta_{\bar{\omega}} \right) \frac{\bar{\omega}d}{c} \right) + \right. \\
& + \Gamma_{baaz} e^{\frac{i\bar{\omega}d}{c}(\delta_a + \beta_{2\bar{\omega}})} \text{sync} \left(\left(-\delta_a - \beta_{\bar{\omega}} \right) \frac{\bar{\omega}d}{c} \right) \left. \right] \sin \vartheta \cos^2 \vartheta \Bigg|^2, \tag{4.1}
\end{aligned}$$

$$\begin{aligned}
S_{hv} \propto |\mathcal{E}_{y,\bar{\omega}}^2|^2 & \left[\Gamma_{abbz} e^{\frac{i\bar{\omega}d}{c}(\beta_{\bar{\omega}}+\delta_a)} \text{sync} \left((-\delta_a + \beta_{\bar{\omega}}) \frac{\bar{\omega}d}{c} \right) \cos^3 \vartheta + \right. \\
& + \Gamma_{baaz} e^{\frac{i\bar{\omega}d}{c}(\delta_a+\beta_{\bar{\omega}})} \text{sync} \left((-\delta_a - \beta_{\bar{\omega}}) \frac{\bar{\omega}d}{c} \right) \sin^3 \vartheta + \\
& + \left[-(\Gamma_{bbaz} + \Gamma_{bab}) e^{\frac{i\bar{\omega}d}{c}(\delta_a+\frac{1}{2}\beta_{\bar{\omega}}+\beta_{2\bar{\omega}})} \text{sync} \left((-\delta_a + \frac{1}{2}\beta_{\bar{\omega}} - \beta_{2\bar{\omega}}) \frac{\bar{\omega}d}{c} \right) + \right. \\
& + \left. \Gamma_{aaaz} e^{\frac{i\bar{\omega}d}{c}\delta_a} \text{sync} \left((-\delta_a) \frac{\bar{\omega}d}{c} \right) \right] \sin^2 \vartheta \cos \vartheta + \\
& + \left[-(\Gamma_{abaz} + \Gamma_{aabz}) e^{\frac{i\bar{\omega}d}{c}(\delta_a+\frac{1}{2}\beta_{\bar{\omega}})} \text{sync} \left((-\delta_a + \frac{1}{2}\beta_{\bar{\omega}}) \frac{\bar{\omega}d}{c} \right) + \right. \\
& + \left. \left. \Gamma_{bbbz} e^{\frac{i\bar{\omega}d}{c}(-\delta_a-\beta_{2\bar{\omega}}+\beta_{\bar{\omega}})} \text{sync} \left((-\delta_a - \beta_{2\bar{\omega}} + \beta_{\bar{\omega}}) \frac{\bar{\omega}d}{c} \right) \right] \sin \vartheta \cos^2 \vartheta \right]^2, \quad (4.2)
\end{aligned}$$

$$\begin{aligned}
S_{hh} \propto |\mathcal{E}_{y,\bar{\omega}}^2|^2 & \left[\Gamma_{bbbz} e^{\frac{i\bar{\omega}d}{c}(\beta_{\bar{\omega}}+\beta_{2\bar{\omega}}+\delta_a)} \text{sync} \left((-\delta_a + \beta_{\bar{\omega}} - \beta_{2\bar{\omega}}) \frac{\bar{\omega}d}{c} \right) \cos^3 \vartheta + \right. \\
& - \Gamma_{aaaz} e^{\frac{i\bar{\omega}d}{c}\delta_a} \text{sync} \left((-\delta_a) \frac{\bar{\omega}d}{c} \right) \sin^3 \vartheta + \\
& + \left[\Gamma_{baaz} e^{\frac{i\bar{\omega}d}{c}(\delta_a+\beta_{2\bar{\omega}})} \text{sync} \left((-\delta_a - \beta_{2\bar{\omega}}) \frac{\bar{\omega}d}{c} \right) - \right. \\
& + \left. (\Gamma_{abaz} + \Gamma_{aabz}) e^{\frac{i\bar{\omega}d}{c}(\delta_a+\frac{1}{2}\beta_{\bar{\omega}})} \text{sync} \left((-\delta_a + \frac{1}{2}\beta_{\bar{\omega}}) \frac{\bar{\omega}d}{c} \right) \right] \sin^2 \vartheta \cos \vartheta + \\
& + \left[-(\Gamma_{bbaz} + \Gamma_{babz}) e^{\frac{i\bar{\omega}d}{c}(\delta_a+\frac{1}{2}\beta_{\bar{\omega}}+\beta_{\bar{\omega}})} \text{sync} \left((-\delta_a + \frac{1}{2}\beta_{\bar{\omega}} - \beta_{2\bar{\omega}}) \frac{\bar{\omega}d}{c} \right) + \right. \\
& - \left. \left. \Gamma_{abbz} e^{\frac{i\bar{\omega}d}{c}(-\delta_a+\beta_{\bar{\omega}})} \text{sync} \left((-\delta_a + \beta_{\bar{\omega}}) \frac{\bar{\omega}d}{c} \right) \right] \sin \vartheta \cos^2 \vartheta \right]^2, \quad (4.3)
\end{aligned}$$

$$\begin{aligned}
S_{vh} \propto & \left| \mathcal{E}_{x,\bar{\omega}}^2 \right|^2 \left[\Gamma_{baaz} e^{\frac{i\bar{\omega}d}{c}(\beta_{2\bar{\omega}}+\delta_a)} \text{sync} \left((-\delta_a - \beta_{2\bar{\omega}}) \frac{\bar{\omega}d}{c} \right) \cos^3 \vartheta + \right. \\
& - \Gamma_{abbz} e^{\frac{i\bar{\omega}d}{c}(\delta_a+\beta_{\bar{\omega}})} \text{sync} \left((-\delta_a + \beta_{\bar{\omega}}) \frac{\bar{\omega}d}{c} \right) \sin^3 \vartheta + \\
& + \left[\Gamma_{bbbz} e^{\frac{i\bar{\omega}d}{c}(\delta_a+\beta_{2\bar{\omega}}+\beta_{\bar{\omega}})} \text{sync} \left((-\delta_a + \beta_{\bar{\omega}} - \beta_{2\bar{\omega}}) \frac{\bar{\omega}d}{c} \right) - \right. \\
& + \left. \left. \left(\Gamma_{abaz} + \Gamma_{aabz} \right) e^{\frac{i\bar{\omega}d}{c}(\delta_a+\frac{1}{2}\beta_{\bar{\omega}})} \text{sync} \left((-\delta_a + \frac{1}{2}\beta_{\bar{\omega}}) \frac{\bar{\omega}d}{c} \right) \right] \sin^2 \vartheta \cos \vartheta + \right. \\
& + \left[\left(\Gamma_{bbaaz} + \Gamma_{babz} \right) e^{\frac{i\bar{\omega}d}{c}(\delta_a+\frac{1}{2}\beta_{\bar{\omega}}+\beta_{2\bar{\omega}})} \text{sync} \left((-\delta_a + \frac{1}{2}\beta_{\bar{\omega}} - \beta_{2\bar{\omega}}) \frac{\bar{\omega}d}{c} \right) + \right. \\
& \left. \left. - \Gamma_{aaaz} e^{\frac{i\bar{\omega}d}{c}(-\delta_a)} \text{sync} \left((-\delta_a) \frac{\bar{\omega}d}{c} \right) \right] \sin \vartheta \cos^2 \vartheta \right]^2. \tag{4.4}
\end{aligned}$$

First, we rewrite these expressions in a different version. In fact, by using as fit procedure the least squares method and by choosing as fit parameters δ_a , $\beta_{\bar{\omega}}$ and $\beta_{2\bar{\omega}}$, the chi square depends on trigonometric functions of the parameters. Because such function are periodic, the chi square has in the parameters space an infinite number of equivalent minima. This fact make the standard numerical best fit procedure very ineffective. Therefore, we chosen to redefine the fit by a suitable change of variables. To this purpose, we express the incident plane wave at frequency $\bar{\omega}$, of amplitude \mathcal{E}_i and polarization lies along the axes x or y as follows:

$$E_{j,\bar{\omega}}^{(i)}(z) = \sum_{\gamma=a,b} R_{j\gamma}^{-1} R_{\gamma,i} \mathcal{E}_i e^{i\eta_{\gamma}z}, \tag{4.5}$$

where $i = x$ or y and $\eta_\gamma^2 = \frac{\bar{\omega}^2}{c^2} \varepsilon_\gamma(\bar{\omega})$. Thus, the equation (1.105) that gives the second harmonic field generated from the mica becomes:

$$E_{j,2\bar{\omega}}^{(i)}(d) = 2id\mu_0\bar{\omega}^2\mathcal{E}_i^2 \sum_{\gamma=a,b} R_{j\gamma}^{-1} \frac{1}{k_\gamma} \times \\ \times [T_{aa\gamma}R_{ai}^2 + (T_{ab\gamma} + T_{ba\gamma})R_{ai}R_{bi} + T_{bb\gamma}R_{bi}^2], \quad (4.6)$$

where we put

$$T_{\alpha\beta\gamma} = i\eta_\beta\Gamma_{\gamma\alpha\beta z} e^{\frac{i(\eta_\alpha + \eta_\beta + k_\gamma)d}{2}} \times \text{sync} \left[\frac{i(\eta_\alpha + \eta_\beta - k_\gamma)d}{2} \right] \quad (4.7)$$

and

$$k_\gamma = \frac{4\bar{\omega}^2}{c^2} \varepsilon_\gamma(2\bar{\omega}).$$

With the (4.6), using the same calculation as in section 3.3, we get the second harmonic signals generated from the muscovite mica for the different input-output polarization combinations¹:

$$S_{vv} \propto \cos^2(\vartheta) \left[(\mathcal{A} \cos^2 \vartheta + \mathcal{B})^2 + \mathcal{C} \right] \\ S_{vh} \propto \cos^2(\vartheta + \pi/2) \left[(\mathcal{A} \cos^2(\vartheta + \pi/2) + \mathcal{D})^2 + \mathcal{F} \right] \quad (4.8)$$

¹In order to simplify the notation, we indicate the components polarized along x and y axis with v and h , respectively.

and

$$\begin{aligned}
S_{hh} &\propto \cos^2(\vartheta + \pi/2) \left[(\mathcal{A} \cos^2(\vartheta + \pi/2) + \mathcal{B})^2 + \mathcal{C} \right] \\
S_{hv} &\propto \cos^2(\vartheta) \left[(\mathcal{A} \cos^2 \vartheta + \mathcal{D})^2 + \mathcal{F} \right].
\end{aligned} \tag{4.9}$$

We note that introducing the tensor $T_{\alpha\beta\gamma}$, we have equations less complicated than the (4.1)-(4.4), where the parameters parameters fit are now the coefficients \mathcal{A} , \mathcal{B} , \mathcal{C} , \mathcal{D} , \mathcal{F} . They are related to $\Gamma_{\alpha\beta\gamma}$, the dispersion and the birefringence by the following relations:

$$\begin{aligned}
|\mathcal{B} + i\mathcal{C} + \mathcal{A}|^2 &= \left| \frac{1}{k_a} T_{aaa} \right|^2 = \frac{\eta_a^2}{k_a^2} |\Gamma_{aaa}|^2 \text{sync}^2 \left[\frac{-\bar{\omega} \delta_a}{c} d \right] \\
|i\mathcal{F} - \mathcal{D} - \mathcal{A}|^2 &= \left| \frac{1}{k_a} T_{bba} \right|^2 = \frac{\eta_b^2}{k_a^2} |\Gamma_{abb}|^2 \text{sync}^2 \left[\frac{\bar{\omega}(\beta_{\bar{\omega}} - \delta_a)}{c} d \right] \\
|\mathcal{A} + \mathcal{D} - i\mathcal{F} + \mathcal{B} + i\mathcal{C}|^2 &= \left| \frac{1}{k_B} (T_{abb} + T_{bab}) \right|^2 = \\
&= \frac{|\eta_b \Gamma_{bab} + \eta_a \Gamma_{bba}|^2}{k_b^2} \text{sync}^2 \left[\frac{\bar{\omega}(-\delta_a + \frac{\beta_{\bar{\omega}}}{2})}{c} d \right].
\end{aligned} \tag{4.10}$$

We used the equations (4.8)-(4.9) to fit the experimental data.

Now, we move on explain the results by means of our theoretical model. The sample I ($d \simeq 30 \mu\text{m}$) has the S_{vv} , S_{hv} , S_{vh} and S_{hh} signals with six oscillations of the same amplitude. As expected by symmetry arguments and predicted by the equations (4.8)-(4.9), the S_{vh} and S_{hh} signals are respectively identical to S_{hv} and S_{vv} , except for a 90° angle shift (see Fig.4.2). It is possible to show that

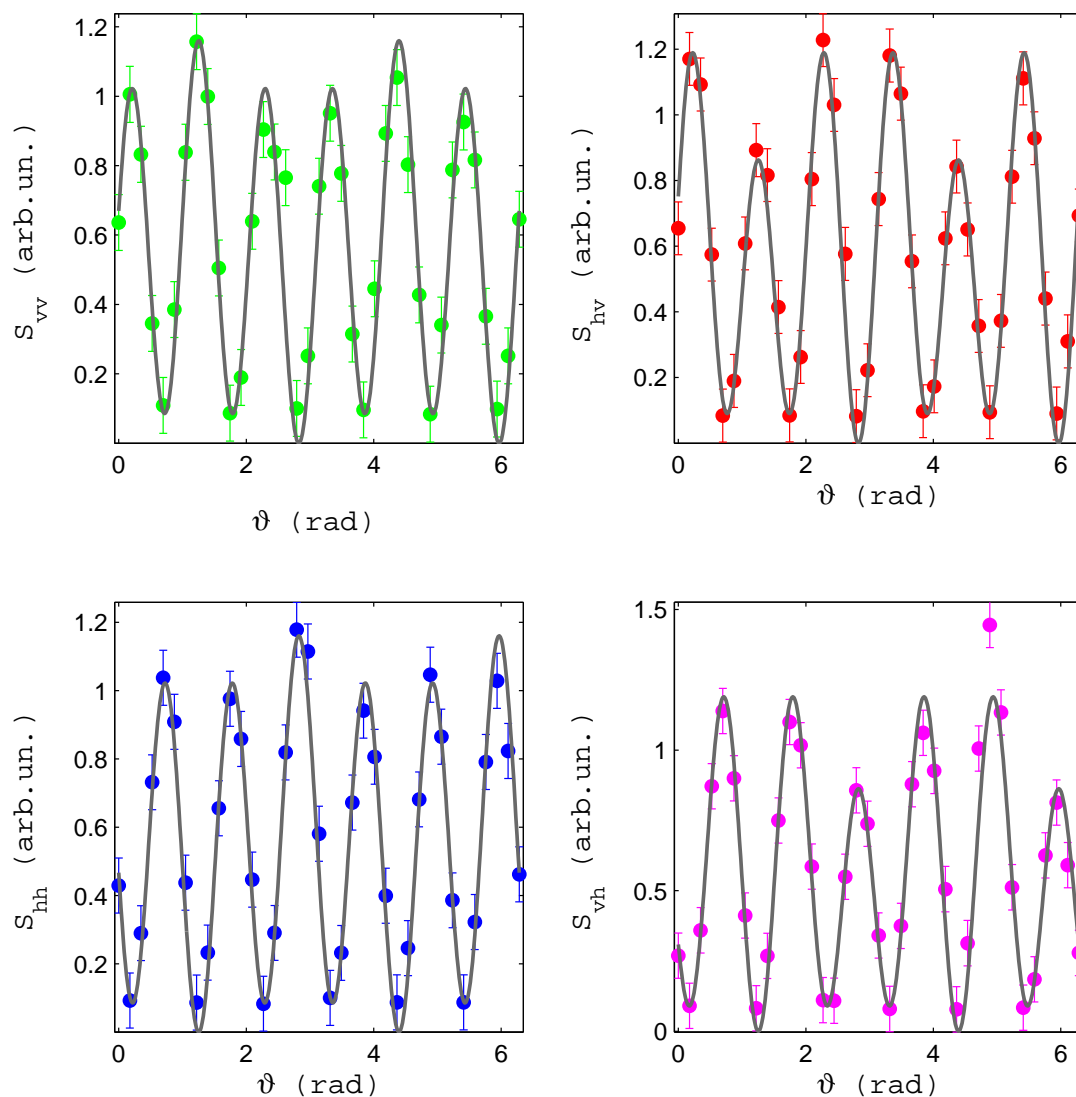


Figure 4.2: Dependence of the second harmonic signals on the mica (sample *I*) rotation angle for 4 different polarization combinations. Circles are data and solid curves are fit from (4.8)-(4.9) equations.

in the limit of zero thickness, all four SH signals must have six peaks. For our samples this limit is verified only for the sample *I*. In fact, for the sample *II*

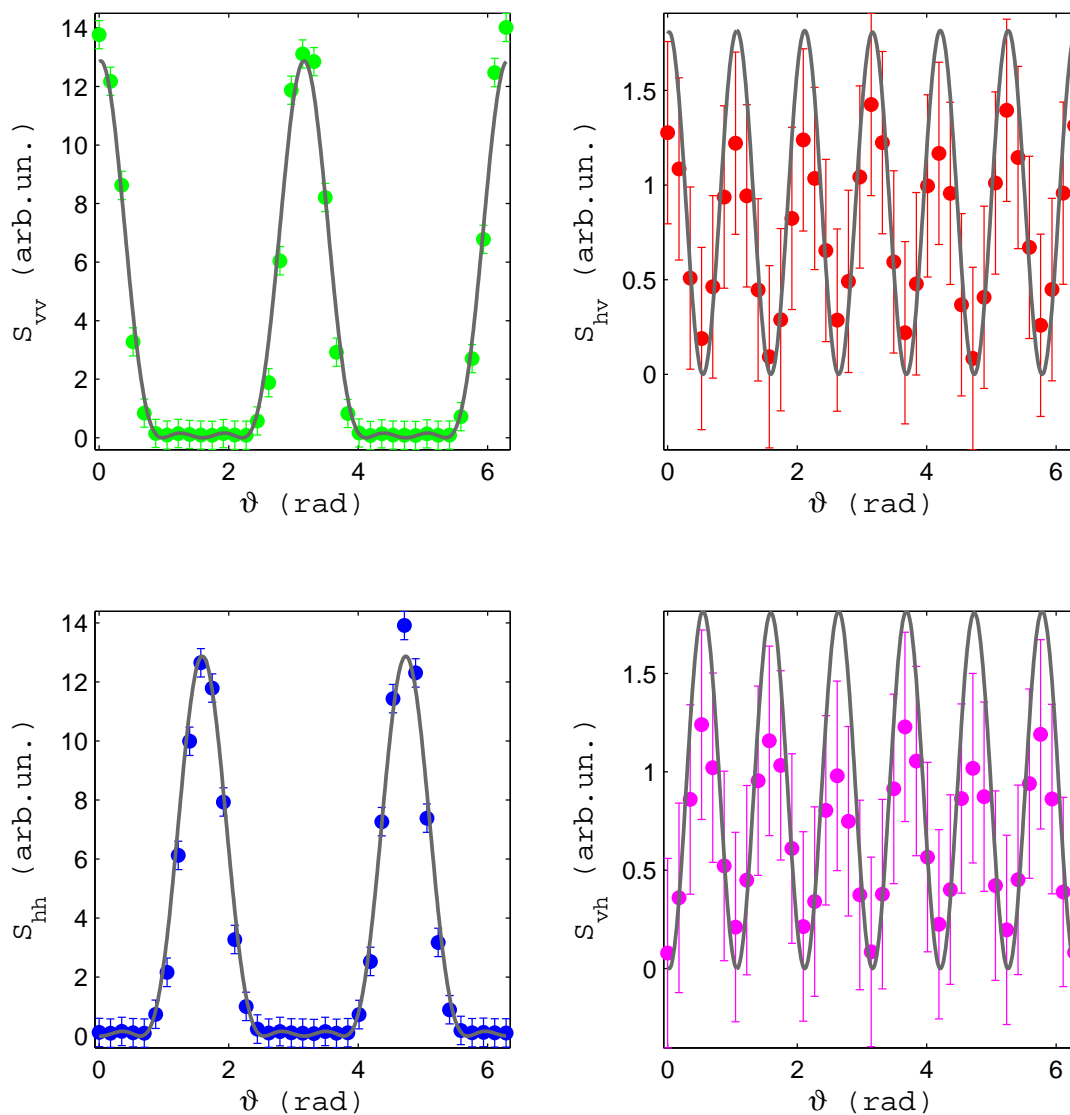


Figure 4.3: Dependence of the second harmonic signals on the mica (sample *II*) rotation angle for 4 different polarization combinations. Circles are data and solid curves are fit from (4.8)-(4.9) equations.

($d \simeq 80 \mu\text{m}$), the vh and hv signals have 6 peaks, whereas the vv and hh signals have only 2 large peaks (see Fig. 4.3). Thus, when the thickness of the mica

increases, a coupling between it and the birefringence appears. This coupling makes the signal dependent on the sample thickness as one can see from the Figs. (4.4)-(4.6). Besides, the amplitude of the signals of the sample *II*, for the polarization combinations *vv* and *hh*, is about 10 times higher than those ones from the others samples; whereas for the sample *V*, the amplitudes for all the polarization combinations are 10 times higher than the others samples. We interpreted these last effects as resulting from varying degrees of phase-matching condition occurring in different samples. This fact indicates that the SHG is generated in the bulk and not from the outer interfaces of the mica. To conclude this first part of the thesis, we can say that the most important features of these measurements are three. First, the SH signal depends on the thickness of the mica sample. We interpreted this fact as birefringence effect. Second, the variation of the amplitude of the signal is due to the phase matching. Third, to explain these experimental data we have proposed a detail study of the nonlocal second harmonic radiation generated from the mica. Our model is able to explain the complex angular behavior of the experimental data.

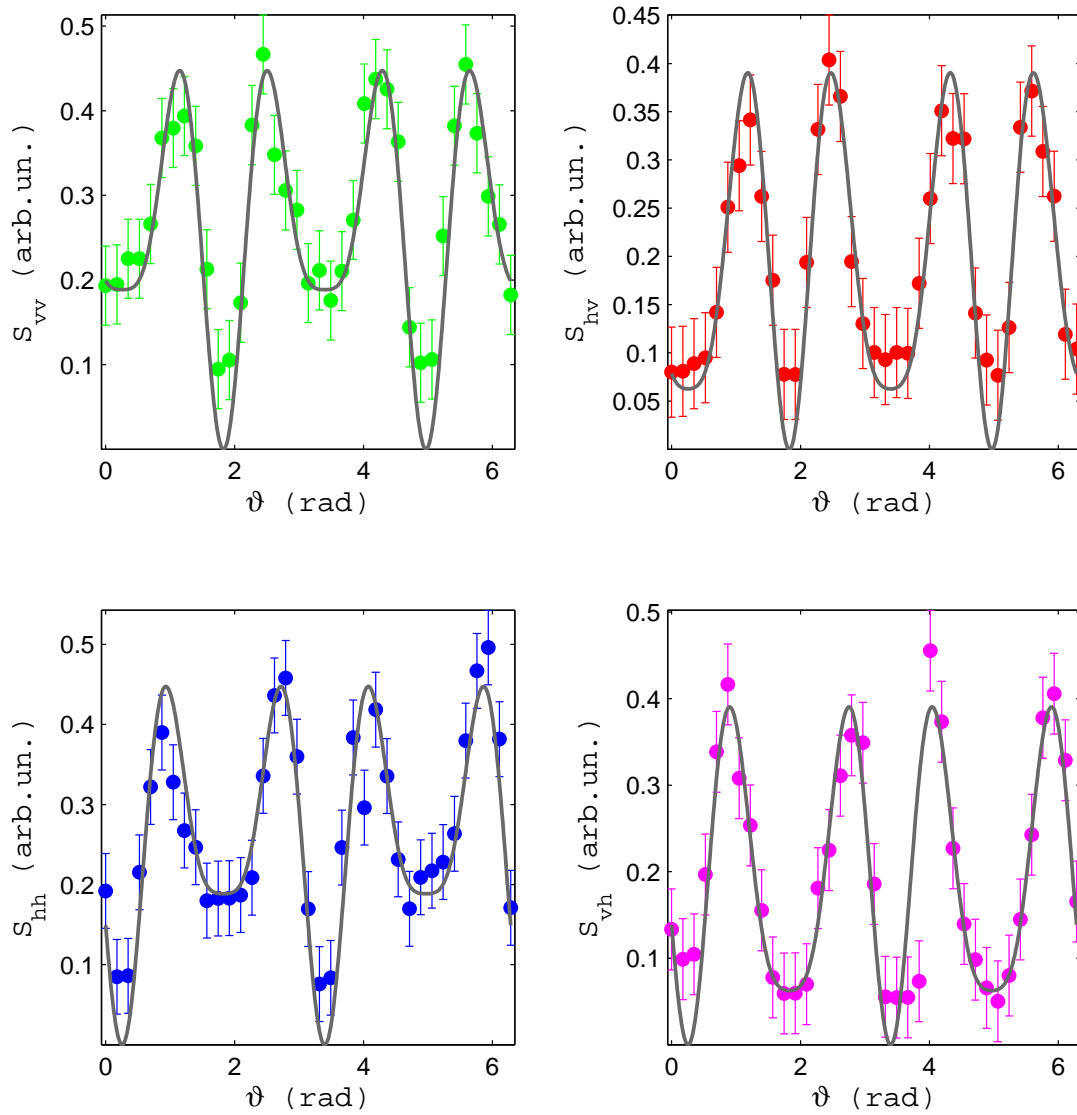


Figure 4.4: Dependence of the second harmonic signals on the mica (sample *III*) rotation angle for 4 different polarization combinations. Circles are data and solid curves are fit from (4.8)-(4.9) equations.

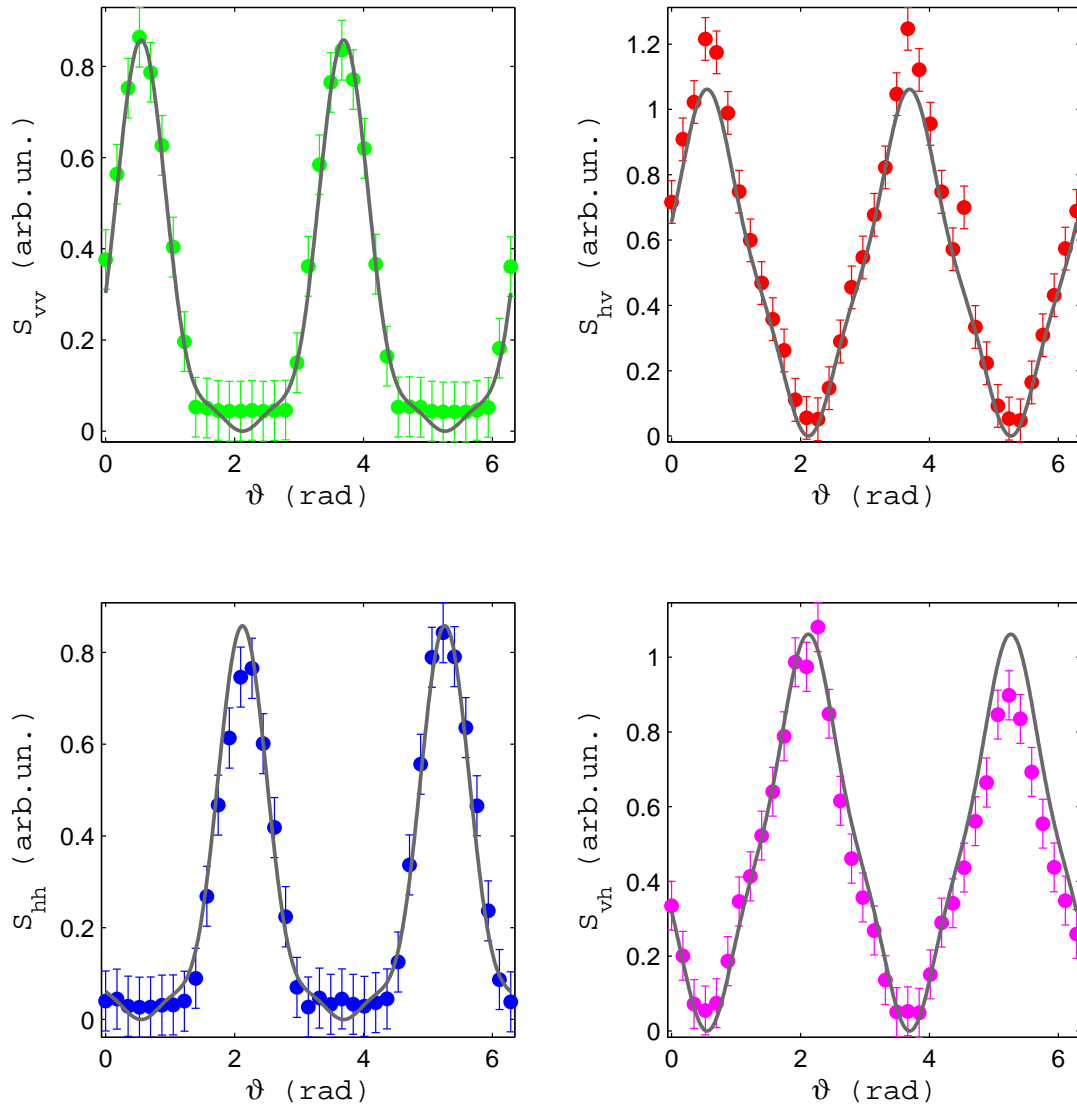


Figure 4.5: Dependence of the second harmonic signals on the mica (sample IV) rotation angle for 4 different polarization combinations. Circles are data and solid curves are fit from (4.8)-(4.9) equations.

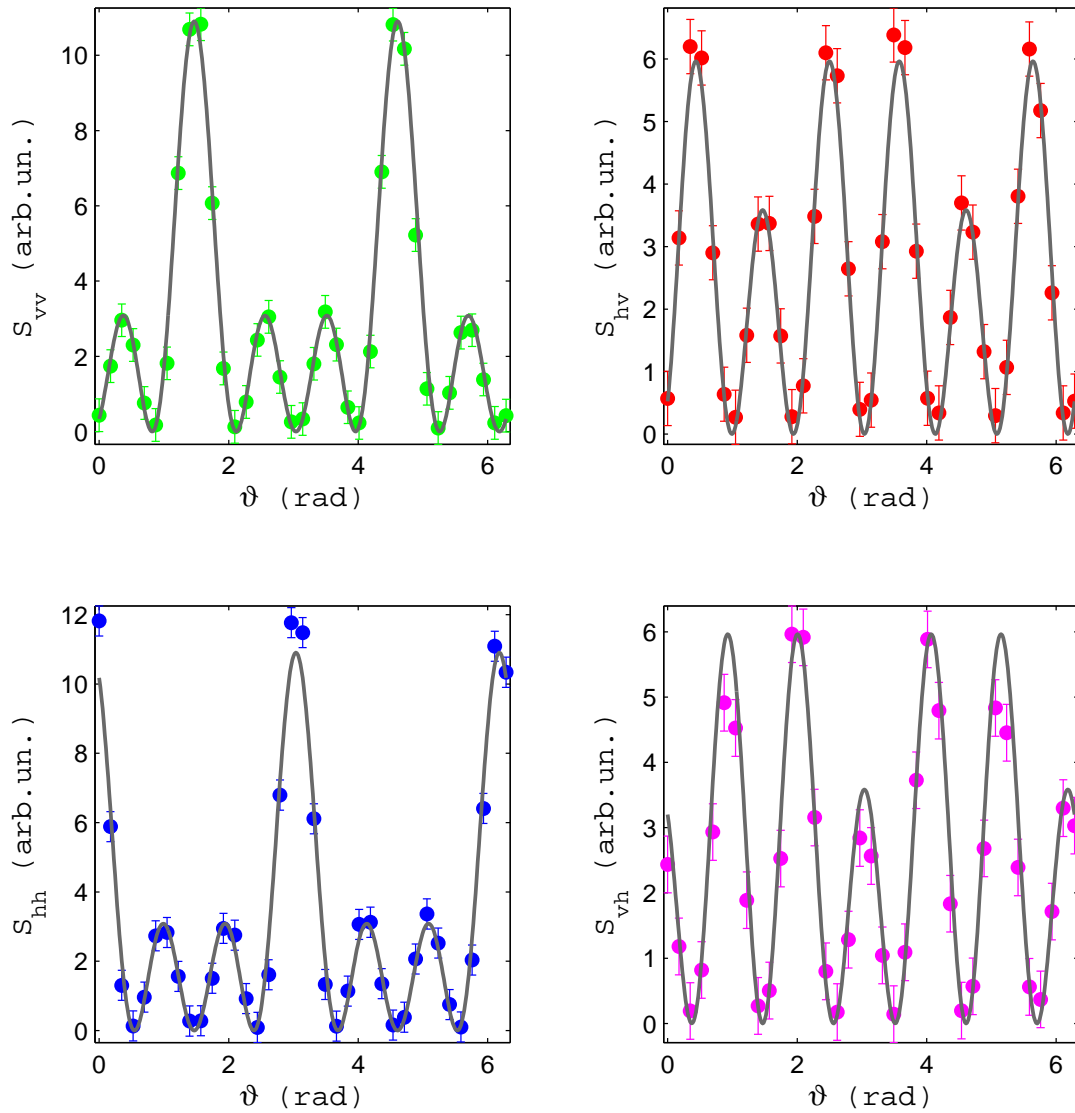


Figure 4.6: Dependence of the second harmonic signals on the mica (*V* sample) rotation angle for 4 different polarization combinations. Circles are data and solid curves are fit from (4.8)-(4.9) equations.

Part II

Application to the study of the
 $\text{LaAlO}_3/\text{SrTiO}_3$ interface

Chapter 5

LaAlO₃/SrTiO₃ interface

Perovskite-structured oxides are complex materials which exhibit a huge number of properties comprising ferromagnetism, ferroelectricity, conductivity and superconductivity [25, 26, 33, 29, 30, 31]. Their interfacial properties are even more interesting. In fact, recently Ohtomo and Hwang [23] reported the existence of a conducting electron layer at the interface between two perovskite-oxide insulators, SrTiO₃ (STO) and LaAlO₃ (LAO).

The second part of my thesis work consisted in the study of this interface by means of SHG. This was the first application of SHG technique to this problem, to the best of our knowledge. In this chapter we first recall, briefly, the known properties of the LAO/STO interface. After that, we present the principal models proposed in literature to explain this unexpected behavior. Finally, in the next chapter, we will show and discuss the results of our SHG measurements.

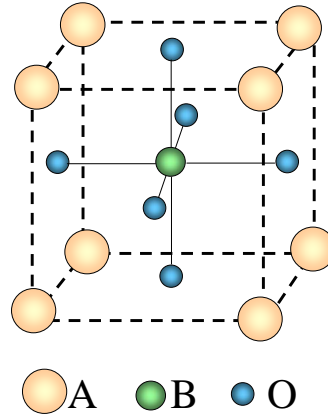


Figure 5.1: Schematic sketch of unit cell for cubic perovskite structure of the bulk crystal.

5.1 Properties of the $\text{LaAlO}_3/\text{SrTiO}_3$ interface

LaAlO_3 and SrTiO_3 are perovskites oxides. This is a family of crystals composed by three different elements A, B and O with chemical formula ABO_3 . As shown in Fig. 5.1, the crystal structure of ABO_3 perovskite is cubic and contains two cation sites: for a choice of the unit cell, the larger cations (A) reside on the cube corners, the smaller cations (B) are in the cube center and the oxygen ions are on the centers of the cube faces. The lattice constant is equal to 3.789 \AA for the LAO and 3.905 \AA for the STO. Both of them are wide-bandgap insulators: 5.6 eV for the LaAlO_3 and 3.2 eV for the SrTiO_3 . In the (001) direction, the LAO structure is made of alternating planes of LaO and AlO_2 , while the STO presents alternating layers of SrO and TiO_2 . Assuming the following formal valence states: La^{3+} , Al^{3+} ,

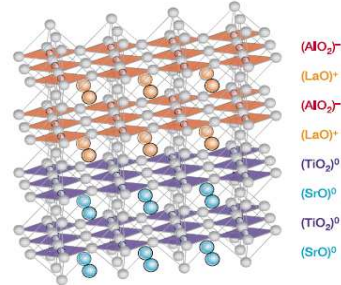


Figure 5.2: Schematic of the $(\text{LaO})^+ / (\text{TiO}_2)^0$ interface, showing the composition and the ionic charge state of each layer of the LAO and STO structure. Reprinted from [33].

O^{2-} , Sr^{2+} and Ti^{4+} , the planes LaO and AlO_2 of the LAO can be considered as $\pm e$ -charged sheets¹, respectively; whereas the plane SrO and TiO_2 of the STO can be considered as neutral sheets (see Fig. 5.2). As a consequence, when a LAO film is grown on a STO substrate a “polar discontinuity” is introduced at the interface. Such discontinuity can lead to nontrivial phenomena. For example, it has been shown by Ohtomo and Hwang [23] that the LAO/STO interface in suitable conditions can become highly conducting. Moreover, very recently, it was also discovered that the LAO/STO interface exhibits a metal-insulator transition applying an external voltage for samples of LAO thickness of 3 unit cells [33]. To this purpose, the possibility to fabricate field-effect transistors devices is started to be explored by using the LAO/STO interface as source-drain channel [33]. These

¹ e is the electron charge.

and other phenomena have spurred a flourishing of research activity, motivated both by fundamental questions and by the emerging prospect of new interfacial oxide electronics. In the next section, we will give a brief overview of the state of the art on this topic.

5.2 State of the art

Since its discovery by Ohtomo and Hwang [23], the unusual metallic state between the LAO and the STO has been the subject of many studies. To date, certain important features of this puzzling phenomenon have been well established. First, the LAO/STO interface, in the (001) orientation, is found to be actually conducting only if the atomic-plane interface is actually $(\text{LaO})^+ / (\text{TiO}_2)^0$, while it is always insulating when the interface is $(\text{AlO}_2)^- / (\text{SrO})^0$ [23]. Second, if the LAO film is grown in reducing conditions, oxygen vacancies are generated in the STO substrate and give rise to a rather strong electron doping in a STO layer adjacent the interface and extending several microns inside the STO substrate [30, 32]. If the growth is instead performed in a high enough O_2 pressure or a suitable oxidation annealing step is performed after growth, so as to eliminate essentially all oxygen vacancies, one still finds a residual interfacial carrier density of $10^{13} - 10^{14} \text{ cm}^{-2}$, giving rise to conduction [33, 30, 32]. However, and

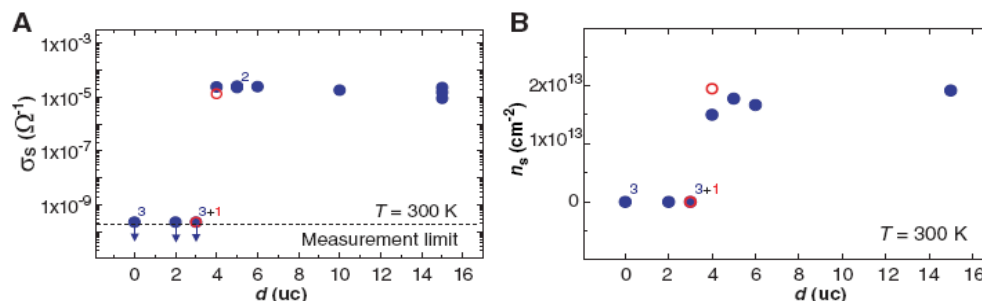


Figure 5.3: Influence of LaAlO₃ thickness on the electronic properties of the LaAlO₃/SrTiO₃. (A) Conductance measurement and (B) carrier density of the interfaces plotted as a function of the number of their LaAlO₃ unit cells. Reprinted from [33].

this is the third important feature, in these growth conditions the interface is found to be conducting only when the thickness of the LAO layer is equal or above a threshold of 4 unit cells (u.c.), otherwise it is insulating [33, 30] (see Fig. 5.3). Moreover, these “residual” carriers are localized in a very thin interfacial layer, only few nanometers thick. The currently leading interpretation of these phenomena is based on the so-called “polar catastrophe” idea [25] (see Fig. 5.4). Briefly, the charged character of the LAO atomic layers grown with a well defined order would give rise to an ever increasing electrostatic potential and energy for increasing thickness. As this cannot be sustained, an interfacial reconstruction must necessarily occur for a large enough thickness of the LAO film. Since for these LAO/STO structures no ionic lattice reconstruction takes place (although some small interface roughening is actually observed [25]), it has been proposed

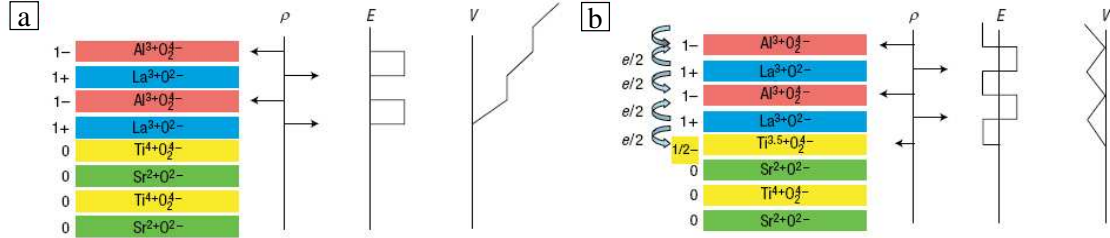


Figure 5.4: The polar catastrophe illustrated for the (001) interfaces between LaAlO_3 and SrTiO_3 ; a, the interface plane $\text{AlO}_2/\text{LaO}/\text{TiO}_2$ produces a non-negative electric field (E), leading to an electric potential (V) that diverges with thickness. b, the divergence catastrophe can be avoided if half an electron is added to the last Ti layer. This produces an interface dipole that causes the electric field to oscillate about 0 and the potential remains finite. Reprinted from [25].

that a purely electronic rearrangement is induced, leading to the injection of electrons from LAO to STO, presumably placing them in the STO conduction band.

Ideally, a charge of half electron per unit cell ($e^-/\text{u.c.}$) should be injected, corresponding to a density of $3 \times 10^{14} \text{ cm}^{-2}$, close enough to the measured value. This simple explanation is very appealing, but reality is probably much more complex.

Very recent theoretical studies point to rather significant lattice distortions taking place at the interface, both before [35] and as a consequence of the electron redistribution [36]. These distortions may in turn contribute to localizing part or all of the charges (particularly at low temperatures), and presumably also might allow for the onset of magnetism, which has been actually observed for certain growth conditions [31].

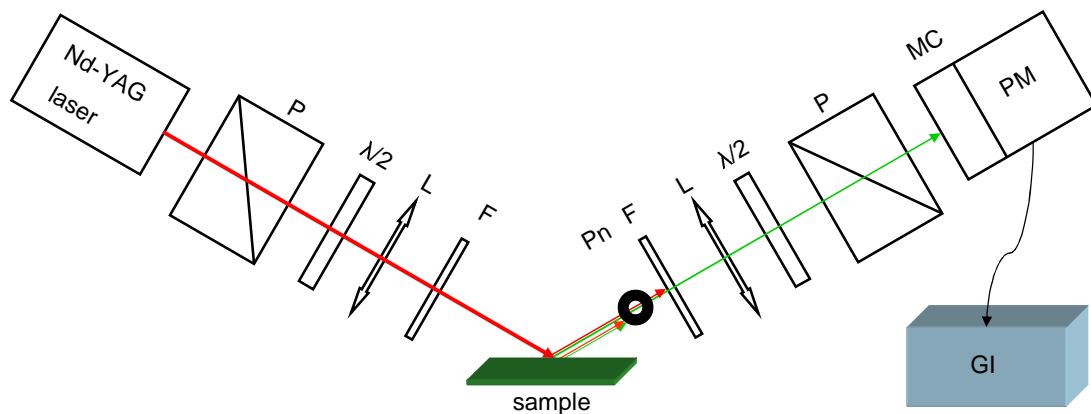
To clarify these issues, it would be desirable to use a direct experimental probe of the electronic polar rearrangements taking place at the interface. To this purpose, we use the Second Harmonic Generation technique. In the next chapter, we will show our SHG results for the LAO/STO interface, the field-effect experiment performed on a sample with $d = 3$ u.c. and the SHG measurements on sample where the termination of the STO substrate is the plane SrO.

Chapter 6

Experimental setup and SHG results for $\text{LaAlO}_3/\text{SrTiO}_3$ interface

In the first part chapter, we report the results of our SHG-based investigation of the LAO-STO system for an increasing thickness d of the LAO film. In the last two sections, we present our very recent SHG measurements on the field-effect transistor and on the SrO-terminated STO.

The surface SHG experiment is illustrated in Fig. 6.1. A detailed description of the SH experimental setup has been done in the chapter 3, so only a brief outline is given here. The SH experiment was performed with the output of the Nd-YAG pulsed laser. The wavelength $\lambda = 1064$ nm of the laser corresponds a photon energy of 1.17 eV, well below the gap energy of both LAO and STO, so as to minimize any possible photoinduced effects. The samples were positioned with the



Legend

P polarizer

$\lambda/2$ wave plate

L lens

F filter

Pn pinhole

MC monochromator

PM photomultiplier

GI gated integrator

Figure 6.1: Second Harmonic experimental setup in the reflection geometry.

LAO/STO interface on the top side, on which the laser beam impinges from air.

A pinhole placed after the sample was used to block the light reflected from the lower surface of the substrate (although this surface gives rise mainly to scattered reflection, as it is optically rough). The reflected SH signal at 532 nm was focused onto the entrance slit of a monochromator. The second harmonic signal was detected with a photomultiplier tube and sent to a gated boxcar amplifier. In fact, despite the high power of the input laser, the signal collected was weak and consisted of only a few photons of second harmonic light detected per input laser pulse. Therefore, the detection scheme required the use of the so called “photon

counting” approach. It is based on a gated integrator (Stanford-Research SR250) which amplifies and integrate the signal measured within a specified time-gate synchronized with the input laser pulse. In this way, a background noise was achieved of about three photons in 2000 laser pulses. Finally, the SH signal was converted from analog to digital by means of an A/D converter and sent to a pc for further elaboration.

6.1 Samples

We studied two different sets of samples, the first one (set 1) from the Naples University and the second one (set 2) from the Institute of Physics of Augsburg University. For both the sets, the LAO/STO interface was obtained by PLD (Pulsed Laser Deposition). Pulsed laser deposition is a technique highly suited to growing multi-component oxides. A pulsed laser beam is focused onto a solid, stoichiometric target, named substrate. The beam ablates an energetic plume of material, generally preserving cation stoichiometry, which is deposited on the substrate. Oxygen partial pressure is usually provided in the growth chamber. In-situ reflection high-energy electron diffraction (RHEED) is used to monitor the film growth and the surface morphology during the deposition process.

The samples of the set 1 were grown in oxygen atmosphere of 10^{-4} mbar at the

800°C, whereas those from the set 2 were grown at about same temperature in an oxygen atmosphere of 8×10^{-5} mbar, then cooled to room temperature in 400 mbar of O₂, with a 1-hour oxidation step at 600°C [28]. Both approaches are believed to avoid the introduction of significant concentrations of oxygen vacancies in the STO substrate. The thickness of the STO substrate for the two sets is not the same: it is 0.5 mm for the set 1, 0.5 mm and 1 mm for the set 2; the transverse dimensions of the samples are 5×5 mm in those of set 1, and 5×10 mm and 5×5 mm in those of set 2. Resistivity measurements performed on samples grown in the same conditions showed that in both sets a nonvanishing conductivity appears only for a LAO thickness $d \geq 4$, in agreement with previous results [33]. Moreover, Hall measurements showed that the interfacial carrier density at room temperature for $d \geq 4$ is of the order of $5 - 10 \times 10^{13} \text{ cm}^{-2}$ in samples of set 1 and of the order of $1 - 3 \times 10^{13} \text{ cm}^{-2}$ in samples of set 2.

6.2 Preliminary results

All our SHG measurements were performed at room temperature, in normal air atmosphere, after cleaning the investigated surfaces with isopropyl alcohol so as to eliminate possible physical adsorbates that could alter the SHG signal. By forcing its complete evaporation with a heating cycle, we also verified that the

isopropyl alcohol itself did not affect the SHG signal significantly. The SHG in reflection from the upper surface of the samples was selected for measurements (the substrate thickness, 0.5 or 1 mm, was large enough to allow for a direct optical separation of the two SHG beams respectively generated from the upper and lower sample surfaces). Since the LAO film thickness is very small compared to the optical wavelength, the SHG is expected to include contributions arising from the LAO upper surface, the LAO film, and the LAO/STO interface, with negligible propagation-induced dephasing between them.

First, we measured the second harmonic signal from the samples with $d = 3$ u.c. and $d = 4$ u.c. of both of the sets for four different input-output polarization combinations. The ps and ss signals are very small (almost comparable to dark signal), so they are not reported. This fact is expected because the symmetry of the interface under investigation is C_{4v} . The pp and sp SHG signals were measured in different positions of each sample. We obtained that the samples of set 1 are homogenous (variation in the SHG intensity below 10% for both the polarization combinations). The results for the set 2, presented in Fig. 6.2, show a behavior dependent on the position within the sample. The SHG signal was measured in three different positions, one approximately in the center, the other

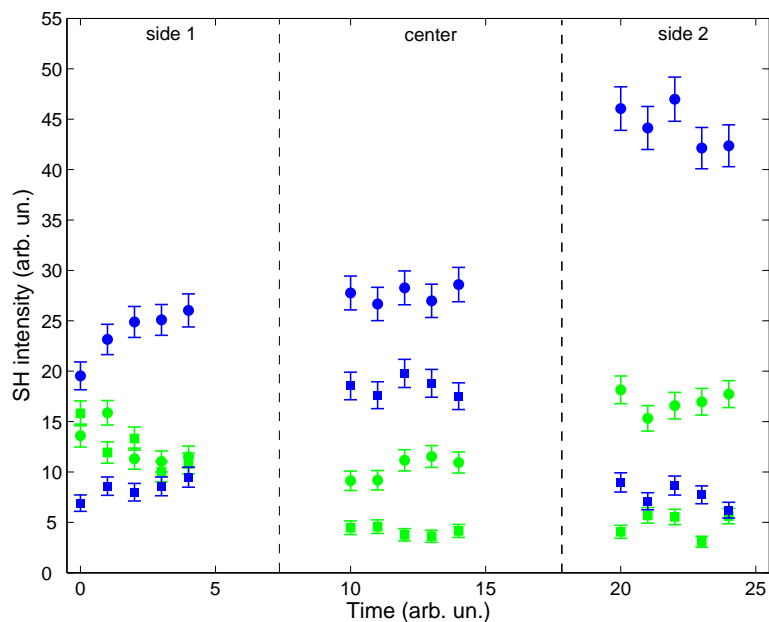


Figure 6.2: Dependence of the time of the pp (circle) and sp (square) signals of the sample of thickness of 4 u.c. LAO (green) and 3 u.c. (blue) in three different position.

two are approximately mid-way between the center and each side of the long direction of the samples. The thickness of the substrate is 0.5 mm for the sample with 3 u.c. and 1 mm for that with 4 u.c. For the pp signal, variations of about 100%, in the sample of 3 u.c., and of 80%, in the sample of 4 u.c., are observed; for the sp signal, variations of about 100% are observed in both of the samples. The sp signal is smaller than the pp signal for the sample with 3 u.c. in each position, whereas for the sample of $d = 4$ u.c., it is approximately equal to the pp signal in the side 1 and smaller than pp in the others positions. We exclude that the difference in the SH signal (for both the polarization combinations) from the two

samples is due, in part or entirely, to the different thickness of the STO substrate because we blocked any possible contribution to the SH signal of the lower STO surface by introducing the pinhole (see Fig.6.1). To conclude this section, since we observed a different SH signal from the two samples, we started a systematic study of the LAO/STO interface for a varying thickness of the LAO film. In the next sections, we will show and discuss the results of this study.

6.3 SHG intensity results

Normal SHG intensity measurements (NSHG, in the following) provide a signal which is proportional to the squared-modulus $|\chi^{\text{eff}}|^2$ (see equation (1.50)). We verified that our laser input beam was not altering the interfacial electronic state and then that the laser exposure did not generate significant photoconductivity in the samples, by studying the NSHG signal $I(2\omega)$ dependence on the input laser intensity I . If the surface properties are unaffected by the light, the χ^{eff} is constant and one has $I(2\omega) \propto I^2(\omega)$, i.e., a pure quadratic behavior. Fig. 6.3 shows a typical result we obtained at the center of the sample of thickness $d = 6$ u.c. of the set 1. The good quadratic fit confirms the absence of photoinduced effects. The quadratic coefficient obtained from this fit is proportional to the squared-modulus of χ^{eff} . We used this approach to measure $|\chi^{\text{eff}}|$ across many of

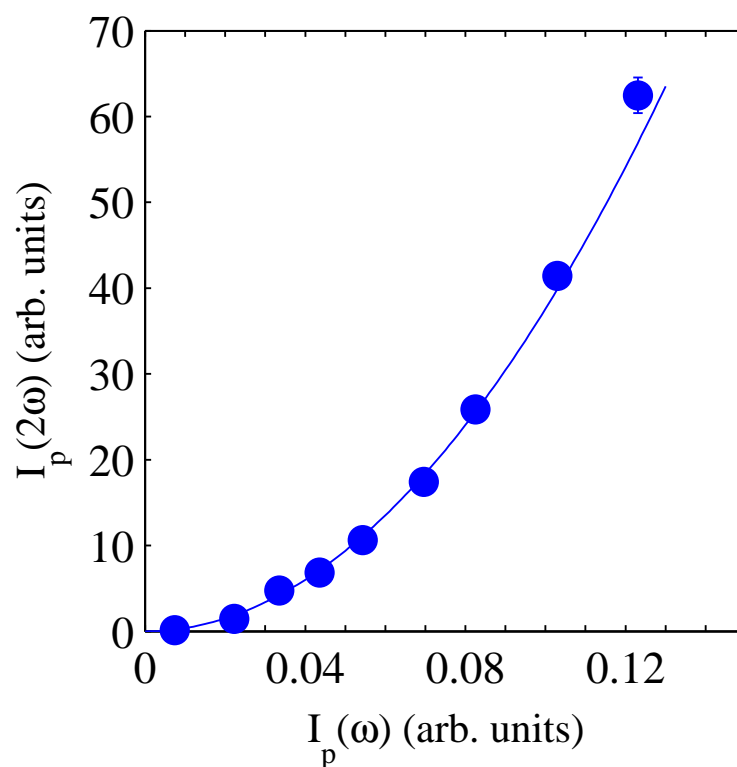


Figure 6.3: Dependence of the SH signal of the input laser intensity for the sample of $d = 6$ u.c. of the set1.

our samples. Since the samples of the set 2 are not homogenous, we repeated the measure in different points, then we calculated the average $|\chi^{\text{eff}}|$ and plotted it as function of the thickness of the samples. In Figs. 6.4 and 6.5 we show our NSHG results. Let us start from the pp polarization combination. In set 1 (see Fig. 6.4a), the NSHG is approximately constant from $d = 0$ (pure STO substrate) to $d = 3$, while it rather increases for $d > 4$ and then remains constant. For the set 2 (see Fig. 6.4b), the behavior of the data is more complex: the NSHG decreases

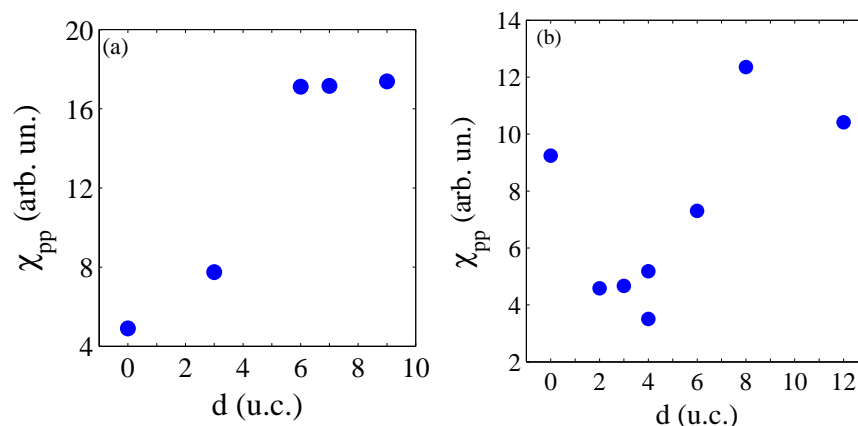


Figure 6.4: Dependence of the thickness of the NSHG for the polarization combination pp . The results of the set 1 are in (a), those of the set 2 in (b).

from $d = 0$ to $d = 4$, then there is an abrupt variation at $d = 6$, a further increasing at $d = 8$ and, finally, a decreasing at $d = 12$. For the sp polarization combination, in set 2 (Fig. 6.5b), the NSHG signal is small and approximately constant for $d = 0$ u.c. and $d = 2$ u.c., while it rather abruptly increases for $d = 3$, and then finally increases even further up to $d \approx 8$, while decreasing again for thicker samples. A similar behavior seems present also for set 1.

Although, these first observations already point to something of abrupt probably taking place in the samples for $d \geq 3$, we cannot draw secure conclusions from these measurements alone, due to the lack of sensitivity of NSHG to the phase of the χ^{eff} . In fact, χ^{eff} is a complex quantity and, for example, a dramatic variation such as a sign-inversion would pass completely unnoticed with NSHG. To measure

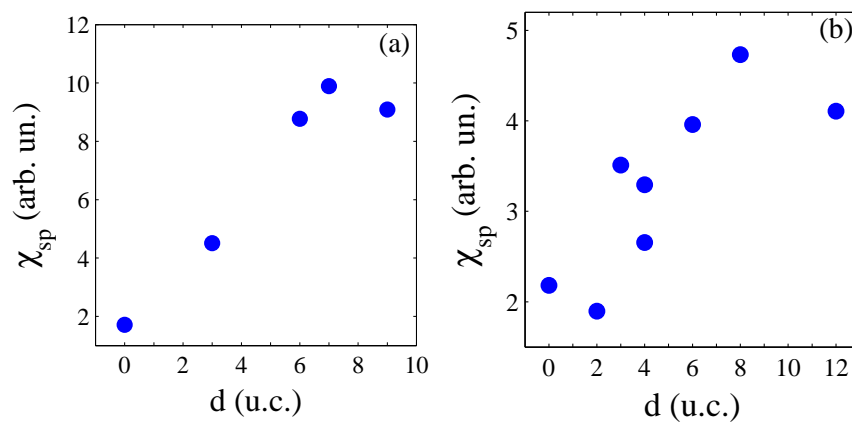


Figure 6.5: Dependence of the thickness of the NSHG for the polarization combination sp . The results of the set 1 are in (a), those from set 2 in (b).

the full χ^{eff} and then its phase, we adopted a homodyne SHG (HSHG) detection geometry. The details of the measurements and the results are shown in next section.

6.4 Homodyne SHG measurements: results and discussion

To perform homodyne SHG measurements, we placed a nonlinear optical medium, named reference, in the incident beam path, as shown in Fig. 6.6. The dispersion of light in air causes the phase shift, and varying the distance L between the two SHG media, the sample and the reference, the phase shift varies. The interference

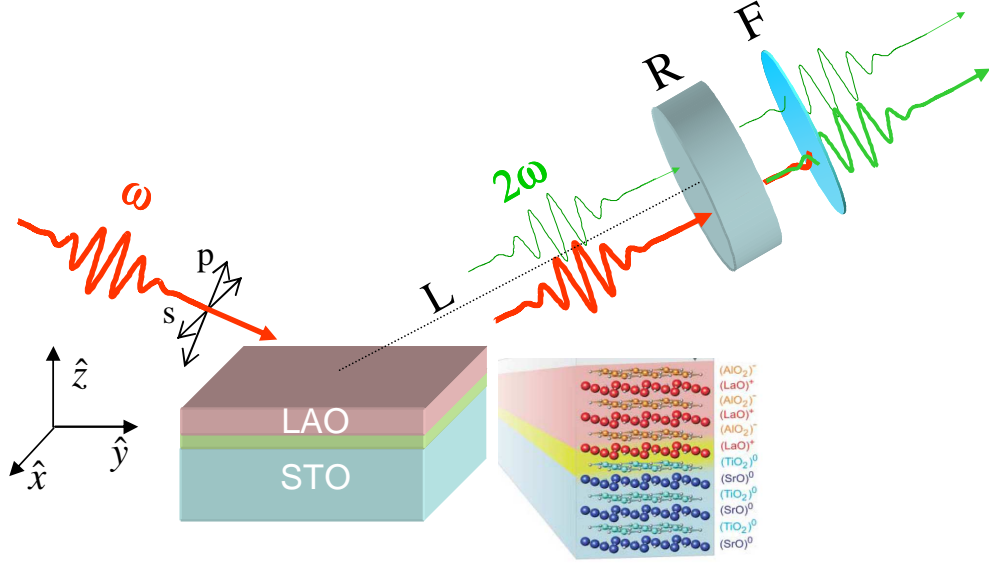


Figure 6.6: Schematic of our homodyne SHG experiment. The SH light (2ω , drawn in green) generated in reflection by the upper surface of the sample is made to interfere with the SH generated by a reference quartz crystal (R). The latter is moved along the beam path (with displacement L), so as to modulate the phase difference of the two SH terms by exploiting the air dispersion. The reflected light at the fundamental frequency ω (drawn in red) is filtered out before detection (F). The input/output polarizations used in our experiments are also shown: s - optical electric field parallel to sample surface xy ; p - optical field in the incidence plane yz .

pattern obtained is described by the relation obtained in the section 1.1.4:

$$I(2\omega) = K \frac{|\chi_s|^2}{1 + z_s^2/z_0^2} + K \frac{|\chi_r|^2}{1 + z_r^2/z_0^2} + 2K \frac{|\chi_s||\chi_r|}{\sqrt{(1 + z_s^2/z_0^2)(1 + z_r^2/z_0^2)}} \times \quad (6.1)$$

$$\times \cos(\mathbf{L}(z_r - z_s) + \arctan(z_r/z_0) - \arctan(z_s/z_0) + \varphi_s - \varphi_r).$$

A typical interference measured for a given sample is shown in Fig. 6.7. With suitable fitting, we obtain from the (6.1), both the modulus and the phase (the latter up to a constant, common to all measurements) of the complex χ^{eff} for each sample.

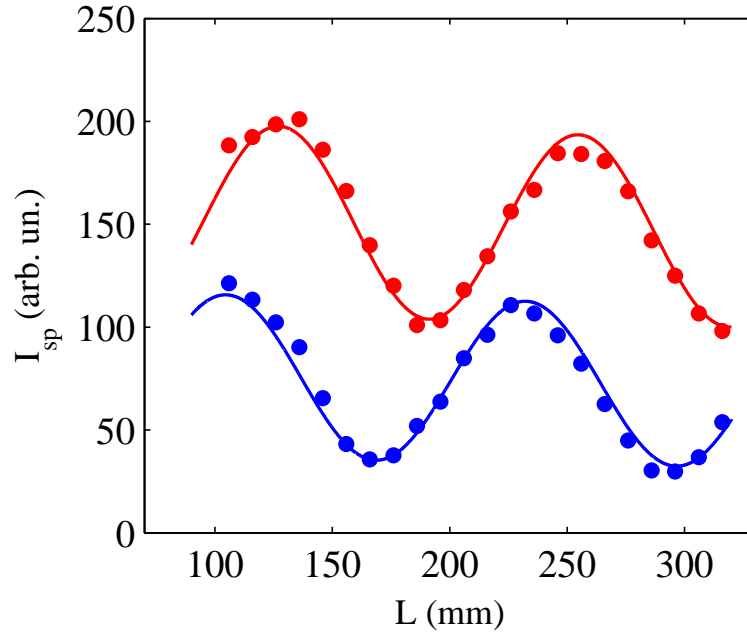


Figure 6.7: Two example of SH interference patterns observed in our HSHG experiment for sample of $d = 3$ u.c. (blue dots) and $d = 4$ u.c. (red dots) from the set 1.

Let us start the analysis of the experimental data from the measured amplitude of χ_{sp} . The results we obtained are shown in Fig. 6.8. We see that the SHG signal amplitude changes only little when passing from $d = 0$ (STO substrate) to $d = 2$ (actually, it is slightly reduced) [43], while an abrupt large increase of SHG intensity (or $|\chi_{sp}|$) occurs for $d = 3$. On further increase of d , the SHG amplitude increases further slightly and then saturates, or possibly starts decreasing again (with some sample-to-sample irregularity). This step-like behavior is clearly evident for our samples set 1, while the step height is smaller for set 2 (a fact

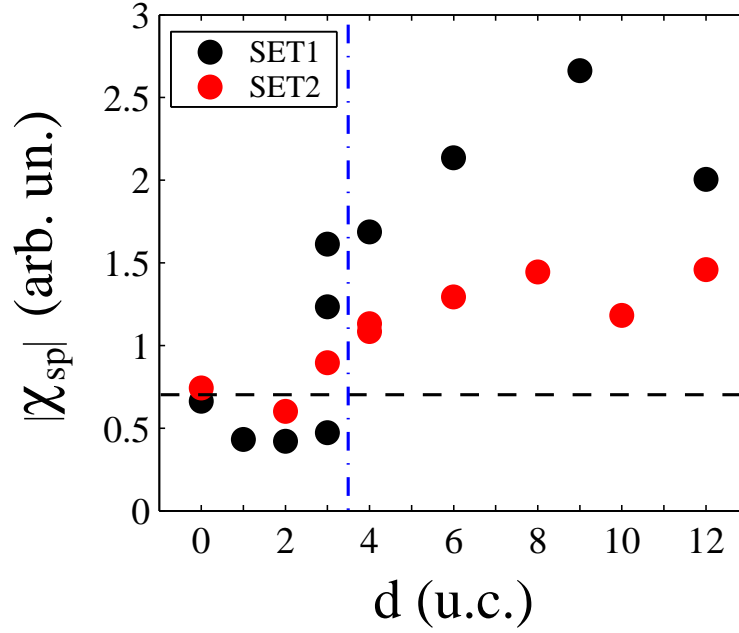


Figure 6.8: Amplitude of the SHG nonlinear susceptibility $|\chi_{sp}|$ as a function of LAO thickness d for our set 1 (black dots) and set 2 (red dots) samples. Different data points having the same d refer to different samples. The dashed line gives the average SHG amplitude of the STO substrates ($d = 0$). The dot-dashed line corresponds to the threshold thickness for the onset of conductivity.

possibly related with the smaller carrier density measured in the latter samples).

This SHG behavior is strongly reminiscent of the abrupt conductance variations seen as a function of d (see Fig.5.3). However, the SHG step takes place always at $d = 3$, while the conduction onset is located at $d = 4$. Therefore, we believe that SHG amplitude is not detecting directly the carrier electrons, but it is instead *revealing another phenomenon that acts as a precursor for the onset of conductivity*. In general, an enhanced SHG amplitude should reflect an increased degree of polarity experienced by the ensemble of all interfacial electrons (e.g., due to

increases in the local ionic crystal field or to electronic transfer from less polar to more polar orbitals) and/or, possibly, a transfer of electrons from less polarizable orbitals to more polarizable ones (e.g., having a smaller local bandgap). We will discuss further below some possible specific interpretations of this transition. Different samples with $d = 3$, even within the same set, show a strongly variable SHG signal, ranging from very close to that of $d = 2$ samples to more similar to that of $d = 4$ ones. This strong variability, not seen for other LAO thicknesses, could be a further confirmation that $d = 3$ is a threshold thickness for a first-order-like electronic transition. However, we verified that all our $d = 3$ samples remained good insulators. Let us now move on and discuss the behavior of the full complex nonlinear susceptibility χ_{sp} versus d , as determined by the measured HSHG interference fringes (see Fig.6.7). It is convenient to represent these measured variations as a sequence of data points in a complex plane, with the real and imaginary components χ'_{sp} and χ''_{sp} corresponding to the point projections on the two cartesian axes, and the amplitude $|\chi_{sp}|$ and phase $\arg(\chi_{sp})$ corresponding to its polar coordinates (radius and polar angle). Within this representation, the physical magnitude of the electronic rearrangement induced after adding each monolayer of LAO can be directly related with the length of the segment connect-

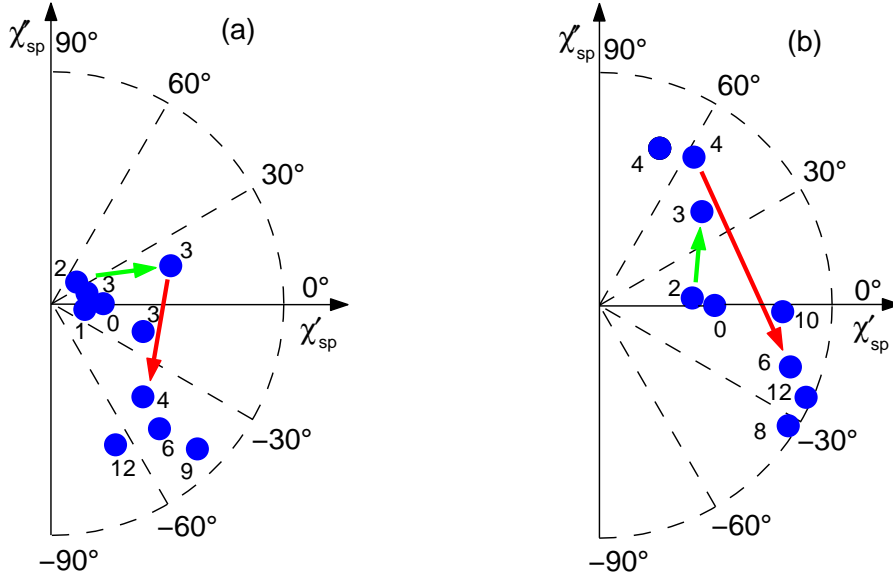


Figure 6.9: Complex effective SHG nonlinear susceptibility $\chi_{sp} = \chi'_{sp} + i\chi''_{sp}$ of the LAO/STO heterostructure as a function of LAO thickness d for our set 1 (a) and set 2 (b) samples. The polar angle of each point corresponds to the argument (or phase) of the complex χ_{sp} , as measured by HSHG (the argument of the STO substrate $d = 0$ being set to zero). The number written close to each data point gives the corresponding thickness of the LAO film, in u.c.. The green and red arrows indicate the two main electronic transitions seen in our data.

ing two consecutive data points on the plane. Our results are reported in Fig. 6.9.

We see once again that the χ_{sp} variations for $d < 3$ are small, while a first large transition takes place at $d = 3$ (green arrows). On further increasing d , however, we now find another abrupt large variation of the HSHG signal (red arrows in Fig. 6.9). This was invisible in the amplitude plots discussed above because the variation is mainly one of phase. This in turn implies that it cannot be caused by a modification of the degree of interfacial polarity. Instead, a χ_{sp} phase variation should reflect an electronic transfer, as optical phase retardations are induced by

the optical resonances available at the electrons. Samples in set 1 (see Fig. 6.9a) exhibit this second transition when passing from $d = 3$ to $d = 4$, i.e., exactly in coincidence with the onset of conduction (the large phase difference between the 3 u.c. and 4 u.c. cases is evident even in the raw data, as shown in the Fig. 6.7). This would suggest a straightforward interpretation of this second transition as directly revealing the injection of electrons in the interfacial conductive states. However, the samples of set 2 (Fig. 6.9b) behave somewhat differently, with only a small change at $d = 4$, and exhibiting the second transition only when passing from $d = 4$ to $d = 6$ (we do not have a $d = 5$ sample). This discrepancy might be again related to the different carrier density seen in the two sets, as in set 1 the mobile electrons represent a substantial fraction of the total number of electrons expected to be injected as a consequence of the polar catastrophe, while in set 2 the conducting electrons are only a small fraction of the total. In both sets, the second transition is associated with the sudden appearance of a large negative imaginary component of the χ_{sp} (the phase zero in these measurements is conventionally taken to correspond to the $d = 0$). All remaining changes seen on further increasing d are minor in both sets.

Now we move on explain the pp data, shown in Fig. 6.10. Set 1 and 2 behave

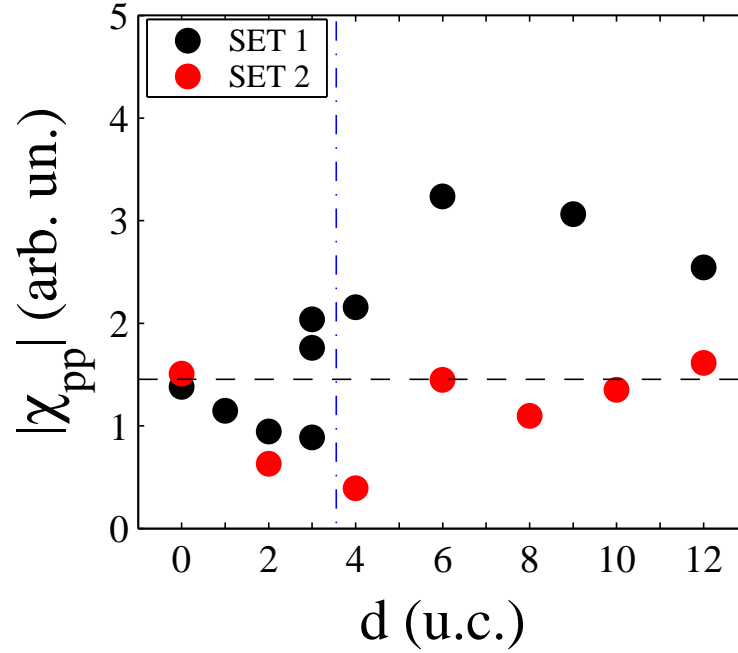


Figure 6.10: Amplitude of the SHG nonlinear susceptibility $|\chi_{pp}|$ as a function of LAO thickness d for our set 1 (black dots) and set 2 (red dots) samples. Different data points having the same d refer to different samples. The dashed line gives the average SHG amplitude of the STO substrates ($d = 0$). The dot-dashed line corresponds to the threshold thickness for the onset of conductivity.

more differently. In the first one, we see a large transition in $d = 3$ (with the same sample-to-sample variability discussed above) and a second one transition in $d = 4$: as in the *sp* case, the signal in $d = 4$ changes approximately only in phase. Then, the complex χ_{pp} increases even further up to $d \approx 6$ and decreases again for thicker samples. Such samples have about the same phase, as you can see from the Fig. 6.11a. For the set 2, we see that χ_{pp} decreases until $d = 4$, then it remains approximately constant. In this case, we have a first abrupt variation

of the HSHG signal (red arrows in Fig. 6.11), that was invisible in the amplitude plot but visible in the polar plot, passing from $d = 2$ to $d = 4$ and a second transition from $d = 4$ to $d = 6$, such as for *sp* polarization combination. However, for the *pp* case, this transition involves both a strong increase of amplitude and a phase variation.

From these data, we can say that, qualitatively, the behavior of the HSHG with the thickness of the LAO film is similar for both the sets because we observed two transition, the first at $d = 3$, before the appearance of the conductivity, and the second one at $d = 4$ or $d = 6$, depending on the different modality of samples preparation. Let us now discuss the possible physical meaning of these results. We propose two alternative hypotheses about the underlying nature of the two main transitions observed with HSHG. The first hypothesis is based on the assumption that the SHG signal is always dominated by the electronic states residing within the STO crystal, as they are expected to be more polarizable than the LAO orbitals due to the smaller bandgap. At 3 u.c., the “polar catastrophe” takes place and some electrons start to be injected from LAO to STO, but end up trapped in localized surface states, or give rise to self-trapped polarons involving local lattice deformations [26, 29, 36]. These electrons would provide the main

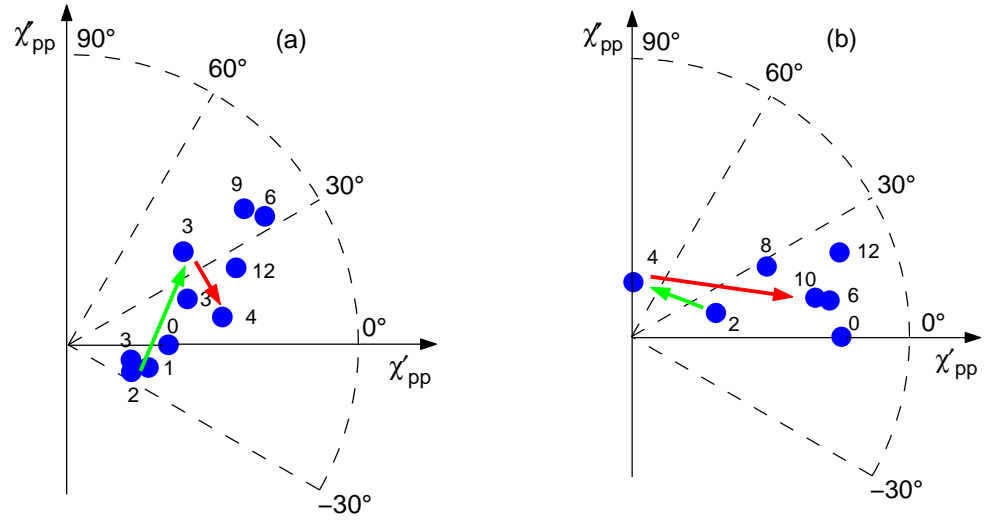


Figure 6.11: Complex effective SHG nonlinear susceptibility $\chi_{pp} = \chi'_{pp} + i\chi''_{pp}$ of the LAO/STO heterostructure as a function of LAO thickness d for our set 1 (a) and set 2 (b) samples. The polar angle of each point corresponds to the argument (or phase) of the complex χ_{pp} , as measured by HSHG (the argument of the STO substrate $d = 0$ being set to zero). The number written close to each data point gives the corresponding thickness of the LAO film, in u.c.. The green and red arrows indicate the two main electronic transitions seen in our data.

contribution to the first SHG transition. On further increasing the LAO film thickness, more electrons are injected but occupy progressively different kinds of interfacial states, including (but possibly not limited to) the extended states that give rise to conduction. These additional electrons give rise to the second SHG transition.

In the second hypothesis, instead, the first transition is ascribed to the electrons still residing in LAO orbitals. The sudden increase of SHG would then be due to a sudden increase of structural polarity of the LAO film taking place when its

thickness reaches the 3 u.c.. The LAO film electronic polarity for $d \leq 2$ could be depressed due, for example, to LAO/STO interfacial roughness and/or cationic mixing [25, 34] or to possible ionic distortions in LAO [29, 35]. These effects could be particularly large in the two monolayers of the LAO film adjacent to STO and to air, thus explaining the 3 u.c. threshold. By this interpretation, the second large transition seen by SHG would be then ascribed to the LAO→STO electronic injection.

6.5 Homodyne SHG measurements and electric-field-effect

An important goal of nanoscience is the creation of new functionality to control materials and their interfaces to atomic dimensions. A way to do it is to modify the carrier density in thin films through the application of an electric field using classical field-effect geometry (Fig. 6.12). In fact, applying an external electric field to a material across a gate insulator electrode G attracts or repels charge carriers, thus creating a thin charge accumulation or depletion layer at the surface which modifies the electrical conductivity between a source (S) and a drain (D) contact. The characteristic width of the accumulation or depletion layer is given by the electrostatic screening length, which, in the semiclassical limit, is the

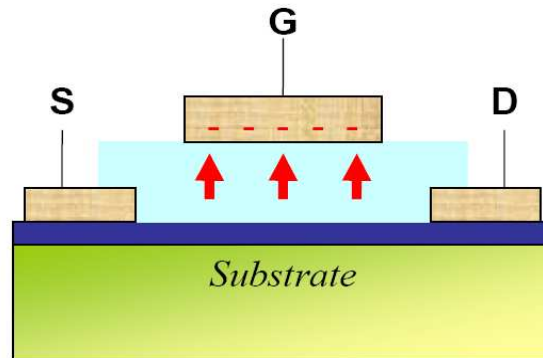


Figure 6.12: Schematic view of geometry used for field effect studies: S, source, G, gate, D, drain.

Thomas-Fermi length λ_{TF} . The high density of charge carriers ($\sim 10^{22} \text{cm}^{-3}$) in a metal implies an extremely short screening length, and then negligible field-effects are found. Instead, in low-carrier-density systems, as semiconductors, the screening length is larger than the metals and, then, field-effects can be obtained. A traditional metal-oxide-semiconductor (MOS) structure is obtained by depositing a layer of silicon dioxide (SiO_2) and a layer of a metal on top of a semiconductor. When a voltage is applied across a MOS structure, it modifies the distribution of charges in the semiconductor. A metal-oxide-semiconductor field-effect transistor (MOSFET) is based on the modulation of charge concentration by the MOS. The MOSFET was made by putting an insulating layer on the surface of the semiconductor and then placing a metallic gate electrode on that. Usually, silicon is

used as semiconductor and a layer of silicon dioxide as insulator. Over the past decades, the MOSFET has continually been scaled down in size. However, the thickness of conventional SiO₂ layer is approaching its physical limit, due to its large tunneling leakage current. LaAlO₃ was found to be a promising candidate for SiO₂ replacement because it has many outstanding features: high dielectric constant [21], wide energy band gap [20], large conduction band offsets with silicon [24] and stable thermal property during the MOSFET annealing process [22]. Recently, the LAO/STO interface was used in a suitable configuration to tune the carrier density at the interface by using the electric-field-effect[33]. To this purpose, we decided to verify if with our homodyne SHG measurements we can study this effect. In this section, we report our field-effect measurements performed at room temperature. We induced the electric-field effect on a sample of LAO/STO of thickness of 3 u.c.. The sample was prepared as indicated in ref [33] and maintained in a dark environment to suppress carrier photoexcitation in the STO. Sketch of the sample and contacts configuration is given in Fig. 6.13. The resistivity measurements were performed with a standard four probe technique [38]. The result of the measurement is shown in Fig.6.14: we started with the sample in the insulator state (the voltage V_g applied to the backside contacts

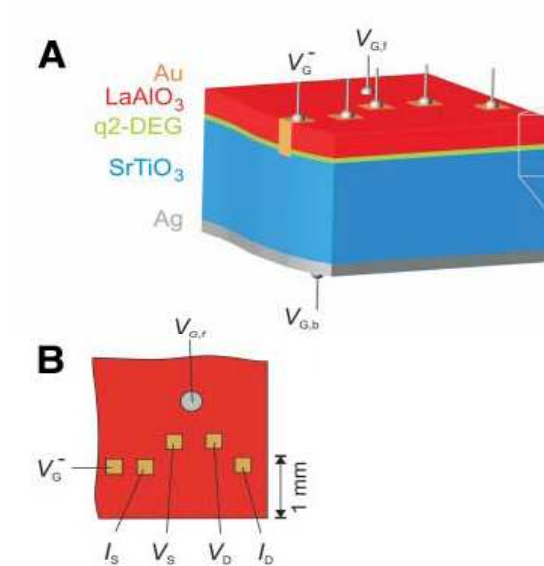


Figure 6.13: Sketch of the samples and the contacts configuration: the left side of the sample sketch in (A) is a cross-sectional cut. The SrTiO_3 substrate is 1 mm thick. Current-voltage and resistance measurements were done with the configuration shown in (B). Reprinted from [33].

of the STO is equal to -100 V). During the insulator phase of the sample, we measured the interference pattern (interference pattern 1 in Fig. 6.14(a)) for the polarization combinations sp (the results for the pp polarization combination, not reported here, are the same). After that, on applying a gate voltage of 100 V, we expected that the sample switched to the metallic state as reported in [33]. However, we did not observe a change in the resistance. To obtain the switching, it was necessary to expose the sample to the ambient light. We verified, by mea-

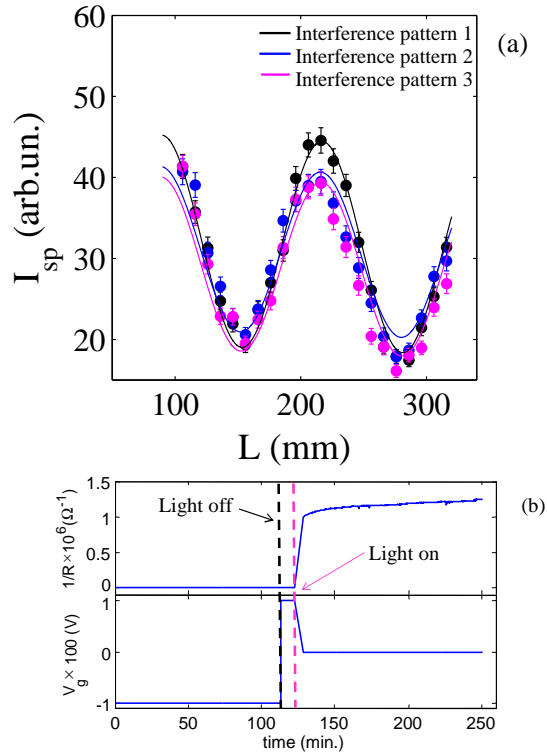


Figure 6.14: (a), HSGH measurements on the sample of thickness of 3 u.c. used for the electric-field-effect when the sample is insulator (Interference pattern 1), and it is conductive (Interference pattern 2 and 3). In (b), we show the resistance measurement.

During the resistance measurement, the sample remained conductive. Immediately after the exposing of the sample to the light, we measured the interference pattern and obtained no significant variation of the phase (pattern interference 2 in Fig. 6.14) with respect to that measured in the insulator state. After about 2 hours, we repeated the HSGH measurement obtaining the same result (see interference pattern 3 in Fig. 6.14). Experimentally, we observed that for our sample the transition from insulator to metallic state is possible only with the light and that the

phase of the effective susceptibility does not change. The latter seems to indicate that the phase does not depend on carriers injected at the interface by external voltage. However, at the present, we are not able to explain why the transition appears under the ambient light and not by changing the external voltage.

6.6 Homodyne SHG measurements and orientational order

In general, HSGH is sensitive to the change of orientation of the dipoles present at an interface. In our case, we did not see a dramatic change of the direction of the dipoles at the LAO/STO interface, for example a change of 180° , with the thickness. However, we performed another experiment with the following set of samples: the STO, the LAO/STO ¹ and other two oxide interfaces, the STO/NdGaO₃ ² and the LAO/STO/NdGaO₃ ³. The new samples were prepared with the same deposition parameters of set 1. NdGaO₃ (NGO) is a perovskite with orthorhombic structure of lattice constants of $a = 0.5433$ nm, $b = 0.55036$ nm and $c = 0.77157$ nm [39]. Now we explain the choice of this particular perovskite as substrate. Ideally, the STO presents two possible termination, the

¹the thickness of LAO is of 12 u.c..

²the thickness of STO film is of 4 u.c..

³the thickness of LAO film is of 10 u.c., that of the STO of 7 u.c., and the NdGaO₃ is the substrate.

TiO₂ and the SrO. To obtain the first termination, the STO is chemically treated and then annealed in oxygen. Instead the second termination is obtained starting from a TiO₂-terminated STO where a single layer of SrO is deposited by PLD. AFM scans show that in the second case the quality of the sample is not high. Moreover it was shown that the surface is not stable [40, 41]. However, a recent work [42] shows that a high quality SrO termination can be achieved by growing a STO film on (110) NGO substrate. Therefore, according to this work, we expected that growing a STO film on NGO substrate all dipoles in the STO are inverted with respect to the case of the TiO₂ termination. In other words, we expect that the interference pattern from the LAO/STO/NGO interface is shifted by 180° with respect to the interference pattern of the STO sample⁴. We performed the measurements for both the polarization combinations *pp* and *sp* and verified that our hypothesis holds true, as it can be seen in the Fig. 6.15(a). These results indicate that the HSHG measurement is sensitive to STO termination. In order to confirm further our hypothesis, we measured also the HSHG from the sample LAO/STO and LAO/STO/NGO obtaining that the signals are 180° shifted in phase. Besides, as shown in the Fig. 6.15(b), the signal amplitude of LAO/STO

⁴In this case the STO termination is TiO₂.

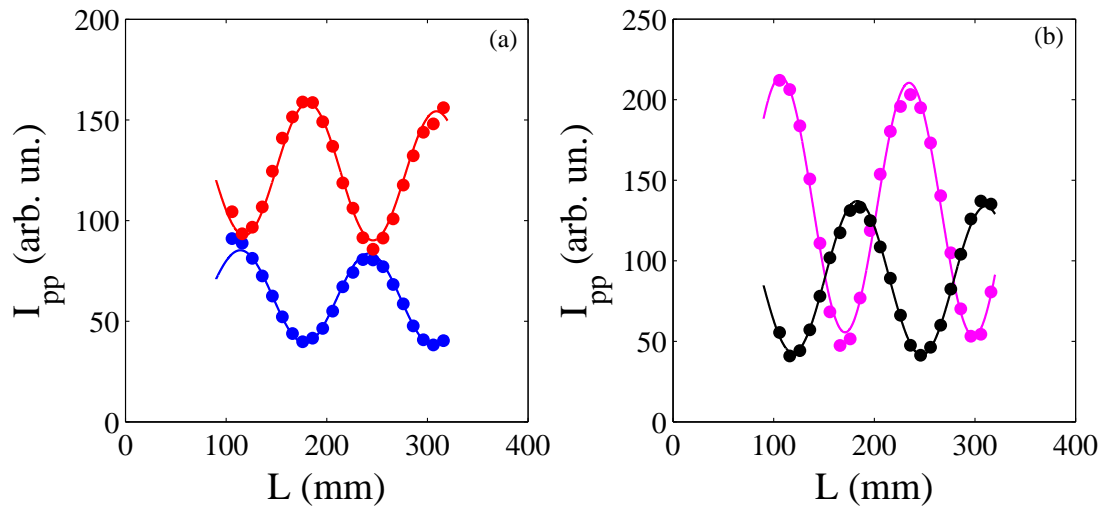


Figure 6.15: (a) Interference pattern of the SrO-terminated STO (red dots) and interference pattern of TiO₂-terminated STO (blue dots). (b) Interference pattern of a film of LAO on TiO₂-terminated STO (magenta dots), interference pattern of a film of LAO on SrO-terminated STO (black dots).

sample is higher than that of LAO/STO/NGO sample. This difference is due to the charge transfer that occurs only when the STO is terminated with a TiO₂ plane.

Conclusions

During my thesis work, I applied the optical second harmonic generation technique to two different topics: the study of the lubrication at molecular level and the study of the electronic properties of the $\text{LaAlO}_3/\text{SrTiO}_3$ interface.

The first project is still underway, but some important intermediate steps have been completed. They were the subject of the first part of the thesis. Here, I have presented the Friction Apparatus and described the procedure followed to interface it. Next, I assembled the experimental setup for the generation and the detection of the second harmonic radiation generated from the mica. The measurements were performed in the transmission configuration, at normal incidence angle, and the second harmonic signal was detected as a function of the azimuthal angle of the mica. I have varied the polarization of both incident and second harmonic radiations to perform the measurements for four different input-output polarization combinations. Despite its centrosymmetry property, mica was found to generate an intense second harmonic radiation, strongly dependent on the sam-

ple thickness and orientation. When this happens, the second harmonic signal must be ascribed to the nonlocal response of the material. Then, we developed a detailed theoretical model, to explain the experimental data, where we included the nonlocal response of the mica into the nonlinear second order polarization. This was the first systematic and complete experimental and theoretical study of nonlocal SHG from the mica.

In the second part of my thesis, I have focused my attention on the $\text{LaAlO}_3/\text{SrTiO}_3$ interface. First, I have developed the experimental setup for the surface second harmonic measurements and verified that the SHG is able to distinguish between samples of different thickness. After that, I upgraded the setup by inserting a reference in order to perform homodyne phase-sensitive second harmonic measurements. This upgrade was necessary for investigating the polar rearrangements taking place at the LAO/STO interface. In this part of the thesis, I have reported our SHG-based investigation of two different sets of samples, grown in different conditions, where the SHG signal was studied as a function of the thickness of the LAO film. Our results indicate that, on increasing the LAO film thickness, a first significant variation of the complex effective second order susceptibility χ^{eff} occurs when the thickness of the LAO film is of 3 unit cells, just preceding the

onset of conduction, and a second variation takes place for a LAO film thickness comprised between 4 (for the set 1) and 6 u.c. (for the set 2), depending on the sample preparation procedure. With respect to the first transition, we believe that the SHG is not sensitive directly to the carrier electrons, but it instead reveals another phenomenon that anticipates the conductivity. Finally, I have performed another experiment to probe the sensitivity of the homodyne configuration to the orientational order of dipoles present at the interface. To this purpose, the measurements done on the samples LAO/STO and LAO/STO/NGO have showed a phase difference of 180° , indicating, thus, the applicability of this technique to detecting the orientation of the film termination. To conclude this second part, I have applied for the first time the second harmonic generation, in a homodyne phase-sensitive configuration to investigate the electronic properties of the LAO/STO interface. There are many conclusions that may be drawn from these results. First, I have observed the capability of the SHG technique to distinguish between different deposition conditions. Second, I have observed two different electronic transitions, the first one at 3 u.c., not yet revealed from conductivity and Hall measurements, which probably gives rise to the polar catastrophe, and the second one depending on the parameter depositions. Third, I have distin-

guished between the SrO and TiO₂ terminations of the STO. This fact is very important because both the terminations of the STO belong to the same symmetry class and then there is no possibility to distinguish between them by means of normal SHG intensity measurements, whereas the homodyne SHG detection geometry, being sensitive to the orientation of the dipoles, is able to do it. To conclude, then, we can say that the homodyne SHG measurements can offer fundamental insights into the investigation of the oxide interfaces and not only on the LaAlO₃/SrTiO₂ interface.

Bibliography

- [1] E. Rabinowicz, *Wear* **159**, 89 (1992).
- [2] B. Jérôme e Y.R. Shen, *Phys. Rev. E* **48**, 4556 (1993).
- [3] Y.R.Shen, *Surface Science* **299/300**, 551 (1994).
- [4] J. N. Israelachvili, P. Mc Guiggan, A. M. Homola *Science* **24**, 189 (1988)
- [5] B. Bhushan, J. N. Israelachvili, and U. Landman, *Nature* **374**, 607 (1995).
- [6] P.Frantz, F. Wolf, X.-d. Xiao, Y. Chen, S. Bosch, and M. Salmeron, *Rev. Sci. Instrum.* **68**, 2499 (1997).
- [7] F. Eisert, M. Gurka, A. Legant, M. Buck, M. Grunze, *Science* **287**, 468 (2000).
- [8] B.Gauthier-Manuel, *Meas. Sci. Technol.* **9** 485 (1998).
- [9] A. I. Bailey e S. M. Kay , *J. Appl. Phys.* **16** 39 (1965).

-
- [10] R. W. Boyd, *Nonlinear Optics* (Academic, San Diego, 1992).
- [11] B. Bushan, J. N Israelachvili and U. Landman, *Nature* **374**, 607 (1995).
- [12] J. Klein, *Annu. Rev. Mater. Sci.* **26**, 581 (1996).
- [13] C. M. Mate, G. M. McClelland, R. Erlandsson, and S. Chiang, *Phys. Rev. Lett.* **59**, 1942 (1987).
- [14] M. Medhat, S.Y. El-Zaiat, *Optics Communications* **141**, 145 (1997).
- [15] E. Hecht, A. Zajac, *Optics* (Addison-Wesley, Massachusetts, 1974) p.248.
- [16] T.F. Heinz, C. K. Chen, D. Ricard, and Shen, *Phys. Rev. Lett.* **46** 1010 (1981).
- [17] Y.R. Shen, *Annu. Rev. Phys. Chem.* **40**,327 (1989).
- [18] Y.R. Shen, *The Principle of Nonlinear Optics* (Wiley, New York, 1984)
- [19] P.Guyot-Sionnest and Y. R. Shen, *Phys. Rev. B* **38**,7985, (1988).
- [20] G. Lim, S. Kriventsov, T. N. Jackson, J. H. Haeni, D. G. Schlom, A. M. Balbashov, R. Uecker, P. Reiche, J. L. Freeouf, and G. Lucovsky, *J. Appl. Phys.* **91**, 4500 (2002).

-
- [21] E. Park and H. Ishiwara, *Appl. Phys. Lett.* **82**, 1197 (2003).
- [22] W. Xiang, H. Lu, L. Yan, H. Guo, L. Liu, Y. Zhou, G. Yang, J. Jiang, H. Cheng, and Z. Chen, *J. Appl. Phys.* **93**, 533 (2003).
- [23] A. Ohtomo and H. Y. Hwang, *Nature* **427**, 423 (2004).
- [24] L. F. Edge, D. G. Schlom, S. A. Chambers, E. Cicerrella, J. L. Freeouf, B. Hollander, and J. Schubert, *Appl. Phys. Lett.* **84**, 726 (2004).
- [25] N. Nakagawa, H. Y. Hwang, and D. A. Muller, *Nature Materials* **5**, 204 (2006).
- [26] R. Pentcheva and W. E. Pickett, *Phys. Rev. B* **74**, 035112 (2006).
- [27] H. Y. Hwang, *Science* **313**, 1895 (2006).
- [28] N. Reyren, S. Thiel, A. D. Caviglia, L. F. kourkoutis, G. Hammerl, C. Richter, C. W. Schneider, T. Kopp, A. S. Rüetschi, D. Jaccard, et al., *Science* **317**,1196, (2007)
- [29] V. Vonk, M. Huijben, K. J. I. Driessen, A. brinkman, S. Harkema, and H. Graafsma, *Phys. Rev. B*, **75**,235411, (2007)

-
- [30] W. Siemons, G. Koster, H. Yamamoto, W. A. Harrison, G. Lucovsky, T. H. Geballe, D. H. A. Blank, and M.R. Beasley, *Phys. Rev. Lett.* **98**,196802, (2007)
- [31] A. Brinkman, M. Huijben, M. V. Zalk, J. Uijben, U. Zeitler, J. C. Maan, W. G. V. der Wiel, G. Rijnders, D. H. A. Blank, and H. Hilgenkamp, *Nature Mat.* **6**, 493, (2007)
- [32] M. Basletić, J.-L. Maurice, C. Carrétéro, G. Herranz, O. Copie, M. Bibes, E. Jacquet, K. Bouzehouane, S. Fusil, and A. Barthélémy, *Nature Mater* **7**, 621, (2008).
- [33] S. Thiel, G. Hammerl, A. Schmehl, C. W. Schneider, and J. Mannhart, *Science* **313**, 1942 (2006).
- [34] P.R. Willmott, S. A. Pauli, R. Herger, C. M. Schlepütz, D. Martoccia, B. D. Patterson, B. Delley, R. Clarke, D. Kumah, C. Cionca, et al., *Phys. Rev. Lett.* **99**, 155502 (2007).
- [35] R. Pentcheva and W. E. Pickett, to be published.
- [36] Z. Zhong and P. Kelly, *Europhys. Lett.* **84**, 27001 (2008)

-
- [37] C. Cen, S. Thiel, G. Hammerl, C. W. Schneider, K. E. Andersen, C. S. Hellberg, J. Mannhart, and J. Levy, *Nature Mat.* **7**, 298 (2008).
- [38] F.M. Smits, Measurement of Sheet Resistivities with the Four Point Probe, *Bell System Technical Journal* **37**, 711 (1958).
- [39] W. Marti et al., *J. Phys.: Condens. Matter* **6**, 127 (1994); L. Vasylechko et al. *J. of Alloys and Compounds* **297**, 46 (2000).
- [40] G. Rijnders et al., *Appl. Phys. Lett.* **84**, 505 (2004)
- [41] U. Scotti di Uccio et al., *Eur. Phys. J. B* **41**, 3 (2004)
- [42] U. Scotti di Uccio et al, *Appl. Phys. Lett.*, submitted.
- [43] It must be noted that the LAO film deposited on STO, since it starts with a given termination, is structurally polar. Therefore, in the absence of electronic rearrangements one would expect a SHG contribution arising from electrons in LAO that is linearly increasing with thickness, starting from the first monolayers. The fact that we do not see this contribution may reflect either the fact that the LAO film electronic polarity is depressed by some unknown mechanism for $n \leq 2$, or that the LAO electrons are much less polarizable, owing to the LAO large bandgap. We verified experimentally that

the LAO(001) surface of a LAO single crystal generates very little SHG, compared to both a pure STO crystal and to all our LAO/STO samples.